Chemical Vapor Synthesis and Characterization of Ga-Zn-Oxynitrides for Photocatalytic Overall Water Splitting

Von der Fakultät für Ingenieurwissenschaften, Abteilung Maschinenbau und Verfahrenstechnik der

Universität Duisburg-Essen

zur Erlangung des akademischen Grades

eines

Doktors der Ingenieurwissenschaften

Dr.-Ing.

genehmigte Dissertation

von

Saša Lukić

aus

Užice, Serbien

Gutachter: Univ.-Prof. Dr. rer. nat. Markus Winterer

Univ.-Prof. Dr. Martin Muhler

Tag der mündlichen Prüfung: 15.06.2021

Ehrenwörtliche Erklärung zu meiner Dissertation mit dem Titel: „Chemical Vapor Synthesis and Characterization of Ga-Zn-Oxynitrides for Photocatalytic Overall Water Splitting"

Sehr geehrte Damen und Herren,

hiermit erkläre ich, dass ich die beigefügte Dissertation selbständig verfasst und keine anderen als die angegebenen Hilfsmittel genutzt habe. Alle wörtlich oder inhaltlich übernommenen Stellen habe ich als solche gekennzeichnet.

Ich versichere außerdem, dass ich beigefügte Dissertation nur in diesem und keinem anderen Promotionsverfahren keine endgültigt gescheiterten Promotionsverfahren vorausgegangen sind.

'Family is a life jacket in the stormy sea of life.'

(J.K.Rowling)

Dedicated to my parents and my wife.

Acknowledgment

It would not have been possible to write this doctoral thesis without the help and support of the kind people around me, to only some of whom it is possible to give particular mention here and express my deepest gratitude:

First and foremost, my mentor Prof. Markus Winterer for all of his patience, guidance and thoughtful feedback during my PhD studies, always aimed at moving me forward. Not only that I had the opportunity to work in his group on this very interesting topic, but I will always remember our friendly conversations, barbecues, excursions around Europe and trip to the USA full of adventures and fun. It made me realize how kind and caring person he is. It was a real joy being a part of the NPPT group.

Prof. Martin Muhler for great cooperation during the MERCUR and DFG SPP1613 projects, as well to those organizations for the financial support and interesting meetings. To my colleagues from Bochum: Philipp Weide, Jasper Menze and especially Wilma Busser for all the knowledge shared and scientific conversations during relaxed coffee breaks.

Prof. Christina Scheu, our cooperation partner during the SPP1613 project and to Siyuan (Spark) Zhang for all the TEM measurements, valuable scientific discussions and opportunity to learn from him.

Stevan Ognjanović, my heartiest gratitude to everything he has done for me. Our relation started in 2008 during our volleyball days. My teammate, my bachelor supervisor, colleague and the most of all a great friend. Thanks for 'watching my back' and unreservedly teaching me and helping whenever I needed. Truly, one of the greatest persons I met in my life.

Viktor Mackert and Alexander Levish (also my only roomie), who were always there to listen to me, cheer me up and give wise advices. Thanks for being great friends and for all the fun we had together during on- and off-faculty activities.

Ulf Spengler, for all his patience and assistance to build the 'bubbler box', as well for many friendly conversations. In addition, we owe great gratitude to Ingo

Kietzmann, Michael Eisenhut, Kai Fedder and Uwe Rettig and their whole team in the mechanical / electrical workshop who helped us with our ideas.

Alexander Kompch, for his scientific help and amazing energy and willingness to organize countless events, such as 'No Plan Tours' organized with Stevan in 2013, which became a legacy and tradition in NPPT. Heike Feiten, for patiently helping me with administration and paperworks. To Julia Gebauer, for all her cheerfulness and positivity that she passed on to us. To Alice Sandman, for morning chats and great mood at the start of the day.

Past, present and future NPPT group members: Roman Ligotski, Claudia Gorynski, Jeremias Geiß, Carolin Schilling, Prof. Frank Schmidt, Detlef Kramczynski, Christian Nothoff, Mohammed Ali, Lukas Helmbrecht, Martin Busch, Kai Gilles, Tobias Schuld, Claudia König and many others for all the energy they were bringing into NPPT and nice moments we have spent together.

Prof. Vladimir Srdić, my first mentor, for introducing me to CVS technique and world of nanomaterials and later to Prof. Winterer. To Ivan Stijepović, Prof. Ljubica Nikolić and the whole group for all the knowledge and love shared for advanced ceramics. Prof. Radmila Nedučin, together with Prof. Tatjana Vulić, for conveying her love for hetergoneous catalysis to me during studies with such an amazing charisma, as well for all the scientific and life advices.

To all of my friends, for their encouragement and support, especially: Nikola Kanas, Branko Ćorilić and Branko Protić who I could always count on. Also, to RIO team in Ivoclar Vivadent, where I started working in 2020.

Finally, my deep and sincere gratitude to my parents Biljana and Vojislav for their continuous and unparalleled love, help and support. Thank you for teaching me the true values of life. Last, but not least, to my lovely wife Anna, for all the love, patience and motivation, especially during countless nights writing the thesis.

Saša Lukić
Lindau (Bodensee), June 2021

Abstract

The development of semiconductors with extended lifetime that split water photocatalytically under visible-light irradiation is a path to efficient conversion of solar energy. The aim of this work is the production of zinc-gallium-oxynitride nanoparticles $(Ga_{1-x}Zn_x)(N_{1-x}O_x)$ with a high potential for improved photocatalytic activity.

Chemical Vapor Synthesis (CVS) is used in this thesis to generate nanoparticles of high purity with well-defined composition, structure, size distribution and high surface area. β-Ga_2O_3 is used for optimization of the CVS process to obtain quantitative structure-property correlations. As demonstrated, a temperature of 1200°C and pressure of 300 mbar are found to be optimal. Pure phase and highly crystalline β-Ga_2O_3 with crystallite size of about 20 nm and specific surface area of 62 m^2/g is generated from inexpensive solid gallium acetylacetonate precursor. With optimal loading of Rh/Cr_2O_3 co-catalysts this sample is regarded as photocatalytically the most active for overall water splitting under UV light compared to all samples synthesized in this work. In addition, the high reproducibility of the sample is confirmed applying the same CVS parameters. CVS β-Ga_2O_3 demonstrates a better stability for long time irradiation under UV light compared to commercial Ga_2O_3. X-ray absorption (XANES and EXAFS) data indicate that β-Ga_2O_3 nanoparticles do not undergo significant local structural changes during overall water splitting experiments.

Light absorption and charge carrier generation can be optimized by size effects and doping and charge carrier separation by low defect density (high crystallinity) and band alignment through microstructural variations. β-Ga_2O_3 is doped with Mn, Rh and Fe to investigate the change in electronic structure and corresponding photocatalytic activity. Doping with 0.26 % of Mn shows the highest photocatalytic activity among doped samples at optimal co-catalyst loading, but still lower than for pure β-Ga_2O_3. Higher dopant concentrations above 1 % generate higher defect densities in the material, which has a negative effect on photocatalytic activity.

By combining Zn and Ga precursors and varying their delivery sequences a mixture of ZnO and β-Ga_2O_3 (using two reactors), as well as the complex spinel phase $ZnGa_2O_4$ (using one reactor) are generated. During the nitridation process nitrogen is incorporated into the crystal structure, while oxygen and zinc are eliminated to form $(Ga_{1-x}Zn_x)(N_{1-x}O_x)$. It is possible to tune atomic composition and band edge positions by varying nitridation times from 0.17 h to 10 h at a temperature of 850°C. The Zn volatilization rate during thermal nitridation starting from spinel $ZnGa_2O_4$ is lower compared to ZnO-Ga_2O_3 mixture. $ZnGa_2O_4$ and ZnO-Ga_2O_3 are nitrided for 5 h at 850°C, which are the optimal nitridation conditions, and Zn/(Zn+Ga) ratios of 0.15 and 0.03, respectively, are observed. Hence, oxynitrides made from $ZnGa_2O_4$ show about four times higher photocatalytic activity than oxynitride from ZnO-Ga_2O_3. However, all nitrided samples show lower activities in UV region compared to pure β-Ga_2O_3, which is also due to increased defect density and higher recombination probability.

Microwave assisted plasma nitridation of $ZnGa_2O_4$ is developed and employed with the aim to decrease the nitridation temperature and increase the Zn/(Zn+Ga) ratio. NH_3 and N_2 are decomposed in a microwave plasma reactor. The wurtzite phase, typical for oxynitrides, is observed already at 550°C. When NH_3 is decomposed by microwave plasma a very aggressive reduction atmosphere (concentration of H_2 increases) is created leading to an even faster loss of Zn. This is avoided by using N_2 as reaction gas and the Zn/(Zn+Ga) ratio changes very little at lower nitridation temperatures. However, the disadvantage of this method is a strong charging of the powder and its loss during the process. Therefore, the powder must be pelleted, which causes co-sintering of the particles during nitridation. After regeneration of powder from pellets the specific surface area is strongly decreased and photocatalytic activity drops.

To generate GaN nanoparticles directly via CVS at lower pressures (e.g. 20 mbar) triethylgallium, as an alternative oxygen-free liquid precursor compared to solid gallium acetylacetonate, is used. This precursor reacts violently in ambient air or in contact with water, and they are very difficult to handle. Therefore, we designed and constructed a novel, complex and unique precursor delivery unit named

‘inert gas box’. GaN nanoparticles with crystallite size below 3 nm and the high specific surface area of 160 m^2/g are generated.

In this work final nanoparticle characteristics and their photocatalytic activities are correlated and supported by comprehensive structural and spectroscopic characterization.

Zusammenfassung

Die Entwicklung von Halbleitern mit verlängerter Lebensdauer, die Wasser unter Bestrahlung mit sichtbarem Licht photokatalytisch spalten, ist ein Weg zur effizienten Umwandlung von Sonnenenergie. Ziel dieser Arbeit ist die Herstellung von Zink-Gallium-Oxynitrid-Nanopartikeln $(Ga_{1-x}Zn_x)(N_{1-x}O_x)$ mit einem hohen Potenzial für eine verbesserte photokatalytische Aktivität.

Chemische Gasphasensynthese (CVS) wird in dieser Arbeit verwendet, um Nanopartikel von hoher Reinheit mit gut definierter Zusammensetzung, Struktur, Größenverteilung und hoher Oberfläche zu erzeugen. β-Ga_2O_3 wird zur Optimierung des CVS-Prozesses verwendet, um quantitative Struktur-Eigenschafts-Korrelationen zu erhalten. Wie gezeigt, erweisen sich eine Temperatur von 1200°C und ein Druck von 300 mbar als optimal. Reinphasiges und hochkristallines β-Ga_2O_3 mit einer Kristallitgröße von etwa 20 nm und einer spezifischen Oberfläche von 62 m^2/g wird aus einem kostengünstigen festen Galliumacetylacetonat-Precursor erzeugt. Bei optimaler Beladung mit Rh/Cr_2O_3 Co-Katalysatoren gilt diese Probe im Vergleich zu allen in dieser Arbeit synthetisierten Proben als die photokatalytisch aktivste für die Gesamt-wasserspaltung unter UV-Licht. Darüber hinaus wird die hohe Reproduzierbarkeit der Probe bei Verwendung der gleichen CVS-Parameter bestätigt. CVS β-Ga_2O_3 zeigt eine bessere Stabilität bei Langzeitbestrahlung unter UV-Licht im Vergleich zu kommerziellen Ga_2O_3. Röntgenabsorptionsdaten (XANES und EXAFS) zeigen, dass die β-Ga_2O_3 Nanopartikel während der Wasserspaltungsexperimente keine signifikanten lokalen Strukturveränderungen erfahren.

Lichtabsorption und Ladungsträgergenerierung können durch Größeneffekte und Dotierung und Ladungsträgertrennung durch geringe Defektdichte (hohe Kristallinität) und Bandausrichtung durch mikrostrukturelle Variationen optimiert werden. β-Ga_2O_3 wird mit Mn, Rh und Fe dotiert, um die Veränderung der elektronischen Struktur und die entsprechende photokatalytische Aktivität zu untersuchen. Die Dotierung mit 0.26 % Mn zeigt die höchste photokatalytische

Aktivität unter den dotierten Proben bei optimaler Co-Katalysatorbeladung, aber immer noch niedriger als bei reinem β-Ga_2O_3. Höhere Dotierstoffkonzentrationen über 1 % verursachen höhere Defektdichten im Material. Dies wirkt sich negativ auf die photokatalytische Aktivität aus.

Durch die Kombination von Zn- und Ga-Precursoren und die Variation Ihrer Zufuhrsequenz wird eine Mischung aus ZnO und β-Ga_2O_3 (unter Verwendung von zwei Reaktoren), sowie die komplexe Spinellphase $ZnGa_2O_4$ (unter Verwendung eines Reaktors) erzeugt. Während des Nitridierungsprozess wird Stickstoff in der Kristallstruktur der synthetisierten CVS Oxide eingebaut und Sauerstoff und Zink eliminiert, um $(Ga_{1-x}Zn_x)(N_{1-x}O_x)$ zu bilden. Durch Variation von Nitridierungszeiten von 0.17 h bis 10 h bei einer Temperatur von 850°C ist es möglich, die atomare Zusammensetzung und die Bandkantenpositionen einzustellen. Die Zn-Verdampfungsrate während der thermischen Nitridierung ist im Vergleich zur ZnO-Ga_2O_3 Mischung ausgehend vom Spinell $ZnGa_2O_4$, deutlich geringer. $ZnGa_2O_4$ und ZnO-Ga_2O_3 werden für 5 h bei 850°C nitridiert. Dies sind die optimalen Nitridierungsbedingungen und es werden Zn/(Zn+Ga) Verhältnisse von 0.15 bzw. 0.03 beobachtet. Dabei zeigt das Oxynitrid aus $ZnGa_2O_4$ eine etwa viermal höhere photokatalytische Aktivität als das Oxynitrid aus ZnO-Ga_2O_3. Allerdings zeigen alle nitridierten Proben geringere Aktivitäten im Vergleich zu reinem β-Ga_2O_3 im UV Bereich was auch auf eine erhöhte Defektdichte und höhere Rekombinationswahrscheinlichkeit zurückgeführt werden kann.

Die mikrowellenunterstützte Plasmanitridierung von $ZnGa_2O_4$ wird mit dem Ziel eingesetzt, die Nitridierungstemperatur zu senken und das Zn/(Zn+Ga) Verhältnis zu erhöhen. NH_3 und N_2 werden durch den Mikrowellenplasmareaktor zersetzt und die für Oxynitride typische Wurtzitphase wird bereits bei 550°C beobachtet. Bei der Zersetzung von NH_3 mittels Mikrowellenplasma entsteht eine sehr aggressive Reduktionsatmosphere (Konzentration von H_2 steigt an), die zu einem noch schnelleren Verlust von Zn führt. Dies wird durch die Verwendung von N_2 als Reaktionsgas vermieden und das Zn/(Zn+Ga) Verhältnis ändert sich bei niedrigeren Nitridierungstemperaturen nur wenig. Der Nachteil dieser Methode ist jedoch eine starke Aufladung des Pulvers und dessen Verlust während des

Prozesses. Daher muss das Pulver pelletiert werden, was zu einer Versinterung der Partikel während der Nitridierung führt. Nach der Regeneration des Pulvers aus den Pellets nimmt die spezifische Oberfläche stark ab und die photokatalytische Aktivität sinkt entsprechend.

Um GaN Nanopartikel direkt über CVS bei niedrigeren Drücken (z.B. 20 mbar) zu erzeugen, wird Triethylgallium, als alternativer sauerstofffreier flüssiger Precursor im Vergleich zu festem Galliumacetylacetonat, verwendet. Dieser Precursor reagiert an der Luft oder in Kontakt mit Wasser heftig und ist sehr schwierig zu handhaben. Deshalb wurde eine neuartige, komplexe und einzigartige Precursor-Zufuhreinheit, die sogenannte Inertgasbox entwickelt. Es werden GaN Nanopartikel mit einer Kristallitätgröße unter 3 nm und einer sehr hohen spezifischen Oberfläche von 160 m^2/g erzeugt.

Die Korrelation zwischen den endgültigen Eigenschaften der Nanopartikel und ihren photokatalytischen Aktivitäten, unterstützt durch eine umfassende strukturelle und spektroskopische Charakterisierung, wird in dieser Arbeit dargestellt.

Contents

Abbreviations, Acronyms and Symbols

∇T	temperature gradient
$\langle p \rangle$	mean pressure value
a, b	Antoine coefficients specific for each substance
A_0	pre-exponential factor in Arhenius law
A_{ag}	surface area of agglomerate
A_j	absorption factor
BET	Brunauer-Emmett-Teller theory
$\bar{c}$	average velocity of the species
CBM	Conduction Band Minimum
c_p	average particle velocity
CVD	Chemical Vapor Deposition
CVS	Chemical Vapor Synthesis
d (XRD)	spacing between the planes in the crystal structure
D	diffusion coefficient of the species
D_0	pre-exponential factor in grain boundary diffusion (coalescence)
d_{BET}	average particle size calculated from BET
d_c	collision diameter of the agglomerate
DEZ	diethylzinc
D_{fr}	fractal dimension of the agglomerate
DFT	Density Functional Theory
D_{gb}	grain boundary diffusion coefficient
d_h	hydrodynamic diameter of the particles
DLS	Dynamic Light Scattering
D_p	particle diffusion coefficient
d_p	primary particle diameter

d_{RT}	diameter of the reaction tube
dV/dt	volume flow
d_{XRD}	average crystallite size measured by XRD
E *(EXAFS)*	incident beam energy
E_0 *(EXAFS)*	absorption edge energy
E_A	activation energy
EDS	Energy Dispersive Spectroscopy
EELS	Electron Energy Loss Spectroscopy
E_g	band gap energy
E_{gb}	activation energy of diffusion
EXAFS	Extended X-ray Absorption Fine Structure
F	backscattering amplitude function
$f(k\alpha)$	Henry function
FEFF	software for the *ab initio* computation of XAS spectra
F_K	structure factor
FTIR	Fourier-transform Infrared Spectroscopy
F_{tp}	thermophoretic force
g	transition parameter from free molecular to continuum regime
$\hbar$	reduced Planck constant
HER	Hydrogen Evolution Reaction
I	electric current
I	Intensity of the incoming X-rays
I^{bkg}	background intensity
I^{calc}	calculated intensity
I_{coh}	intensity of the coherent scattering
I^{exp}	observed intensity
IF	intrinsic (stacking) fault probability
I_{incoh}	intensity of the incoherent scattering
I_o	Intensity of the transmitted X-rays
J_{dep}	deposition (film growth) rate
K	absorption coefficient in Kubelka-Munk equation

k	photoelectron wave vector
k_r	reaction constant in thermal decomposition of precursor
k_B	Boltzmann constant
$k\alpha$	measure of the ratio of the particle radius to Debye length
L_K	factor containing Lorentz, polarization and multiplicity factor
l_{RT}	length of the reaction tube
L_{VP}	conductance of the vacuum pump
$m_{A/B}$	mass of the reactants A and B
MAUD	software for Rietveld refinement of X-ray diffraction patterns
m_e	mass of the electron
MS	microstrain
N (EXAFS)	coordination number
n (XRD)	integer
N/V	number density of the species
N_A	Avogadro constant
N_a	the number density of the agglomerates
N_{ag}	degree of agglomeration
N_{pr}	number density of the precursor molecules
n_r	gas concentration of the reactive component
NMR	nuclear magnetic resonance
OER	Oxygen Evolution Reaction
P (BET)	equilibrium experimental pressure
P_0 *(BET)*	vapor pressure of the adsorption gas
P_k	preferred orientation function
PL	Photoluminescence Spectroscopy
POWS	Photocatalytic Overall Water Splitting
$P_{partial}$	partial pressure of the pre
pPDF	partial Pair Distribution Function
p_{pr}	precursor partial pressure
Q	heat
q_{pV}	suction power of the vacuum pump

r	nuclei radius
R	resistance
R	universal gas constant
r^*	critical cluster radius
R_∞	reflection of the sample layer with infinite thickness
r_i	distance between absorbing and scattering atom
RMC	reverse Monte Carlo
rmcxas	software for the reverse Monte Carlo analysis of EXAFS spectra
S	saturation ratio
S_{km}	scattering coefficient
SEM	Scanning Electron Microscopy
S_F	scale factor
S_0^2	reduction factor by multiple scattering factor
S_{sp}	specific surface area
T	temperature
t	time
t_c	coagulation time
TEG	triethylgallium
TEM	Transmission Electron Microscopy
TF	twin fault probability
TG/DTA	Thermogravimetry and Differential Thermal Analysis
T_{lN2}	temperature of the liquid nitrogen
t_{sinter}	sintering time (coalescence)
UV/VIS	Ultraviolet-Visible Diffuse Reflectance Spectroscopy
V (BET)	volume of the gas adsorbed
V_{ag}	volume of the agglomerate
VBM	Valence Band Maximum
VESTA	crystal structure viewing software
$\dot{V}_{He}$	volume flow of helium
V_j	phase cell volume
V_m *(BET)*	volume of the monolayer covering the surface

V_m	molar volume
V_p	volume of the primary particle
V_{reactor}	volume of the reactor
V_{tp}	deposition rate of the particle in thermophoretic collector
w_i	weighting factor
XAFS	X-ray fine absorption
XANES	X-ray Absorption Near Edge Structure
Z_{AB}	number of collisions between species A and B
Z_{pp}	number of primary particles
α	absorption coefficient correlated to band gap energy
β	collision frequency
γ	surface free enthalpy
ΔG	change in free Gibbs energy
Δp	pressure difference
ε	dielectric constant
ζ	zeta potential
η_g	gas viscosity
η_{zp}	absolute zero-shear viscosity of the medium
θ *(XRD)*	incident angle of the X-rays
θ *(XRD)*	scattering angle
XRD	X-ray Diffraction
$\lambda(k)$	mean free path of the photoelectron
λ_{gas}	mean free path of gas molecule
$\mu(E)$	absorption coefficient as the function of photon energy
ρ_g	density of the gas
σ *(EXAFS)*	Debye-Waller factor
σ_{AB}	reaction cross section of the collided species A and B
σ_j	thickness of the boundary layer in film growth
σ_s	surface energy
τ_{res}	residence time in the reactor
ϕ	phase shift function

χ	sample thickness
Ω	volume of diffusion species
ω	width of the grain boundary interface
Γ	degree of crystallinity

1 Introduction and Motivation

1.1 Energy Problem and Importance of Solar to Hydrogen Conversion

The world changes rapidly and there is a growing concern regarding our environment and its pollution. Until the end of the 18th century firewood was the main energy source when coal took over that role due to industrial revolution. In the 20th century the fossil fuels – coal, crude oil and natural gas were dominant and still they cover about 80 % of the world energy consumption [Quaschning 2019]. Since the 1850s more than 145 billion tons of crude oil alone were extracted from the Earth's crust. Hazardous effluents are released from fossil fuels to the groundwater and air causing pollution and greenhouse effect [Hoffmann 1995, Arakawa 2001 and Esswein and Nocera 2007]. The International Energy Agency (IEA) estimated that the crude oil and the natural gas will run out in 50 years. The world's population should reach 9.6 billion by 2050 [Tripathi et al. 2019]. Not only due to the growth of population, but also due to increased living standards human mankind faces an ever increased need for energy. Nuclear power would not be a long-term solution, since the uranium sources are limited and need to be enriched, but also the mining process has a huge negative impact on the environment [Quaschning 2016]. The potential of hydropower, geothermal, biomass and wind energy sources are not sufficient to meet the requirements of the future challenges. The largest source of the renewable energy is sunlight and a power of 120000 terawatts (TW) is constantly delivered to the Earth, which is about 4000 times the entire global projected energy demand by 2050 of about 30 TW [Lewis et al. 2005]. To meet the future challenges a breakthrough in chemistry and material science is necessary, as well as development of the new technologies.

The first research on light-driven water splitting emerged by Honda and Fujishima [1972] demonstrating a photoelectrochemical (PEC) cell consisting of a Pt cathode and TiO_2 single crystal anode. Nowadays, electrolysis of water with photovoltaics is currently the best developed technology with an efficiency up to 46 % [Leijtens et al. 2016]. A simpler and cost-effective method to convert water into hydrogen and oxygen on a large scale is photocatalytic water splitting using a slurry

reactor [Pinaud et al. 2013]. Basically, there are two approaches for water splitting: (I) – to combine two photocatalyst materials with use of electron transfer mediators (sacrificial reagents) which is the so called Z-scheme and (II) – single particulate photocatalyst to perform overall water splitting in one step. In the Z-scheme methanol is used for example as an electron donor to facilitate the water reduction by conduction band electrons, while silver-nitrate is used for example as an electron acceptor to promote water oxidation by valence band holes. This inadequacy to evolve both hydrogen and oxygen is the disadvantage of Z-scheme compared to one-step excitation photocatalytic overall water splitting (POWS) systems. To compete with fossil fuels and meet the targeted H_2 price of 2-4 $ per kilogram set by US Department of Energy it is necessary that 10 % of incoming solar energy is used to convert water to hydrogen [Hisatomi and Domen 2019]. Unfortunately, current solar to hydrogen (STH) efficiency is about 1 % on the laboratory scale [Wang et al. 2019]. This work is focused on the development of such a single photoabsorber system.

1.2 State of the Art

There are numerous metal-oxide semiconductors investigated since 1980, such as: TiO_2, ZnO, WO_3, $SrTiO_3$, Fe_2O_3, Ta_2O_5 etc. [Fabian et al. 2015, Zhang et al. 2018]. These materials have wide band gap energies and are unable to harvest energy from solar irradiation and only UV light can be used for hydrogen production. Many of them are incapable of driving the one-step POWS reaction, but perform only a half reaction. Others suffer from poor carrier mobility and short hole diffusion length leading to lower oxygen evolution, as reported for α-Fe_2O_3 [Townsend et al. 2011, Osterloh et al. 2013]. Besides the exploitation of new photocatalyst materials their activation with co-catalyst is very important with surface/interface engineering as fundamental strategy (co-catalyst loading, surface modification and morphology control and surface phase junctions) to obtain high performance [Wang et al. 2019]. An enhanced overall water splitting activity was reported for NiO-loaded Ga_2O_3

and ascribed to an improved charge carrier separation at α-β junctions in the mixed phase α/β-Ga_2O_3 material [Wang et al. 2012]. However, Sakata et al. [2014] reported a diverse correlation between water splitting activity and phase composition of different α- and β-Ga_2O_3 materials when loaded with NiO or Cr_2O_3/Rh as co-catalysts. This is due to different abilities of the α- and β-Ga_2O_3 phase and co-catalysts for the back reaction inhibition. Although Ga_2O_3 has a wide band gap of 4.8-4.95 eV, which requires UV light for water splitting, it is a highly suitable model material to study POWS activity as a function of material properties, such as: phase composition, particle size, degree of crystallinity and surface area. Therefore, this work starts with β-Ga_2O_3 as a basic semiconductor model for further material development, but it can be used to develop and optimize new co-catalyst systems as well. Previously, many metals and metal-oxides have been reported as co-catalyst to improve the water splitting activity. Some co-catalyst used for H_2 evolution are: Pt, Ru, Ni, Au and for O_2 evolution: RuO_x, IrO_x and CuO_x [Grätzel et al. 1981, Kudo et al. 2009, Navarro Yerga et al. 2009, Abe et al. 2010, Yang et al. 2013, Foo et al. 2013, Sakata et al. 2014 and Takata et al. 2015]. When combined, both H_2-evolution and O_2-evolution co-catalysts can significantly improve the activity of the photocatalyst, like co-loaded Rh/Cr_2O_3 co-catalysts, found to be ideal for Ga_2O_3 [Busser et al. 2012]. Domen and co-workers [Maeda et al. 2006, 2007, 2008, 2010 and Sakamoto et al. 2009] have described a Rh/Cr_2O_3 core/shell co-catalyst. The Cr_2O_3 shell is assumed to be permeable to H_2 and protons, but not for O_2, therefore, inhibiting their back reaction to water. Busser et al. [2014] assumed that Cr_2O_3 acts as an oxygen evolution site rather than suppressing the back reaction, which was later confirmed by Soldat et al. [2016]. With respect to noble metal-free co-catalysts as an alternative to the rare and expensive rhodium, a ternary CuO_z/CrO_y/MoO_x co-catalyst system on commercial β-Ga_2O_3 was developed by Busser et al. [2014]. Dopants may improve the absorption properties, but may also act as recombination centers. β-Ga_2O_3 doped with 1-3 at.% of Zn exhibits a seven times higher photocatalytic activity than pure β-Ga_2O_3 for hydrogen evolution [Sakata et al. 2011]. Doping with Zn^{2+} can also result in the formation of $ZnGa_2O_4$ – β-Ga_2O_3 heterojunctions on the surface [Wang et al. 2013]. p-type acceptor levels above the valence

band are formed, which improves the mobility of holes. Substituting a large fraction of Ga^{3+} by Zn^{2+} ions during homogenous precipitation (HP) method leads to the formation of spinel $ZnGa_2O_4$ species and decreased photocatalytic activity [Shimura and Yoshida 2012]. On the other hand, doping with heavy elements, such as Pb^{2+}, leads to a fast decay of the photogenerated electrons and Pb^{2+} ions act as recombination centers decreasing the photocatalytic activity. A photocatalyst can also be doped on the anionic sites, with oxygen being partially replaced by nitrogen to form oxynitrides and control the band structure.

$(Zn_{1+x}Ge)(N_2O_x)$ [Lee et al. 2007] and $(Ga_{1-x}Zn_x)(N_{1-x}O_x)$ [Maeda et al. 2005] are found to be such oxynitrides capable to harvest sunlight and perform overall water splitting. In 2005 a suspension of wurtzite $(Ga_{1-x}Zn_x)(N_{1-x}O_x)$ ($x = 0.14$; E_{BG} = 2.7 eV) solid solution particles were loaded with RuO_2 co-catalysts and evolved stoichiometric H_2:O_2 = 2:1 under visible light. A year later, Maeda et al. [2006] replaced the RuO_2 co-catalyst with $Rh_{2-y}Cr_yO_3$ and enhanced the activity by three times. In 2008, using $(Ga_{0.82}Zn_{0.18})(N_{0.82}O_{0.18})$ particles with loadings of 2.5 wt.% Rh and 2 wt.% Cr based co-catalyst and a post-calcination step at 550°C the activity was even doubled by Maeda et al. [2008] and H_2 evolution activity under visible light was 3090 μmol h^{-1} g_{cat}^{-1}. It was demonstrated by Ohno et al. [2012] that the POWS rate of these materials was stable for three months, while after six months the initial activity dropped by 50 %. Thermodynamically, monoclinic β-Ga_2O_3 and hexagonal α-GaN are the only stable binary phases in the Ga-O and Ga-N systems at ambient pressure and the nitride is less stable than the oxide. GaN can be obtained from Ga_2O_3 by ammonolysis with NH_3 between 500°C and 1000°C following a nucleation and growth model with exclusively Ga_2O_3 and GaN. These are also the only species in the growth of Ga_2O_3 layers during the oxidation of GaN. Therefore, different microstructures are formed for the same nominal Ga-O-N composition. Gallium oxynitrides can be obtained as solid solutions of Ga_2O_3 in GaN with wurtzite structure and as a spinel type Ga_3O_3N (γ-galons) at high pressures [Martin et al. 2009]. There are only a few reports on gallium oxynitrides that are intermediate compounds of the pseudo-binary system Ga_2O_3 – GaN. The nitrogen solubility in

β-Ga_2O_3 is below 2-3 at. % as detected by X-ray and neutron diffraction experiments, which is in strong contrast to the solubility of oxygen in the anion sublattice of GaN, which can reach values even up to 30 at. % [Roehrens et al. 2010]. Other scientific groups studied $(Ga_{1-x}Zn_x)(N_{1-x}O_x)$ using different synthesis techniques, as reviewed by Adeli and Taghipour [2013]. Boppana et al. [2010] synthesized gallium zinc oxynitride with a band gap of 2.5 eV – 2.7 eV by nitridation of spinel zinc gallate produced by sol-gel synthesis. Hu and Teng [2010] reported on wurtzite-type gallium oxynitride with band gaps between 2.2 eV and 2.8 eV formed by nitridation of gallium hydroxide using NH_3 at temperatures between 550°C and 900°C. Hydrogen and oxygen were produced under visible light using sacrificial agents: methanol and silver nitrate solutions. Kim et al. [2011] and Zeng et al. [2013] used metallic Ga, Ga_2O_3 and metal-organic gallium(III)acetylacetonate as precursors to obtain GaN. At temperatures between 950°C and 1000°C NH_3 was flowing over the precursor powder in a quartz tube from 3 h to 40 h. Dharmagunawardhane et al. [2014] obtained a nanocrystalline gallium oxynitride with an indirect band gap of 2.5 eV and a direct band gap energy of 3.69 eV in the same material by ammonolysis of gallium nitrate hydrate. H_2 evolution occurred even without co-catalyst. Chen et al. [2009] monitored the formation of $(Ga_{1-x}Zn_x)(N_{1-x}O_x)$ by in-situ time resolved X-ray diffraction during solid state reaction from mixtures of ZnO-Ga_2O_3 or spinel $ZnGa_2O_4$. It was revealed that $ZnGa_2O_4$ spinel is an intermediate in the formation of $(Ga_{1-x}Zn_x)(N_{1-x}O_x)$ from oxides and imposes a limit on the zinc content in gallium zinc oxynitrides. Combined with the results of density functional theory (DFT) it is found that the zinc content has a big impact on the band gap energy. Systematic insights into the structural and catalytic properties are needed to develop desired $(Ga_{1-x}Zn_x)(N_{1-x}O_x)$ photocatalysts with an atomic zinc content higher than ⅓ and enhanced water splitting activity. This requires the development of new methods, such as rational gas-phase synthesis and post-treatment of highly crystalline doped semiconductors. Not including this work there are no other studies about generation of $(Ga_{1-x}Zn_x)(N_{1-x}O_x)$ from the gas-phase.

1.3 Purpose of the Research

A short overview of the synthesis routes is presented to describe the advantage of the gas-phase method used in this work (Fig. 1.1). There are two approaches for the synthesis of the nanoparticles in general: (I) – top-down, which is based on comminution of larger building blocks and (II) – bottom up strategy, which is based on the formation of clusters and nanoparticles from atomic and molecular species. Mostly, $(Ga_{1-x}Zn_x)(N_{1-x}O_x)$ or solid solutions of GaN-ZnO are synthesized from commercial micropowders Ga_2O_3 and ZnO using solid state reaction and nitridation in NH_3 flow ($\dot{V}$ = 100 – 500 sccm, T = 850°C and t = 5 – 20 h) [Maeda et al. 2005], which is a top-down approach. The bottom-up strategy is advantageous because it is easier to control the desired material properties.

Using different microsized powders as precursors additional mixing and milling processes are necessary for a few hours to obtain smaller particle size and intimate contact between Ga_2O_3 and ZnO. Spinel $ZnGa_2O_4$ is formed during the calcination

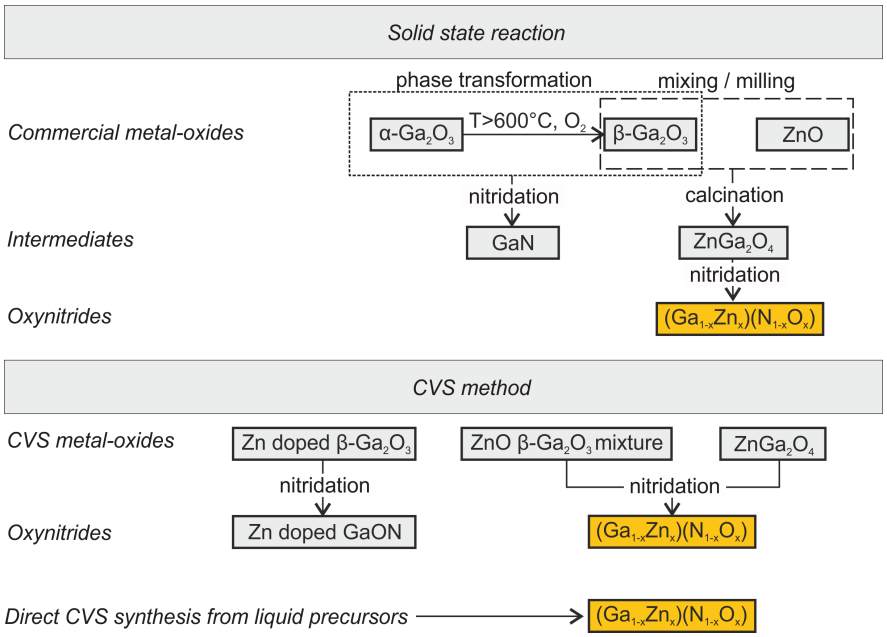

Fig. 1.1: Graphical illustration of the synthesis routes of $(Ga_{1-x}Zn_x)(N_{1-x}O_x)$ and advantage of the CVS method

process by interdiffusion of the constituent cations, which is influencing the growth behavior of the particles. However, powders synthesized from the gas-phase method used in this work are already nanoscaled and no milling is needed. ZnO and Ga_2O_3 particles may be mixed directly in the gas phase achieving intimate contacts in just a few milliseconds while maintaining the high specific surface areas. There are two ways to obtain $(Ga_{1-x}Zn_x)(N_{1-x}O_x)$. One path is to use the synthesized CVS oxide powders as precursors and nitride them in a sequential step. However, thermal nitridation leads to particle growth and loss of Zn due to decomposition of the NH_3 on N_2 and H_2, which reduces ZnO species and volatile metallic zinc leaves the system. The second option is to use appropriate liquid metalorganic precursors (alkyls) to synthesize desired $(Ga_{1-x}Zn_x)(N_{1-x}O_x)$ directly in the gas phase without any additional post-thermal treatments with a precise control of the phase composition. Both ways are bottom-up strategies and considered to be advantageous compared to the conventional solid-state route.

The generation of $(Ga_{1-x}Zn_x)(N_{1-x}O_x)$ with a direct band gap of around 2.6 eV (which has suitable band edge positions to straddle the reduction and oxidation potential of water) is the goal of this work. Chemical composition is just one of many factors to be aware of when aimed to produce a catalytically active material. It is also important to understand the elementary processes of POWS (Fig. 1.2) to design photocatalitically active materials. Step 1 – the semiconductor absorbs the visible light photons with energies larger than the band gap energy and electrons are excited from the occupied valence band to the unoccupied conduction band. Excited electrons leave holes in the valence band and in this initial step electron-hole pairs are generated. Step 2 – electrons and holes are diffusing independently to the surface of the particles. This process is called charge separation. Step 3 – hydrogen is formed by reduction of water by electrons and oxygen by oxidizing water by holes on the surface of the particles [Phivilay et al. 2013]. The hydrogen evolution is accepted to be the rate determining-step [Maeda et al. 2008] and adding a noble metal, such as Rh, generates additional hydrogen evolution sites [Maeda et al. 2006 and Kudo and Miseki 2009]. Step 1 requires a material with an appropriate band structure, as previously described. After charge separation in step 2 it is important that recombi-

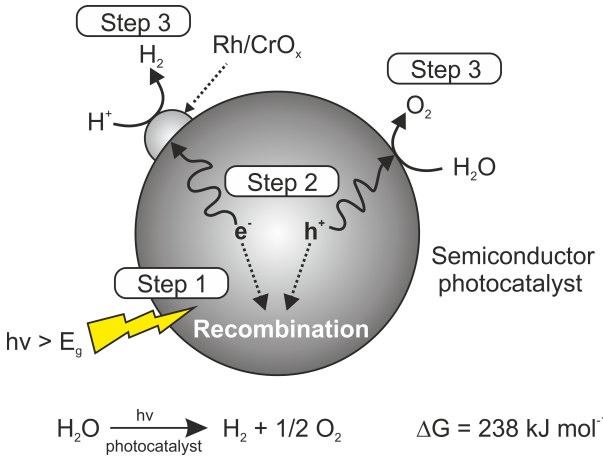

Fig. 1.2: Elementary processes of the overall water splitting: generation and transfer of charge carriers in the bulk of the semiconductor (Steps 1-2) and the redox chemical reactions on the surface of the particles (Step 3). Reproduced from [Maeda et al. 2007]

nation between electrons and holes does not occur during their transport to the particle surface. POWS is an uphill reaction with an increase in free Gibbs energy (Fig. 1.2) and redox reactions are:

$$2H^+ + 2e^- \rightarrow H_2 \quad (1.1)$$

$$H_2O + 4h^+ \rightarrow 4H^+ + O_2 \quad (1.2)$$

A good carrier mobility will be possible if the nanoparticles are highly crystalline (density of the defects is low). The time for which charge carriers reach the surface can be shortened if the particles get smaller (nanoscaled). In step 3, for the surface chemical reaction a large surface to volume ratio, as well as a high density of the active sites is very important. However, with increase of the specific surface area the surface energy increases and one of the main difficulties is instability of the nanoparticles, now more prone to aggregation. Those demands can be met by exploiting the advantages of the Chemical Vapor Synthesis (CVS) method to synthesize nanocrystalline β-Ga_2O_3, intimate mixtures of β-Ga_2O_3 – ZnO, $ZnGa_2O_4$ or

GaN. By adjusting the CVS process parameters, such as: temperature, system pressure and precursor evaporation rate it is possible to improve particle characteristics, such as: particle size, crystallinity and specific surface area. However, optimization of the existing synthesis process is not always sufficient enough to substantially change the material properties. Development of new technologies or modification of existing processes is often necessary followed by use of different precursors. One example is the improvement of nitridation techniques to obtain oxynitrides from CVS synthesized Ga and Zn based oxides with a better control of phase composition. Another example is the combination of the CVS method with the use of metalorganic gallium precursor in order to reduce particle size and chemical purity of GaN phase (not possible with the previously used acetylacetonate precursor). Safe handling of metalorganic precursor completely under inert atmosphere, as well its delivery to the reactor requires the design of new precursor evaporation unit, which is technically the most demanding challenge of this thesis. Finally, the quality of synthesized nanoparticles is evaluated from the perspective of microcrystal-, local- and electronic-structure, as well from the morphology and surface properties. Throughout this work POWS results (observed in step 3) of the CVS synthesized samples are only shown for internal comparison. Since the tests on CVS samples are always performed under the same conditions using the same equipment the concept of the apparent quantum yield (AQY) is here not considered. AQY is important when comparing photocatalytic activities of the materials illuminated using different setups.

2 Theoretical Background

2.1 Photocatalysts for Overall Water Splitting

The basic principles of the POWS are explained in the introduction and it is important to understand how to tune the band structure and obtain material appropriate for POWS under visible light. Semiconducting photocatalysts can be classified into two categories based on different electronic configurations of the metal cations: d^0 (Ti^{4+}, Zr^{4+}, Ta^{5+}, Nb^{5+}, W^{6+} and Mo^{6+}) with no d-electrons in the outmost orbitals and d^{10} (Ga^{3+}, In^{3+}, Ge^{4+}, Sn^{4+}, Sb^{5+}) with fully occupied outmost d-orbitals. Metal cations form the conduction band (CB) of the semiconductor, while anions form the valence band (VB). Therefore, the bottom of the CB of semiconductors with d^0 transition metals consist of empty d-orbitals. On the contrary, the bottom of CB of semiconductors with d^{10} transition metals consists of d- and hybridized sp-orbitals resulting in increased electron mobility. The semiconductor must straddle the reduction and oxidation potential of water, which are 0 and +1.23 eV versus the normal hydrogen potential (NHE) at pH = 0 (Figure 2.1A). In other words, the band gap of the materials must be greater than 1.23 eV [Fang et al. 2018]. Why are metal-oxides not active under visible light then? Actually, the position of the band edges is the determining factor. For metal-oxides the bottom of the conduction band is located at a potential slightly more negative than 0, while the top of the valence band is more positive than 3 eV [Scaife 1980]. To develop a material with appropriate band structure for harvesting the energy of the sunlight doping of the wide band gap metal oxides is one solution. Atomic sites in the host material, in this work β-Ga_2O_3 made by CVS, is replaced by doping. With addition of dopants, such as cationic Zn^{2+} and anionic N^{3-}, the valence band maximum (VBM) will be shifted up. For the hydrogen evolution the conduction band minimum (CBM) must be more negative than 0 eV vs NHE and sometimes doping with a certain metal cation could lead to a shift of the CBM to positive values. In this case hydrogen evolution reaction would not be possible (see Fig. 2.1B) and CBM should remain unchanged. A partial or full substitution of O^{2-} with N^{3-} is possible due to their similar ionic radius of 1.46 Å and 1.41 Å, respectively [Takata et al. 2016 and Wang et al. 2017]. These

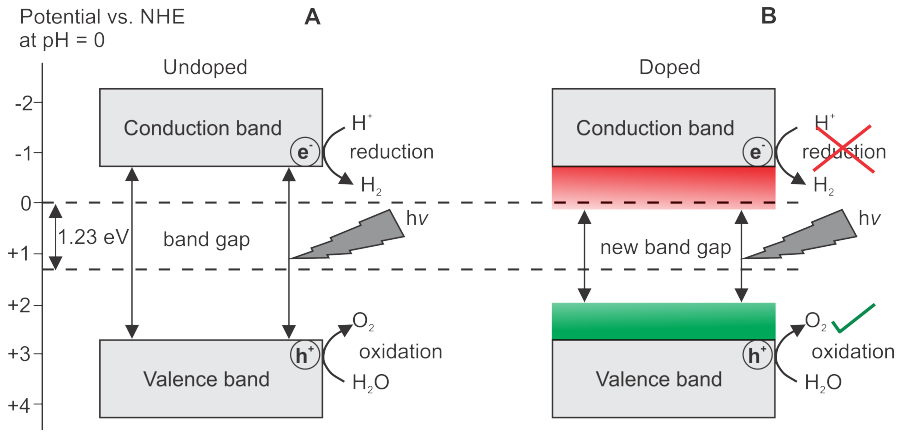

Fig. 2.1: Energy scheme of overall water splitting on a photocatalyst. **A** – undoped metal-oxide photocatalyst and **B** – doped metal-oxide with i.e. Zn^{2+} and N^{3-} to form the oxynitrides. Changed and adjusted from [Takata et al. 2015]

interactions between Zn 3d, N 2p and O 2p orbitals and tuning of the band structure are explained in chapter 4.3 with corresponding examples. However, substitution of the O^{2-} with N^{3-} can lead to the generation of the oxygen vacancies as undesirable effect. The same may occur when Ga^{3+} is substituted by Zn^{2+} and furthermore these impurity levels often provide discrete energy level in the forbidden band rather than an energy band. This can lower the efficiency of the charge generation process or obstruct their migration in the bulk or at the surface [Maeda et al. 2016]. In Fig. 2.1 the presented band gap is an electronic band gap and it can differ from the optical band gap, depending also from the measurement method. An electronic band gap is the energy difference between CBM and VBM or more precise between the highest occupied and the lowest unoccupied electron state at absolute zero temperature. If the positions of the bands are measured by an electron spectroscopy (e.g. tunneling spectroscopy) an extra electron is injected during the process and it needs to overcome the Coloumb repulsion caused by all other electrons in the material. On the other hand, to observe the optical band gap (as described in chapter 3.4.4) the absorption coefficient as a function of the wavelength is measured and the charge state of the material remains unchanged. In other words, a photon has just enough energy to create the electron-hole exciton, but not enough energy to separate them, while

the number of electrons before and after the excitation remains the same. If the semiconductor has a direct band gap than the electronic and the optical band gaps are equal. On the contrary, if the semiconductor has an indirect band gap the electronic band gap is slightly larger than the optical band gap. In general, for the metal oxides or oxynitrides this difference is not so significant as it is for the organic semiconductors (e.g. OLEDs).

After irradiation with UV or visible light the photogenerated electron-hole pair can either recombine or take part in redox reactions. The recombination process becomes very fast and takes a few nanoseconds and most of the electron-hole pairs recombine with dissipation of heat. On the other hand, their migration to the surface is a slow process that usually takes a few hundreds of nanoseconds or even milliseconds [Cossi et al. 2002 and Wang and Liu 2009]. If the photocatalyst is nanoscaled the path to the surface is shorter and, therefore, the probability is higher that charge carrier will reach the surface. The smaller the particles are the higher their specific surface area is, which represents the largest defect of the material. Linsebigler et al. [1995] and Hoffmann et al. [1995] reported that if the diameter of the nanoparticles is less than 10 nm due to quantum confinement effect the optical and electronic properties of semiconductor changes to that of quantum dots. As a result, the band gap increases and band edge positions are shifted to yield larger redox potentials, which affects the photocatalytic activity of the material. An increase in the effective band gap for ZnO nanoparticles is demonstrated when particle diameter decreases from 8 nm to 4 nm (Fig. 2.2). If the charge carrier transfer is the rate-limiting step, the quantum size effect and very small nanoparticles may increase the photoefficiency of the system. Additionally, the density of the surface defects due to a large surface area controls the photoreactivity. Essential steps for the successful POWS reaction are therefore: efficient separation of the photogenerated charges, rapid transfer of the electron-hole pairs to the surface without prior recombination or trapping by defects and the surface catalytic reaction between adsorbed species and photoexcited charge carriers. These steps are affected by many factors, such as: crystal structure of the material, particle size, crystallinity, surface

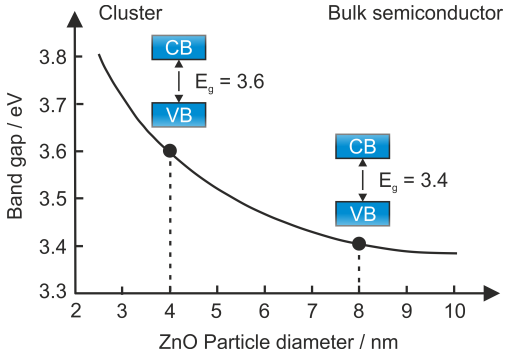

Fig. 2.2: Quantum size effect on bandgap of ZnO semiconductor. Reproduced and adjusted from [Linsebigler et al. 1995]

morphology and area, surface structure, type of the co-catalyst, various adsorption capacities for oxygenated species and acid-base behavior.

2.2 Gallium Based Oxide, Nitride and Oxynitride Materials

β-Ga_2O_3 is a metal-oxide with d^{10} electronic configuration and a band gap of 4.8 eV – 4.9 eV able to absorb UV light with a wavelength below 280 nm [Maeda et al. 2011]. It exists in several polymorphs, such as: α, β, γ, σ and ε. α-Ga_2O_3 is a low temperature phase usually obtained by decomposing precipitated and aged $Ga(OH)_3$ over 500°C and occurs in the corundum α-Al_2O_3 crystal structure. Thermodynamically, the most stable phase is β-Ga_2O_3 obtained above 600°C and via CVS method the only phase obtained with high purity (melting point T_m = 1725°C). β-Ga_2O_3 has a monoclinic crystal structure (Fig. 2.3A). The O^{2-} ions are packed in a distorted cubic closest arrangement, while the Ga^{3+} ions occupy tetrahedral and octahedral lattice sites (Fig. 2.3B-C) with Ga-O bond lengths of 1.83 Å and 2.00 Å, respectively [Geller et al. 1960]. The lattice parameters of the bulk β-Ga_2O_3 reported by Kohn et al. [1957] are a = 12.23 ± 0.02 Å, b = 3.04 ± 0.01 Å, c = 5.80 ± 0.01 Å and $\alpha = \gamma = 90°$ and β = 103.7 ± 0.3°. When the particles are nanoscaled there are small differences in length of the lattice parameters for Ga_2O_3 compared to bulk, as well for all other materials made from the gas phase. GaN is a III/V semiconductor with a band gap of 3.4 eV, and appear as well as ZnO (II/VI semiconductor group) with

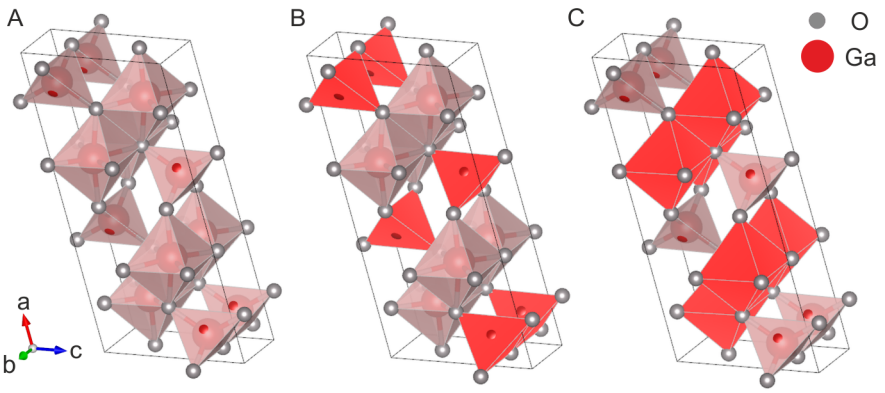

Fig. 2.3: A – β-Ga_2O_3 with monoclinic crystal structure, **B** – Ga(I) in tetrahedral sites and **C** – Ga(II) in octahedral sites (presented by using visualization software VESTA)

a band gap of 3.2 – 3.3 eV in the wurtzite crystal structure (Fig. 2.4) with closely matched lattice parameters (GaN: $a = 3.186$ Å, $b = 5.186$ Å [Levinshtein et al. 2001] and ZnO: $a = 3.249$ Å, $b = 5.207$ Å [Klingshirn 2010] with $\alpha = \beta = 90°$ and $\gamma = 120°$). Without changing the wurtzite structure GaN and ZnO are interchangeable by isomorphic substitution in a solid solution of GaN:ZnO, what is actually $(Ga_{1-x}Zn_x)(N_{1-x}O_x)$ [Adeli and Taghipour 2013]. GaN appears as a yellow powder, while ZnO is pure white. Both materials can be directly synthesized via CVS, but

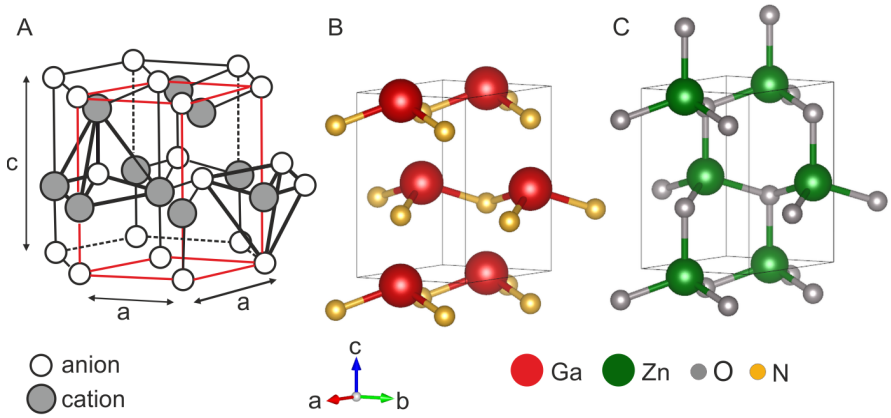

Fig. 2.4: A – Hexagonal crystal structure in general (CorelDRAW X8 software used for schematic presentation) and unit cells (wurtzite phase) of **B** – GaN and **C** – ZnO (presented by using visualization software VESTA)

GaN can be also a product of nitridation of CVS β-Ga_2O_3 (see chapter 4.3). Another material which can be synthesized directly from the gas phase and used as CVS precursor material for obtaining $(Ga_{1-x}Zn_x)(N_{1-x}O_x)$ is the spinel zinc gallate, $ZnGa_2O_4$. It is a wide-band gap semiconductor with a band gap energy of approximately 5 eV and with a cubic spinel structure with lattice parameters $a = b = c =$ 8.335 Å, and $\alpha = \beta = \gamma = 90°$ (Fig. 2.5). Ga^{3+} ions occupy the octahedral sites with Ga-O bond length of 1.90 Å, while Zn^{2+} occupy tetrahedral sites with bond length Zn-O of 2.03 Å. Chen et al. [2009] explained in detail the effects of different starting materials, such as mixture of ZnO-Ga_2O_3 and $ZnGa_2O_4$ on the final properties of $(Ga_{1-x}Zn_x)(N_{1-x}O_x)$. During the nitridation the spinel is converted to wurtzite (the solid solution GaN/ZnO). Zn ions are initially in tetrahedral positions and remain there without the need of reconfiguration. The Zn-O bond in $ZnGa_2O_4$ is shorter than the Zn-O in ZnO and needs to get elongated. In contrast, Ga^{3+} ions are rearranged from tetrahedral to octahedral sites and at least two Ga-O bonds are broken, while oxygen is removed and substituted by nitrogen during nitridation. Comparing the bond enthalpies of Zn-O (1.65 eV) and Ga-O (3.66 eV) it is clear that breaking the Ga-O bond is a rate limiting step of the phase transition into the wurtzite structure [Linde 1993]. The elongation of the Zn-O bond during the phase transition leads to more facile breaking and, therefore, the depletion of metallic Zn from the structure. Since the Zn^{2+} ions are incorporated into the crystal structure of the spinel

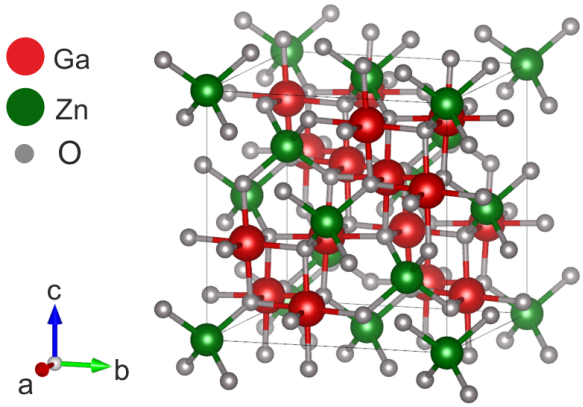

Fig. 2.5: Zinc gallate ($ZnGa_2O_4$) with a cubic spinel structure and Zn:Ga ratio of 1:2 (presented by using visualization software VESTA)

$ZnGa_2O_4$ it is expected that the Zn will abandon the structure slower than in physical mixture of ZnO-Ga_2O_3 where ZnO is free and easier to reduce. The ratio Zn:Ga in the spinel $ZnGa_2O_4$ is 1:2 structure and the maximum Zn/(Zn+Ga) ratio is 0.33. If Ga_2O_3 and ZnO react and form $ZnGa_2O_4$ during the synthesis this ratio can always be maximally 0.33 regardless how much ZnO was present in the beginning. Surplus amount of Zn species (when Zn:Ga > 1:2) will form ZnO, while the rest of Zn will react with Ga and O to form spinel $ZnGa_2O_4$ structure. This addition of the surplus ZnO is found to promote the crystallization of the oxynitride and controls the Zn content [Sun et al. 2007]. Because of the interaction of the Zn 3d with O 2p and N 2p orbitals, causing a so called p-d repulsion, the VBM is shifted and the band gap is narrowed improving the photocatalytic activity [Maeda et al. 2005]. With decrease of the Zn content this shift will not be so pronounced and the activity decreases (Fig. 2.6). It is possible to increase the Zn content using mixtures of ZnO-Ga_2O_3, but since the $ZnGa_2O_4$ intermediate is formed the final Zn/(Zn+Ga) ratio will always be limited. Jensen et al. [2008] predicted that a Zn/(Zn+Ga) ratio of 0.5 will lead to smallest band gap energy and the highest activity using density functional theory (DFT). Some higher values can be reached at the disadvantage of the crystallinity of the materials, but their activity will not be improved.

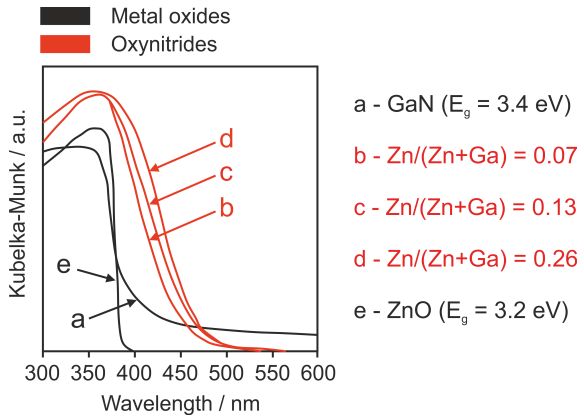

Fig. 2.6: Higher Zn/(Zn+Ga) content narrows the band gap energy of the oxynitride shifting the wavelength to higher values (as an orientation for the ratio of 0.13 is E_g = 2.58 eV) (**b-d**) compared to pure GaN (**a**) and ZnO **(e)** active only in deep UV region around 400 nm. Reproduced from [Domen et al. 2005]

2.3 Chemical Vapor Synthesis (CVS)

Chemical Vapor Synthesis (CVS) is basically a modified Chemical Vapor Deposition (CVD) method used to synthesize nanoparticles from the gas phase instead of films [Winterer 2002]. The gas phase reactions depend on process parameters (pressure, temperature, flow conditions, substrate, reactor type and length, composition of the gas phase etc.). Breiland and Ho [1993] observed 'snowing' in the reactor during CVD, which means the formation of ultrafine nanoparticles as byproducts contaminating the films. In CVS processes the mean free path length λ in the reactor is small compared to the reactor diameter d_r. The ratio is presented by the dimensionless Knudsen number and CVS operates always in the continuum flow regime ($K_n < 1$). In Figure 2.5A the deposition rate J_{dep} (film growth rate) as a function of temperature, which is just one of the adjustable process parameters, is shown, as well the transition from CVD to CVS regime. Three regions can be observed. (I) – at lower temperatures, higher concentration of evaporated precursor matter is transported to the substrate surface. The film growth rate (heterogeneous nucleation) is kinetically controlled following an Arrhenius law:

$$J_{dep} = A_0 \cdot \exp(-\frac{E_A}{RT}) \tag{2.1}$$

limiting the surface reaction. (II) – when increasing temperature, the synthesis reaction speed increases and reaches a plateau. In this area the reaction speed is so high that a concentration boundary layer is formed at the substrate surface. The deposition rate is then determined by the diffusion of the reaction species through the boundary layer:

$$J_{dep} = D \cdot \frac{n_r}{\delta_j} \tag{2.2}$$

where: D – diffusion coefficient of the species, n_r – gas concentration of the reactive component and δ_j – thickness of the boundary layer. (III) – if the temperature increases further, the deposition rate decreases due to generation of supersaturated va-

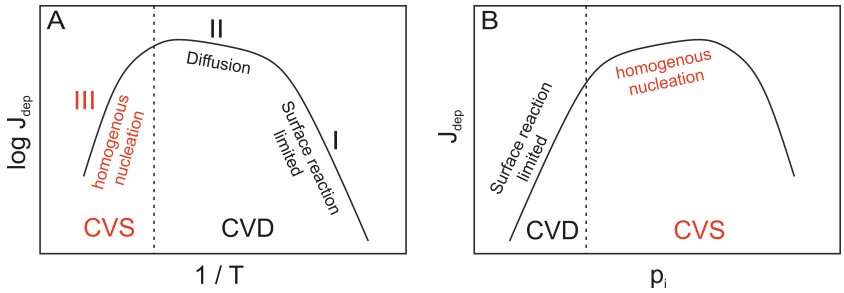

Fig. 2.5: Influence of the temperature (**A**) and precursor partial pressure (**B**) on the film growth rate in CVD and moment when in reactor is starting 'to snow' and nanoparticles are formed by CVS. Adapted from [Kodas and Hampden-Smith 1994]

por and in this moment the 'snowing' in the reactor starts. When the precursor partial pressure p_{pr} is high enough the formation of the nanoparticles is then initiated by homogeneous nucleation (Fig. 2.5B). This typical CVD curves are described by Kodas and Hampden Smith [1994]. Process parameters can be adjusted to switch from CVD to CVS from heterogeneous to homogeneous nucleation. CVS is favored at high temperatures, high partial pressures of monomers at a low vapor pressure of the bulk solids, long residence times in the reaction zone (long reactors or low gas flows). The residence time τ_{res} is calculated from the ratio of the volume of the CVS reactor $V_{reactor}$ to the volume flow dV/dt through the reaction zone:

$$\tau_{res} = \frac{V_{reactor}}{dV / dt} \tag{2.3}$$

Disadvantages of the CVS method are the agglomeration of the collected particles, complex synthesis setups and high-energy consumption. Despite aforementioned drawbacks CVS can produce nanoparticles of very high purity, narrow particle size distribution, high crystallinity and large surface to volume ratio, which correspond to the requirements of the POWS.

2.3.1 Fundamentals of Gas to Particle Conversion

For homogeneous nucleation to occur it is necessary to generate a state of a supersaturated vapor consisting of atomic or molecular species with partial pressures higher than the corresponding equilibrium vapor pressure. The supersaturated vapor can be either formed by chemical reaction, such as irreversible decomposition of the precursor (in CVS) or by physical processes, like rapid cooling when the vapor pressure of the species is decreased. The first step in CVS is the decomposition of the precursor and conversion into monomers. The monomers move in Brownian motion, collide and stick to each other to build clusters. In collision with other monomers clusters can grow and the concentration of the monomers decreases (reduction of supersaturation) followed by decrease in free energy of clusters. Thermodynamically, this state is unstable until spherical nuclei with a critical radius r^* is reached and a new surface is created with tendency to reduce surface tension. Until the critical radius is not reached the cluster can separate into monomers back. Beyond the critical radius, which is an irreversible process, the primary particles are formed and they can only grow further on. Particle growth can proceed in two ways: by condensation and by coagulation [Hinds 1999]. If the concentration of the particles is low the collision probability between particles also decreases and the growth

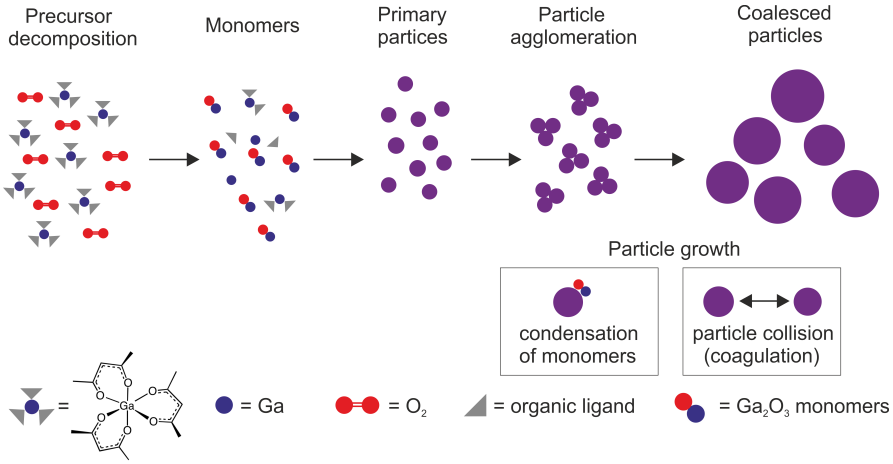

Fig. 2.6: Schematic representation of the physicochemical processes during CVS by gas to particle conversion – generation of Ga_2O_3 from $Ga(acac)_3$

mechanism proceeds by monomers condensing onto existing particles [Kodas and Hampden-Smith 1999]. These basic physicochemical processes of the particle generation in the gas phase are presented in Figure 2.6 and formation of Ga_2O_3 nanoparticles from Ga(III)acetylacetonate precursor is used as an example.

Precursor decomposition

In this work different nanoparticles are synthesized, as previously described. Solid precursors such as: Ga-, Mn-, Rh- and Fe-acetylacetonates and Zn-tetramethyl-heptanodionate are used either for synthesis of nanoparticles or for doping. The combustion / pyrolysis of solid precursors in presence of oxygen generate the desired metal oxides, as well as water and carbon-dioxide as byproducts. Because of the presence of oxygen in the structure of the solid precursors they are generally not applicable for synthesis of nitrides. Therefore, liquid Ga metal-alkyls are used for synthesis of gallium nitride. Due to the variety of the precursors employed in this work the thermal decomposition of the main precursors is presented in Chapter 4 - Results. Simplified, the kinetics of the thermal decomposition can be described as irreversible pseudo first order reaction:

$$\frac{dN_{pr}}{dt} = -k_r \cdot N_{pr} \tag{2.4}$$

where: N_{pr} – number density of the precursor molecules, k – reaction constant [Okuyama et al. 1990] and can be calculated as:

$$k = k_0 \exp(-\frac{E_A}{k_B T}) \tag{2.5}$$

where: k_0 – pre-exponential factor, E_A – the activation energy, k_B – Boltzmann constant and T – process temperature.

Coagulation

The primary nanoparticles generated by precursor decomposition move in the gas phase by Brownian motion and coagulate forming agglomerates, thus increasing

their size [Hinds 1999]. While the number of agglomerates increases the total number of the primary particles decreases due to collision and coagulation. The number density of the agglomerates N_a depends on the collision frequency β:

$$\frac{dN_a}{dt} = -\frac{1}{2}\beta N_a \tag{2.6}$$

Considering monodisperse particles [Fuchs 1965] the collision frequency β and the rate of change in the agglomerate number density due to Brownian coagulation mechanism [Pratsinis 1988, Seinfeld and Pandis 1998] is given as:

$$\beta = 4\pi \cdot D_p \cdot d_c \cdot \left(\frac{d_c}{2d_c + 2\sqrt{2} \cdot g} + \frac{2\sqrt{2} \cdot D_p}{c_p \cdot d_c}\right)^{-1} \tag{2.7}$$

where: D_p – particle diffusion coefficient, d_c – collision diameter of the agglomerate, c_p – average particle velocity, g – transition parameter from free molecular ($K_n >> 1$) to continuum regime ($K_n << 1$), where K_n is the particle Knudsen number. The particle diffusion coefficient D_p is directly proportional to temperature T and indirectly to gas viscosity η_g and particle collision diameter d_c. If the particle diameter is significantly smaller than mean free path of the gas ($d_p << \lambda_{gas}$) than the transition parameter is much larger than collision diameter ($g >> d_c$). The collision diameter d_c of an agglomerate is described by:

$$d_c = d_p \cdot \left(\frac{A_{ag}^3}{36\pi \cdot V_{ag}^2}\right)^{1/D_{fr}} \tag{2.8}$$

where: d_p – primary particle diameter, V_{ag} – volume of the agglomerate, A_{ag} – surface area of agglomerate and D_{fr} – fractal dimension of the agglomerate. [Winterer 2002] describes that the collision and agglomerate diameters are identical if the fractal dimension $D_f = 3$. The coagulation time t_c represents the time for which the number density of particles is reduced by half and can be estimated as:

$$t_c = \frac{1}{\beta N_A} \tag{2.9}$$

If the volume of agglomerate V_{ag} is compared to the volume of the primary particle V_p the number of the primary particles Z_{pp} contained in an agglomerate can be estimated as the degree of agglomeration:

$$Z_{pp} = \frac{V_{ag}}{V_p} \tag{2.10}$$

Coalescence

Coalescence is the process in which two or more particles merge forming sintering necks during their contact producing new bigger particles. Due to the tendency of agglomerates to reduce their surface energy they coalesce decreasing the surface area. The characteristic coalescence time t_{sinter} is limited by grain boundary diffusion process [Winterer 2018] and can be expressed as:

$$t_{\text{sinter}} = \frac{k_B \cdot T \cdot d_p^4}{16\sigma \cdot \omega \cdot \Omega \cdot \gamma \cdot D_{gb}} \quad ; \quad D_{gb} = D_0 \cdot \exp(-\frac{E_{gb}}{k_B T}) \tag{2.11}$$

where: d_p – primary particle diameter, k_B – Boltzmann constant, T – process temperature in the gas phase, σ – sintering constant, ω – width of the grain boundary interface, Ω – volume of diffusion species, γ – surface free enthalpy, D_{gb} – grain boundary diffusion coefficient, D_0 – pre-exponential factor, E_{gb} – activation enthalpy of diffusion. Friedlander [2000] explained the influence of sintering and collision rate (coagulation) on the formation of the final particles and nature and strength of the bond between them (Fig. 2.7). Particles will be rapidly sintered / coalesced if the sintering time is much shorter than the collision time and spherical new bigger particles are formed. When the rates approach each other two types of than the sintering rate the particles will be sintered only partially and form hard agglomerates. On the other hand, if the sintering speed increases and it is much faster than the collision rate the sintering necks are formed between the particles and hard coalescence to obtain non-agglomerated particles.

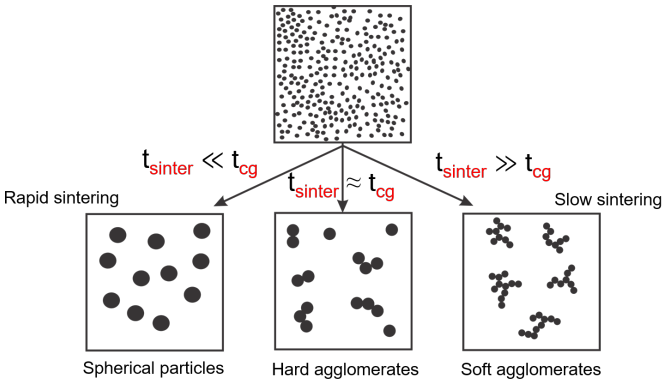

Fig. 2.7: Influence of collision rate (coagulation) and sintering rate on formation of soft and hard agglomerates or single new bigger particles. Reproduced from [Friedlander 2000]

Particle collection by thermophoresis

Formed particles are separated from the gas phase in the particle collector based on the thermophoretic effect. The thermal force and particle motion are always in direction to the colder surfaces (decreased temperature). Mobile particles in the gas phase respond to the temperature gradient between the hot gas stream and the cold stainless steel walls of the collector and stick to the walls. The deposition mechanism of the particles on the walls of the collector is well documented by Schilling et al. [2014]. Where in the collector the particles will be deposited depends on their velocity V_{tp}, which is dependent on thermophoretic force F_{tp} and this one is proportional to particle size d_p and temperature gradient ∇T [Hinds 1999]:

$$F_{tp} = -\frac{p \cdot \lambda \cdot d_p \cdot \nabla T}{T} \tag{2.12}$$

$$V_{tp} = -\frac{n_g \cdot \nabla T}{T \cdot \rho_g} \tag{2.13}$$

where: p – gas pressure, λ – mean free path, T – absolute temperature of the particle, η_g – viscosity of the gas and ρ_g – density of the gas. Schilling [2014] simulated the process of particle deposition on the walls of the collector with variation of the process parameters. One of the disadvantages of this type of the collector is the drop in

collection efficiency within a time by increasing the layer thickness of deposited particles on the wall acting as thermal insulation. Moreover, the particles are exposed to ambient air when opening the collector, which has a negative influence on the GaN nanoparticles as they easily oxidize, particularly if they have a high surface area.

3 Experimental methodologies

3.1 Modular Design of CVS Setup and Unit Operations

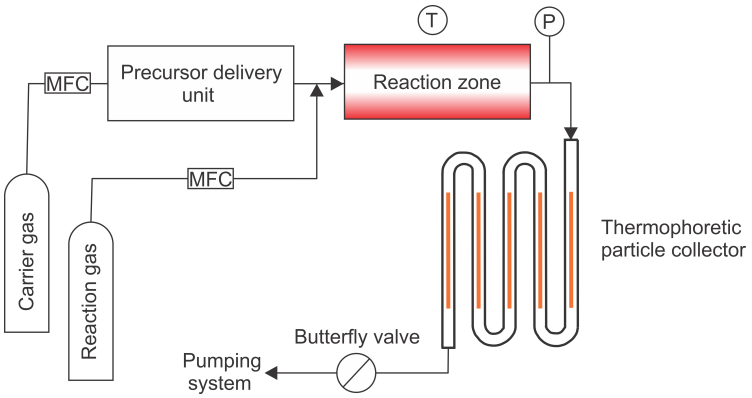

Fig. 3.1: Schematic presentation of the CVS system in general

In general, the experimental CVS setup is divided into four segments: a gas supply with a precursor delivery unit, a reactor, a thermophoretic particle collector and a pressure control unit (Figure 3.1). This system is modular enabling the addition or modification of improved or new parts.

Gas supply and precursor delivery unit*:* Gas flows are regulated by thermal mass flow controllers connected to a central microprocessor unit (*Multi Gas Controller 647C, MKS*). Helium (*Air Liquide, Alfagaz 1*, 99.9999 %) is used as a carrier gas through the precursor delivery zone being saturated with precursor vapors delivering them to the reactor. Helium has a high thermal conductivity and it is, therefore, advantageous over nitrogen to use as an inert carrier gas. As a reaction gas either oxygen (*Air Liquide,* Purity 5.1, 99.9991 %) or ammonia (*Air Liquide,* 99.999 %) are used for the synthesis of oxides or nitrides, respectively.

Depending on the precursor state – solid or liquid, the evaporation method differs and precursors are delivered to the reaction zone in gas state. The flow rate of carrier and reaction gases differ (600 / 1700 sccm and 50 / 1200 sccm, respectively). Solid precursors are placed into a boat made of MACOR (a machineable glass-ceramic) and thermally evaporated using heating mantles positioned around the alumina tube. Unlike sublimation process where solids transform directly to gas these solid precursors melt forming an intermediate liquid phase. The main solid precursors used

in this work are gallium(III)acetylacetonate ($Ga(acac)_3$; T_m = 196ºC; M = 367.05 g/mol) and bis(2,2,6,6-Tetramethyl-3,5-heptanedionato)zinc ($Zn(TMHD)_2$; T_m = 134ºC; M = 431.92 g/mol). Koponen et al. [2016] reported about selection criteria for volatile solid precursors. It is advantageous to use liquid precursors in a more efficient process to minimize precursor waste and reduce processing time at constant vapor pressure. In other words, the surface area from which the liquid precursor is depleted is constant and continually refreshed and, therefore, the evaporation kinetics do not change. This is not the case for the solid precursors, where evaporation depends on particle size, which may vary from batch to batch and manufacturer. The vapor pressure of solid and liquid precursors can be estimated using Antoine equation:

$$p_{pr} = 10^{(a-\frac{b}{T})} \tag{3.1}$$

where: a and b – Antoine parameters specific for each substance, T – temperature in K and p_{pr} – partial pressure of the precursor (when equal with the system pressure the evaporation is uncontrolled).

Liquid precursors used in this work are triethylgallium (TEG; M = 156.9 g/mol) and diethylzinc (DEZ; M = 123.5 g/mol) from the group of metal-alkyls. These very reactive substances are placed inside a stainless steel bubbler kept at a constant temperature (-5ºC) using an oil bath. Helium gas (50 sccm) is passed through the bubbler to get it saturated with a vapor of the liquid precursor. Metal-alkyls are dangerous during handling and to use them we developed a novel system for precursor delivery to do so. Due to its complexity and importance not only for this, but also for future work, this unit is presented in chapter 3.1.1 in more details.

Tube furnace as reaction zone: The reaction in the gas phase takes place inside an alumina tube with an inner diameter of 18 mm placed inside a resistance tube furnace. In this work a resistance furnace with a total heated length of 900 mm (*STF Carbolite, T_{max} = 1650°C*) is used for synthesis of Ga_2O_3, $ZnGa_2O_4$ and GaN. For the mixture of the ZnO-Ga_2O_3 nanoparticles a second resistance furnace is added in line with a total heated length of 400 mm (*Carbolite MTF12/38/400w T_{max} = 1200°C*). If the Zn and Ga source are added before the first reactor they will mix

immediately in the reaction zone and form spinel $ZnGa_2O_4$. If the Ga_2O_3 nanoparticles are already formed in the first reactor and Zn source is added between the first and the second reactor the Ga_2O_3 and ZnO nanoparticles will be physically mixed or form core-shell structures. Those variations of the modular CVS system are schematically shown in Figure 3.2.

Particle collector: the synthesized nanoparticles are separated from the gas phase in a thermophoretic collector. It has a meander-shape to increase the total powder collection efficiency. Temperature gradient is established by quartz lamps positioned in the channels ($T \approx 500$°C), while the stainless steel walls are cooled by water ($T \approx 20$°C). Particles move towards the colder surface. They are deposited on the walls and after opening the collector they can be collected being exposed to the ambient atmosphere at the same time. The main drawback of this type of the collector is reaction of air with nanoparticles, which leads to oxidation of the nitride nanoparticles. Air humidity is adsorbed on the surface of the nanoparticles as well.

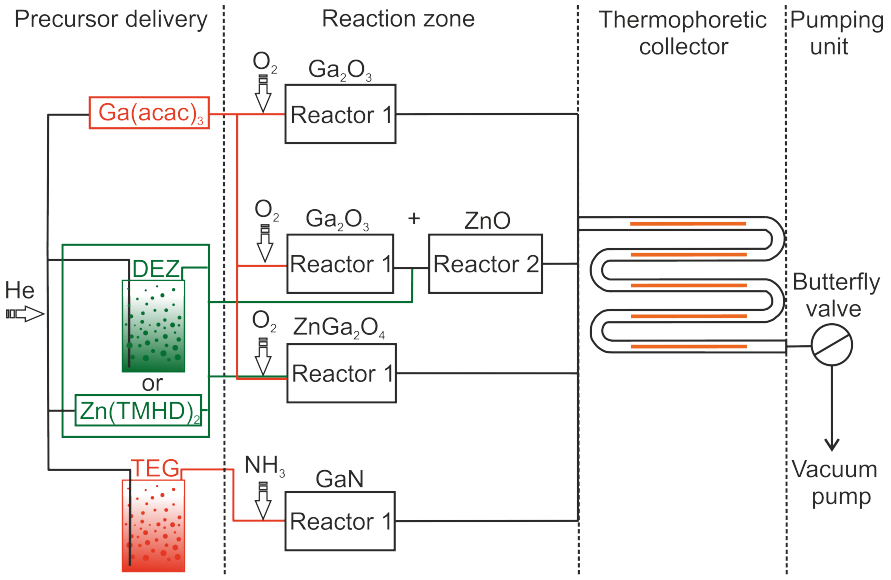

Fig. 3.2: Variation of the precursor delivery unit / reaction zone for generation of nanoparticles with different chemical composition

It has to be added, that during the synthesis there is a danger of cyanide formation as the side-product in reaction of ammonic acid with metalorganic precursors. To minimize this risk, the system is evacuated and refilled with nitrogen five times. A person who carries out experiments is obligated to wear a special protective mask with corresponding filter and sensor is used to detect possible presence of cyanides.

Pressure control unit: Low pressure (20 mbar for liquid and up to 300 mbar for solid precursor) is maintained by using a pumping system (dry screw pump, *Busch Cobra NC600A*, 570 $m^3\ h^{-1}$, ultimate pressure < 0.01 mbar). In order to monitor and to keep the system pressure constant a capacitive absolute pressure gauge (*MKS Baratron 1000*) and a butterfly valve are used. In order to have a successful reaction the precursor molecules *A* and reaction gas molecules *B* should have high enough energy (activation energy) when they collide. In general, the number of the collisions Z_{AB} is given by the collision theory in the gas phase:

$$Z_{AB} = \sqrt{2} \cdot \frac{N_A}{V} \cdot \frac{N_B}{V} \cdot \sigma_{AB} \sqrt{\frac{8 \cdot k_B \cdot T \cdot (m_A + m_B)}{\pi \cdot m_A \cdot m_B}} \tag{3.2}$$

where: N/V – Number density of the species, σ_{AB} – reaction cross section of the molecular species that collide, k_b – Boltzmann's constant, T – temperature, m – mass of the reactants. The average distance travelled by a gas species before the collision occurs is called mean free path λ. The choice of the pump and, therefore, vacuum range that can be achieved (coarse: 300-1 mbar, fine: 1-10^{-3} mbar, high: 10^{-3}-10^{-7} mbar, ultra-high: 10^{-7}-10^{-12} mbar) influences strongly the mean free path:

$$\lambda = \frac{k_B \cdot T}{\sqrt{2} \cdot \sigma \cdot \rho} \tag{3.3}$$

The average velocity $\bar{c}$ is directly proportional to temperature and inversely proportional to system pressure. In this work low vacuum is maintained and the gas flow through the alumina tube with the length l_{RT} and inner diameter d_{RT} (18 mm) is laminar. The relation between the mean pressure value $\langle p \rangle$, suction power q_{pV}, conductance L_{VP} of the vacuum pump and pressure difference Δp is given as following:

$$q_{pV} = \frac{\pi \cdot d^4 \cdot \langle p \rangle}{128 \cdot \eta \cdot l_{RT}} \cdot \Delta p \tag{3.4}$$

where: η – viscosity of the gas. If the mean free path of the gas species is longer than the diameter of the reaction tube (when high vacuum is maintained) there will be no collisions and no particles. Chapter 4.1.2.1 shows in more details how strongly the system pressure influences the synthesis process.

3.1.1 Bubbler Box for Handling Metal-Alkyls

Metal-alkyls, such as TEG and DEZ are highly pyrophoric materials. Exposing them accidentally to air in case of a spillage an immediate reaction with oxygen will occur, which leads to ignition and fire. Even worse, in direct contact with water very loud and violent reaction / explosion occurs releasing highly flammable gases. With complete combustion, the fire generates water vapor, carbon dioxide and metal oxide in the form of white smoke. On the other hand, the products of incomplete combustion may be carbon monoxide, some hydrocarbons (alkanes / alkenes) and other hazardous gases. Failure to follow proper handling procedure can lead to serious injuries, death and significant damage to facilities. Therefore, these materials should be handled under inert atmospheres that rigorously exclude the presence of the oxygen / moisture. They are delivered in portable tanks (containers) and it is necessary to work inside a glove box to transfer the metal-alkyls to the stainless steel bubblers suitable for work in the CVS system. Caution is necessary with contaminated syringes, cannulas, glassware, wipes, spatulas, gloves etc. All equipment needs to be decontaminated outside the glove box and there is a risk of ignition and inhalation of the hazardous gases or severe burns if in direct contact with skin or eyes. A standard commercial glove box is used only for storage of such materials or bubbler refilling. To minimize the risk, an alternative strategy is to have the stainless steel bubblers refilled by *Dockweiler Chemicals* (Germany). Additionally, a unique inert gas box, called bubbler box, is designed and constructed. From the aspect of safety this is a very important innovation not only to store the metal-alkyls, but to function as precursor delivery unit. To the best of our knowledge there is no similar system

developed and it would be also very useful for other processes like chemical vapor deposition or atomic layer deposition.

Bubblers with TEG and DEZ are equipped with an K-type thermocouple to measure the temperature inside the liquid during the synthesis providing accurate real-time information. Additionally, an ultrasonic point level system (*Sensaras, PLS9600 Series*) is mounted in the ½" VCR port and designed to detect the level of the liquid inside the bubbler using multiple sensing points. It is not dependent on color, viscosity, dielectric properties or density of the liquid. If the bubbler is empty it is sent for refilling and regular technical service. After delivery the bubbler is placed inside the bubbler box (Fig. 3.3). Specially designed walls of the box have a thickness of 18 mm with a layered structure (metal-foam-metal). Between the aluminum metal plates titanium-based foam is designed to absorb the impact of an explosion. The body itself has dimensions 850/700/700 mm. It is equipped with a window on one side made from 20 mm thick polycarbonate glass with pneumatic sealing and quick release fasteners for easy opening to access the inner space of the box. The butyl gloves are mounted in case of emergency to handle the bubbler dur-

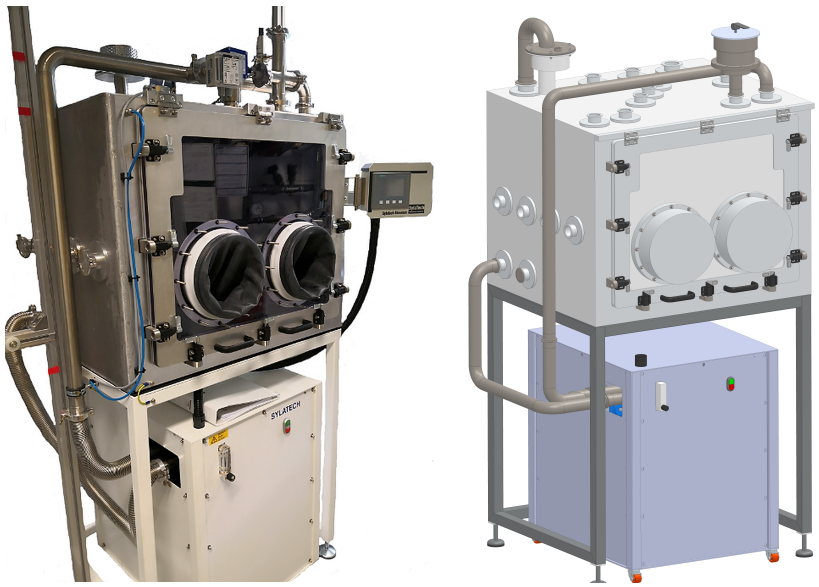

Fig. 3.3: Constructed bubbler box in cooperation with SylaTech GmbH, Germany (left) and designed model of the bubbler box using Pro Engineering Creo Parameters (right)

ing the synthesis, but also to initiate the start / end of the process. DIN ISO KF 40 and KF 50 adapters are mounted on the walls of the chamber and corresponding feedthroughs are installed to connect the bubblers / equipment inside the box with instruments outside of it. The maximum leak rate of the box is 0.05 Vol.% / h (ISO 10648-2). In order to maintain an inert atmosphere (N_2) in the box (O_2 < 1 ppm and H_2O < 1 ppm) a flushing and gas purification system with a capacity of O_2 > 35 L and H_2O > 1400 g is used. Once the copper catalyst is oxidized to copper-oxide the system needs to be regenerated using a gas mixture (95 % N_2 and 5 % H_2) to reduce the catalyst to copper. An electrochemical oxygen sensor with a response time less than 5 s with range 100 – 1000 ppm (*OxyTrans*) and a moisture sensor with range 0 – 3000 ppm monitor the purity status of the atmosphere in the box. The pressure in the box is atmospheric with a standard deviation of ±10 mbar. For safety, there is a special rupture disc which is broken if the pressure rises above 1100 mbar. The box is operated using a controller with a touch screen control unit. Any leakage in the connections between the bubbler and the CVS system must be avoided.

The precursor delivery process from the newly constructed bubbler box is schematically presented in Figure 3.4. Two manual diaphragm high pressure valves *(SS-DSTW4-BL, Swagelok)* are mounted on the bubbler inlet and outlet lines (1). It is required to manually open the valves when starting the synthesis for which the gloves in the bubbler box are used. To exclude the possible risk by handling the manual valves from the close distance three additional high pressure diaphragm pneumatic valves (*3LSS4C-FV, Ham-Let*): outlet (7), bypass (8) and inlet (9) are installed. Each pneumatic actuator is N.C type (normally closed) and nitrogen with a pressure of 3 bar is delivered to actuators pressurizing the membrane and opening the valve. For separate nitrogen supply each actuator is connected to the corresponding port in the multiple pneumatic control valve island, which is connected to the main nitrogen supply line outside the box via feedthrough with VCR high-purity connections. Each port of the island is connected via an electric feedthrough with a valve control process unit, specially designed for this process to open and close the

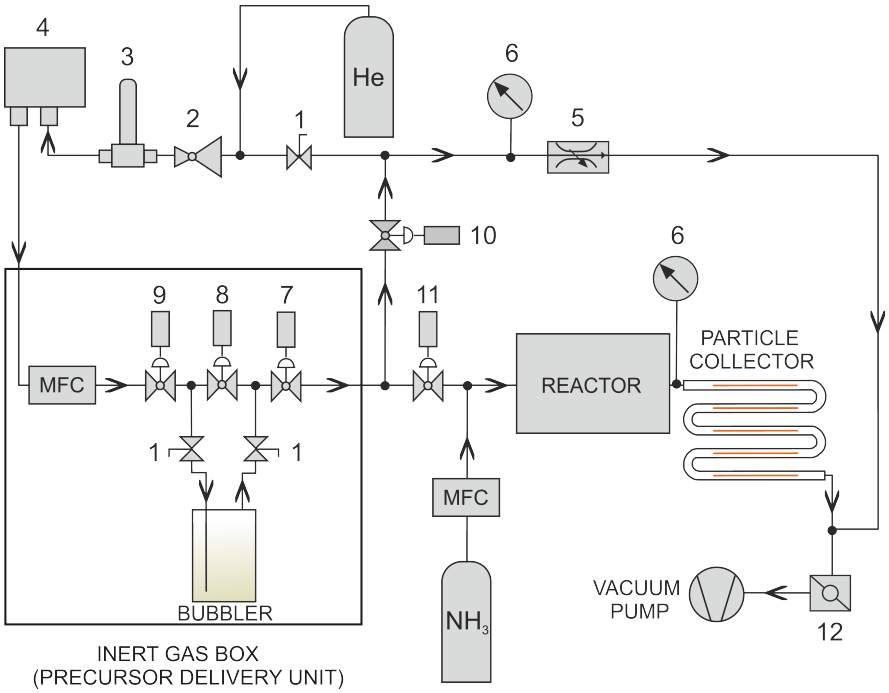

Fig. 3.4: The schematic presentation of the CVS process using specially designed bubbler box as a precursor delivery unit, where: 1 – manually operated valves; 2 – pressure reducer; 3,4 – in-line moisture and oxygen sensors; 5 – proportional valve; 6 – capacitance Baratron manometer; 7-11 – pneumatically operated valves; 12 – butterfly valve

valves from outside. The bubbler is always delivered under inert atmosphere (usually argon) at atmospheric pressure. Due to big pressure difference between bubbler (atmospheric) and CVS system (vacuum) the precursor liquid would be extracted very fast if the valve would be opened abruptly, thus representing a real danger. Therefore, two additional pneumatic valves (*DP6L-FR4-CA, FITOK*) are installed and work on the same principle like previously described valves. Position (11) is the valve to the CVS reaction zone and it is opened only when the synthesis is about to start, otherwise remains closed. Valve (10) is for the bypass line to evacuate the bubbler slowly to the synthesis pressure using the proportional valve (5). The pressure is monitored by a capacitance manometer Baratron pressure gauge. Addition-

ally, a second absolute pressure gauge is placed before the particle collector to monitor the pressure during the synthesis in the reaction line (6). It is strictly forbidden to open the inlet (9), bypass (8) and outlet (7) valves at the same time – vacuum line would be in direct contact with the precursor liquid via inlet tube and due to suction of the liquid the reaction will be uncontrolled and could lead to an explosion. The function of the bypass valve (8) is exactly to prevent this risk during the synthesis when closed and to be able to purge the whole line when opened (if the manual valves are closed). It is advisable to evacuate and refill the bubbler with He at least three times to avoid any contamination. The flow of He is controlled by mass flow controllers (*GE50A, MKS*) with a possible flow rate of maximum 200 sccm. The physical limitation of the flow rate excludes any potential software error which may occur and over pressurize the bubbler if higher flow of the gas would be possible. The supply line of He is connected to in-line ZrO_2 oxygen sensor (*XZR400A2, Michell Instruments*) and moisture sensor (*Pura Online Hygrometer, Michell Instruments*). Since the maximum operating pressure for sensors is 1.5 bar the pressure in the He supply line (initially 200 bar) is decreased using a pressure reducer (2) not to damage the instruments. The oxygen sensor (4) has a very fast response time with a high precision below 0.1 ppm of O_2 (during synthesis the lowest detectable limit was 0.09 ppm) for a He flow of 3 L/h. The moisture sensor (3) measures the dew point in a temperature range from -40°C to -120°C and consists of a polished metal mirror that is cooled at constant pressure until moisture starts to condense on it (dew point). At lower temperatures the moisture amount present in the gas decreases. For precursor delivery the He flow through the bubbler is set to 50 sccm and TEG is kept on the constant temperature of 0°C. The bubbler is placed inside an oil bath in the box to regulate the temperature. Between the walls of the bubbler and the oil bath a spiral heat exchanger is placed and connected via feedthrough with VCR connections to special isolated hoses which withstand temperature of -50°C connected to an oil bath with circulation function (*LAUDA ECO RE 1050 SN,* temperature range from -50°C to 150°C). As a heat transfer medium a polydimethylsiloxane oil (*FRAGOLTHERM X-40,* temperature range from -60°C to 220°C) is used.

3.2 Nitridation Setup

For nitridation of the synthesized powders two different setups are used. In the first thermal nitridation of the powder is carried out in a hot wall reactor at atmospheric pressure using 300 sccm of NH_3 as nitrogen source. The influence of the nitridation time (from 10 min to 10 h) and temperature (from 450°C to 850°C) on particle characteristics is investigated and described in detail in chapter 4. The second type of setup is a combined microwave plasma reactor (MWR) with a hot wall reactor (Fig. 3.5).

The MWR is used to generate reactive nitrogen (radical) species from NH_3 and N_2 at low temperatures. In order to generate a microwave plasma 300 sccm of Ar (*Air Liquide 4.8*) is introduced together with the reaction gas, experimentally found to be the right mixture with adapted gas density to initiate its ionization and formation of the radicals. In the MWR a microwave power of 750 W is used. The plasma glow is pink in color. In the MWR a quartz glass tube with an inner diameter of 18 mm is used and found to give better results compared to an alumina tube. The MWR is positioned very close to the hot wall reactor to decrease the recombination of the formed radicals and to keep the ion flux high. The pressure used in this process is 50 mbar, while under atmospheric pressure the density of the gases is too high and the MWR process is very unstable and impossible to control. A similar setup was used in the work of Ali et al. [2009] for the synthesis of the nanoparticles.

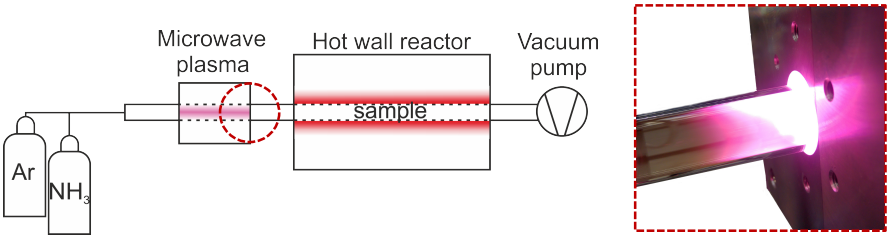

Fig. 3.5: Schematic representation of the nitridation setup (left) using combined microwave plasma reactor and hot wall reactor (T = 850°C, p = 50 mbar, t = 5 h) and afterglow in the MWR of the ionized gas mixture Ar-NH_3/N_2 (right)

3.3 Setup for Photocatalytic Overall Water Splitting

All photodeposition and overall water splitting experiments are performed by G.W.Busser, J.Menze and P.Weide [Ruhr-University Bochum, Laboratory of Industrial Chemistry].

Co-catalyst photodeposition / overall water splitting experiments are carried out in a specially designed three-phase reactor (Fig. 3.6) with continuous on-line detection of the generated gases. Nanoparticles synthesized by CVS are ultrasonicated in 50 mL of deionized H_2O for 10 min to break the soft agglomerates and then suspended in aqueous solution with addition of about 8 vol. % of methanol (total volume of 550 ml). Methanol is used as a sacrificial agent for the oxidation reaction.

The reactor housing is made of quartz and as an irradiation source a lamp is positioned in the middle surrounded by liquid containing catalyst nanoparticles. Depending on the desired light wavelength two types of lamps can be used: mercury lamp [*Peschl*, Hg immersion lamp TQ, power adjustable from 0 to 700 W, typical power applied: 500 W; $\lambda = 250 - 600$ nm) or a Xe lamp (*Peschl*, Xe immersion lamp

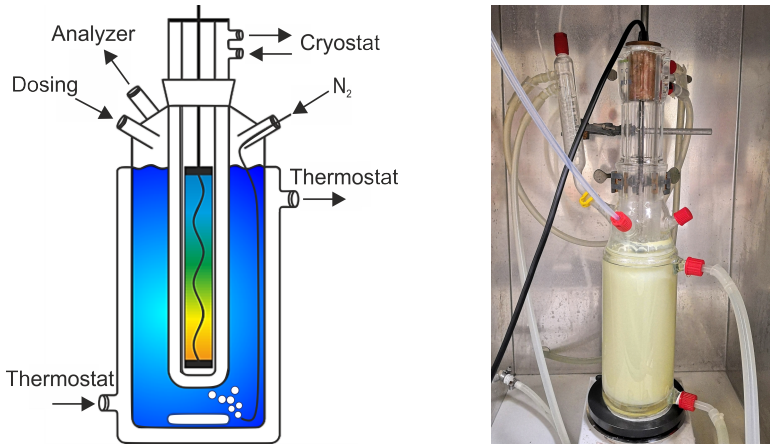

Fig. 3.6: Schematic representation (left) and laboratory setup (right) for the co-catalyst photodeposition / photocatalytic overall water splitting experiments connected with sensors for on-line detection of the H_2, O_2 and CO_2 gases. Photos are printed and used with permission of G.W.Busser

TX, 150 W, λ = 400 – 800 nm). The suspension is stirred using a magnetic stirrer and degassed by flushing 96 sccm of N_2 to remove residual gases. The lamp is switched on immediately to investigate the aqueous methanol reforming activity of the pure CVS nanoparticles. Co-catalyst: 0.1 wt.% Cr_xO_y and 0.1 – 0.6 wt.% Rh are added from metal salt solutions K_2CrO_4 and Na_3RhCl_6, respectively. The methanol solution is filtrated and the filter cake washed with distilled water to remove the metal salts residuals and at the end dried overnight.

The overall water splitting experiments are performed stepwise and the evolved gas mixture is analyzed by a three-channel analyzer. A thermal conduction detector is used to detect H_2, a paramagnetic detector for O_2 and an infrared detector for CO_2. The setup and additional details are presented by Busser et al. [2012].

3.4 Characterization Techniques

3.4.1 X-ray Diffraction (XRD)

The spacing *d* between lattice planes in a crystal structure have the same order of magnitude (1 – 100 Å) as the wavelength of the X-rays and therefore XRD is used to generate diffraction patterns. XRD is a characterization technique used to determine crystal structure, microstructure and phase composition of a material. X-rays are generated by an X-ray tube where electrons are accelerated from a cathode (usually from tungsten) to an anode. Depending on the anode material (copper, silver, molybdenum etc.) X-rays have a characteristic wavelength λ. Accelerated electrons which have enough energy can eject an electron from the inner shell of the anode material leaving a hole. Holes are filled by other electrons from outer shells together with the emission of an X-ray photon. Only 1 % of the total energy can be converted into X-rays. CuK_α radiation with a wavelength λ = 1.540556 Å is produced at 40 kV and 40 mA in X-ray diffractometer (*PANalytical X'Pert PRO*) and K_β radiation is filtered using a Ni-filter. The incident beam irradiates the sample and constructive interference occurs when the Bragg law [Bragg and Bragg 1913] is satisfied:

$$n\lambda = 2d \cdot \sin\theta \tag{3.5}$$

where: n – integer; λ – wavelength of incident photons; θ – the angle between the incident X-ray and the scatter plane and d – spacing between the planes in the crystal structure. X-rays are diffracted as a result of their scattering from lattice points in the crystal structure and detected by linear position sensitive X'Celerator detector.

Powder samples are analyzed on a zero-background holder (Si single crystal that is rotated during measurement) with a step size of 0.0167°, a scan speed of 0.006 °/s and a time per step of 347.35 s. Scanning is performed usually in a range of 10° < 2θ < 120° and repeated 10 times before the averaged scan (diffractogram) is analyzed using Rietveld refinement [Rietveld 1969] with the MAUD software [Lutteroti, 2010]. Information about phase composition, crystal structure (position of the atoms, lattice parameters, occupation numbers etc.), as well as microstructure (crystallite size, anisotropy, microstrain, defect probability etc.) are obtained. The method uses a non-linear least square algorithm to minimize the difference between experimental and calculated diffraction pattern and the residual function is presented as:

$$WSS = \sum_i W_i (I_i^{\exp} - I_i^{calc})^2 \quad ; \quad w_i = \frac{1}{I_i^{\exp}} \tag{3.6}$$

where: w_i – weighting factor equaling $1/I_i^{exp}$, I_i^{exp} – observed intensity at the i^{th} step and I_i^{calc} – calculated intensity at the i^{th} step. The diffractogram is calculated by the classical intensity equation:

$$I_i^{calc} = I_i^{bckg} + s\sum_K L_K \left|F_K\right|^2 \phi(2\theta_i - 2\theta_K) P_K A_K \tag{3.7}$$

where: I_i^{bkg} – the background intensity at the i^{th} step, s – scale factor, K – h,k,l Miller indices of a Bragg reflection, L_K – factor containing Lorentz, polarization and multiplicity factor, F_K – structure factor for the K^{th} Bragg reflection, P_K – preferred orientation function, A_K – absorption factor and ϕ – reflection profile function. A

diffraction pattern of the standard reference NIST LaB_6 material is fitted to determine the instrumental resolution function using identical parameters as for the CVS samples. Instrumental parameters are fixed in MAUD to exclude the instrumental broadening and only parameters for crystal structure and microstructure are fitted. Analyses are carried out in Bragg-Brentano geometry using zero background holder (ZBH) with and without powder to remove the background from the sample signal. The degree of crystallinity Γ is estimated from the ratio of the coherent scattered intensity to total scattered intensity from the diffraction pattern and is given as:

$$\Gamma = \frac{\int I_{coh} d\theta}{\int (I_{coh} + I_{incoh}) \cdot d\theta} \tag{3.8}$$

where: I_{coh} – intensity of the coherent scattering, I_{incoh} – intensity of the incoherent scattering and θ – scattering angle. This degree of crystallinity is a relative measure and it is calculated in the same way for each sample to provide consistent information about the trend as a function of synthesis parameters. A combination of Popa approach [Popa 1998] and the Warren model [Warren 1990] implemented in the MAUD code are applied for size and microstrain anisotropy broadening and planar defect probability, such as intrinsic and twin faults.

3.4.2 X-ray Absorption Spectroscopy (XANES and EXAFS)

The main characteristics of X-ray absorption spectroscopy (XAS) is its element selectivity and the sensitivity to the local structure. Experimental data are collected at synchrotron radiation facilities. XAS measures the absorption coefficient $\mu(E)$ as a function of photon energy E. In transmission mode incoming I_o and transmitted I intensity of the X-rays are recorded [Koningsberger et al. 2000]. According to the Beer-Lambert law these are connected by:

$$I = I_o e^{-\mu(E) \cdot d} \tag{3.9}$$

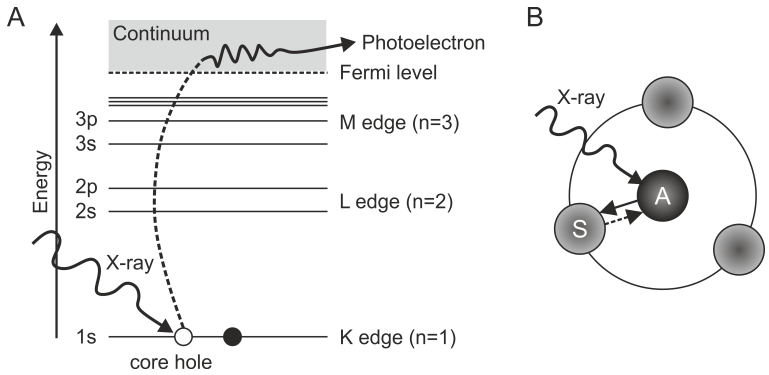

Fig. 3.7: A – Principle of XAS and formation of the photoelectron and **B** – interference between the outgoing and backscattered waves (S – scatterer and A – absorber). Reproduced and adjusted from [Koningsberger et al. 2000]

where d is the sample thickness. $\mu(E)$ is a decreasing function except for sudden jumps, so called absorption edges, which occur at characteristic values of the photon energy. When a photon has sufficient energy the photon excites a core electron from an atom above the Fermi energy and the photoelectron is created (Fig. 3.7A). Quantum numbers n = 1, 2 and 3 describe the shell to which the core electron belongs and edges are labeled as K, L or M.

As can be seen in Figure 3.8 the X-ray absorption spectrum (XAS) can be divided into three regions: pre-edge and X-ray fine absorption (XAFS), which can be further divided on X-ray Absorption Near Edge Structure (XANES) – 50 eV above/around the absorption edge and Extended X-ray Absorption Fine Structure (EXAFS) – over several hundred eV after XANES. XANES is associated with the excitation process of bound and quasi-bound states and sensitive to the oxidation state (valence) and coordination symmetry of the absorbing atom [Iwasawa et al. 2017]. EXAFS refers to the oscillatory behavior of the absorption coefficient above an absorption edge. The photoelectron can be considered as a spherical wave which propagates away from the absorbing atom and eventually interferes with the electrons of neighboring atoms. Part of this wave is backscattered toward the origin and therefore the inter-

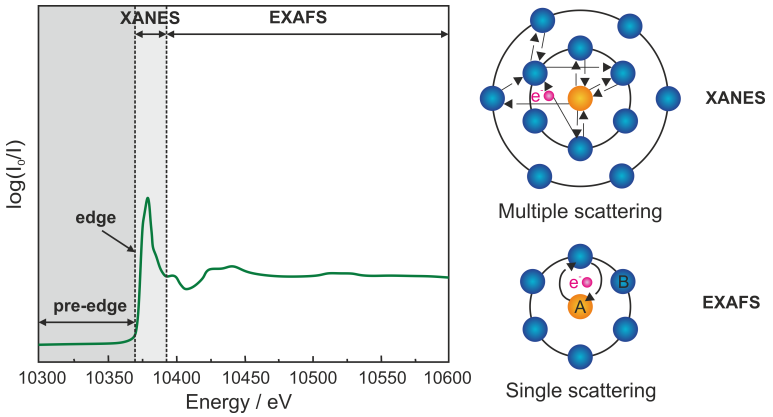

Fig. 3.8: Pre-edge, XANES (multiple scattering) and EXAFS (single scattering) regions in XAS spectrum. Adapted from [Cheng et al. 2013] with use of experimental data recorded for CVS Ga_2O_3 for graphical illustration

ference phenomena between the outgoing wave and backscattered wavelets occurs (Fig. 3.7B). This interference gives rise to modulation of the absorption probability. EXAFS oscillations may approximately be expressed as a sum of the sinusoidal functions of many shells on the basis of the single scattering theory, usually used as a fitting function [Koningsberger et al. 1988]:

$$k^n \chi(k) = S_0^2 \sum_{r_i} \frac{k^n N_{r_i} F_{r_i}(k)}{k r_i^2} \sin(2kr_i + \phi_{r_i}(k)) \exp(-\frac{2r_i}{\lambda_i(k)}) \exp(-2\sigma_{r_i}^2 k^2) \quad (3.10)$$

$$k = \frac{\sqrt{2m_e(E - E_0)}}{\hbar} \quad (3.11)$$

with: k – photoelectron wave vector, S_0^2 – reduction factor by multiple scattering factor, r_i – distance between absorbing and scattering atoms, N – coordination number, F – backscattering amplitude function, ϕ – phase shift function, $\lambda(k)$ – mean free path of the photoelectron and σ – Debye-Waller factor. The wave vector of the photoelectron k is given by equation 3.11 where: m_e – mass of the electron, E – incident beam energy, E_0 – absorption edge energy and $\hbar$ – reduced Plank constant.

The measured intensity is first converted to $\mu(E)$, then normalized to the incident beam intensity I_0 and reduced to $\chi(k)$. Normalized $\mu(E)$ is suitable for XANES analysis, while EXAFS demands the background-subtracted $\chi(k)$.

In order to determine the local structure of the CVS and commercial powders experiments were performed using beamline 12.BM.B with energy range 7.5 – 28 keV at the Advanced Photon Source (APS) in Argonne National Laboratory, Chicago, USA. Samples are prepared by mixing the Ga_2O_3 samples with starch powder (9.37 mg : 73.49 mg) and uniaxial pressed for 5 min at pressure of 30 kN to form a pellet with diameter of 13 mm covered with kapton tape. Transmission and fluorescence spectra are obtained at ambient temperature. The XAFS data is analyzed using the program *xafsX* [Winterer 1997]. The extracted EXAFS data are analyzed by Reverse Monte Carlo (RMC) method using the *rmcxas* program [Winterer 2000]. Number of Ga atoms, lattice constants and crystallite sizes from Rietveld refinement are used to obtain initial atom configurations. The visualization software *VESTA* is used for graphical display of the atomic configurations [Momma and Izumi 2011]. Theoretical amplitude and phase functions for RMC analysis are obtained using *FEFF 9.6.4* simulations [Rehr et al. 2010].

3.4.3 Low-Temperature Nitrogen Adsorption

Low-temperature nitrogen adsorption is a method used for determination of: specific surface area, pore volume and pore size distribution of powders. The principle of the method is based on physisorption. The method is based on the measurement of gas needed to cover the surface of the sample in a molecular monolayer. It is assumed that molecules continue to physisorb in layers indefinitely, which is an extended Langmuir (monolayer) model. The powder sample, typically between 20 mg and 50 mg, is placed in the glass cell (12 mm diameter) and cooled at the temperature of liquid N_2 (-195.15°C). At low relative pressure p/p_o first the micropores are filled when N_2 is adsorbed. When the relative pressure is in range 0.05 – 0.35 this linear region is called a BET (Brunauer-Emmett-Teller). It is used to determine the specific surface area [Lowell 2012] and in BET theory is considered that sample

surface is completely covered with a molecular monolayer of adsorbed N_2 with volume V_m. BET equation is given as:

$$\frac{P}{V(P-P_0)} = \frac{1}{V_m \cdot C} + \frac{C-1}{C \cdot V_m} \cdot \frac{P}{P_0} \tag{3.12}$$

$$S_{sp} = \frac{A_{N_2} \cdot N_A \cdot V_m}{M_{N_2} \cdot m_{sample}} \tag{3.13}$$

where: P – equilibrium experimental pressure, P_0 – vapor pressure of the adsorption gas (N_2) at T_{lN2} = (-195.15°C), V – volume of the gas adsorbed, V_m – volume of the gas adsorbed when the surface is covered by a monolayer of the adsorbate, C – constant related to enthalpy of adsorption, S_{sp} – specific surface area, A_{N2} and M_{N2} – cross section area (16.2 Å^2) and molar mass of N_2 molecules and m_{sample} – mass of the powder used for analysis. It is possible to determine the average particle diameter with the assumption that all the particles are spherical and consist of a single phase. If the density of the powder is known (for β-Ga_2O_3 is 5.88 g/cm^3) using a measured S_{sp} the particle diameter d_{BET} is calculated as:

$$d_{BET} = \frac{6}{S_{sp} \cdot \rho_{powder}} \tag{3.14}$$

The degree of hard agglomeration N_{agg} represents the number of the primary particles in an agglomerate. It can be estimated from the ratio of the average particle volume from BET and the crystallite size from XRD:

$$N_{agg} = \frac{d_{BET}^3}{d_{XRD}^3} \tag{3.15}$$

A Quantachrome Autosorb 1C instrument is used to obtain the data. Prior to analysis the samples are degassed under vacuum at 120°C for at least 24 h to remove the moisture or easy volatile residual organics from the powder.

3.4.4 Ultraviolet-Visible (UV/Vis) Diffuse Reflectance Spectroscopy

UV/Vis diffuse reflectance spectroscopy is a method to determine the band gap and absorption coefficients of powder samples in the visible and UV regime for wavelengths between 800 – 400 nm (λ_{vis}) and 400 – 100 nm (λ_{UV}). Two hemispherical mirrors collect the diffuse reflected light from the horizontally placed solid powder sample and direct it to the detector. Scattering and absorption behavior of the measured sample can be described by the Kubelka-Munk $F(R_\infty)$ [Kubelka and Munk 1931] equation:

$$\frac{K}{S_{km}} = \frac{(1-R_\infty)^2}{2 \cdot R_\infty} = F(R_\infty) \tag{3.16}$$

where: K – absorption coefficient, S_{km} – scattering coefficient and R_∞ – reflection of the sample layer with infinite thickness. The absorption coefficient α is correlated to the band gap energy E_g which is derived from $F(R_\infty)$ by plotting $[F(R_\infty)]^{1/n}$ against photon energy hv known as Tauc-plot [Tauc 1968]. The value of the exponent n can be 2 or ½ for the direct or indirect band gap, respectively, denoting the nature of the transition. For gallium oxide samples a direct band gap transition is observed, while for mixed Zn-Ga oxide variations both direct and indirect band gap is observed for determination of the band gap by Tauc-plot.

DRUV/Vis spectra are measured using a Perkin Elmer Lambda 650 spectrometer equipped with a Harrick Praying Mantis diffuse reflectance accessory. The sample is irradiated by light with a wavelength in the range from 800 nm to 200 nm at a resolution of 1 nm and an integration time of 0.4 s. $BaSO_4$ is used as a 100 % internal reflectance standard, while the samples (25 mg) are diluted in 500 mg of $BaSO_4$ and measured.

3.4.5 Photoluminescence (PL) Spectroscopy

PL spectroscopy is a technique for investigation of optical and electronic properties of semiconductors, as well impurities and defects present in the material. If the incident photons have a larger energy than the band gap energy electrons are excited

from the valence to the conduction band and electron-hole pairs are created. After excitation the electrons return to the ground state. They can re-emit photons or undergo different internal transitions [Aoki 2012]. PL spectra are recorded using a FL3-22 PPD HORIBA-spectrometer with a laser excitation source of a power of 1 mW, slit width of 150 µm and integration times from 0.2 s to 5 s. In general, samples are measured in the range 260 – 802 nm and some samples with broader spectra also up to 866 nm or 916 nm. The measurements were carried out by Johanna Meier (AG Bacher).

3.4.6 Dynamic Light Scattering (DLS) and Zeta-Potential

Dynamic light scattering (DLS) is used to determine the hydrodynamic diameter d_h of colloidal particles. A monochromatic laser beam is passed through a colloidal dispersion, light is scattered from the particles in all directions and detected by an analyzer. Due to the Brownian molecular motion of the particles there are time-dependent fluctuations of the scattered light intensity, which are detected by a photomultiplier and evaluated by a correlator. The Stokes-Einstein equation provides the relationship between the diffusion coefficient D and the hydrodynamic diameter of the particles d_h [Berne and Pecora 2000]:

$$D = \frac{k_B \cdot T}{3\pi \cdot \eta \cdot d_h} \tag{3.17}$$

with: k_B – Boltzmann constant, T – temperature and η – viscosity. Particle size distribution and the hydrodynamic diameter is measured using a Zetasizer Nano ZS (Malvern) with a He-Ne laser with a wavelength of 633 nm. A colloidal dispersion with 1 mg of powder and 10 ml of an appropriate solvent is prepared. An amount of 1 ml is filled into a cuvette and measured at room temperature.

The zeta potential ζ of dispersion is measured as a function of pH to provide information about surface charge of the particles. By applying an electric field, charged particles move towards the electrode with opposite polarity. The diffuse layer can be sheared off, while the so called Stern layer remains strongly bound to

the surface of the particles [Clogston and Patri 2011]. The zeta potential is the potential present at this 'slipping plane' boundary. The electrophoretic mobility μE of the particles is determined from the electrophoretic dynamic light scattering. The zeta potential is an indicator of the dispersion stability and can be calculated using the Henry equation:

$$\xi = \frac{3 \cdot \eta_{zp} \cdot \mu(E)}{2\varepsilon \cdot f(k\alpha)} \tag{3.18}$$

where: η_{zp} – absolute zero-shear viscosity of the medium, ε – dielectric constant, $f(k\alpha)$ – Henry function and $k\alpha$ – measure of the ratio of the particle radius to the Debye length. The colloidal dispersions of nanoparticles with a zeta potential between -10 mV and +10 mV are considered as stable, while those exceeding values of -30 mV and +30 mV are highly anionic and cationic, respectively. Colloidal stability is important for POWS experiments.

3.4.7 Fourier Transform Infrared Spectroscopy (FTIR)

FTIR is an analytical method for identification of organic compounds in the material. Chemical bonds between different elements absorb the infrared light in the fingerprint region with wavelength in region 1500 – 500 cm^{-1} causing oscillations and rotations in molecules. IR radiation is absorbed only if there is a change in the dipole moment within the molecule. The measurements were performed with an FTIR spectrometer IFS66v/S (Bruker) of the solid powders. The scattered radiation is composed of the radiation reflected from the surface and of the absorbed radiation, which is brought back to the surface by internal scattering processes. The signals arriving at the detector are decomposed into a sum of sine functions with different frequencies and amplitudes by the Fourier transformation. Diffuse reflectance infrared Fourier transform (DRIFT) spectroscopy is a convenient sampling technique used on samples without prior preparation. The IR irradiation interacts with the nanoparticles and it is reflected from their surface, causing the light to diffuse or scatter, as it moves throughout the sample. Measurements are carried out by Dr. Günther

Prinz (AG Lorke) to investigate the presence of organic residuals on Ga_2O_3 particle surfaces with variation of the process temperature.

3.4.8 Thermogravimetry (TG) / Differential Thermal Analysis (DTA)

Combined TG/DTA is a thermal analysis technique used to observe the thermal properties of samples. Upon heating of solid powder TG measures mass change during the temperature-time controlled process in a defined atmosphere. The mass change occurs due to moisture evaporation, decomposition or oxidation of the sample. DTA shows changes in the samples, either endothermic or exothermic, relative to an inert reference material, again as a function of the temperature-time profile. The DTA curve provides information on the type of the phase transformation, such as melting or sublimation of the sample. This allows the investigation of the thermal stability and decomposition kinetics of the solid precursors used in this work.

A commercial TGA/DTA (Bähr STA 503) was used to perform the experiments up to maximum temperature of 520°C in a mixture of nitrogen and air. Samples of 12 mg are used along with 58 mg of Al_2O_3 as a reference material. Analysis were carried out by Andreas Görnt (AG Atakan).

3.4.9 Scanning Electron Microscopy (SEM)

SEM is an imaging method that uses a fine beam of focused electrons to probe the surface of a sample. The electron gun emits a current of high energy electrons to the sample. The beam is focused using electromagnetic lenses and interacts with the surface from which is scattered to obtain information. In general, due to the interactions of electrons with the sample surface the backscattered, secondary, Auger, elastically and inelastically scattered electrons are created, as well X-rays and other photons (Fig. 3.9). Backscattered electrons provide information about atomic number differences, while secondary electrons give information about surface topography. On the other hand, energy dispersive spectroscopy (EDS) in SEM uses X-rays generated after excitation of core electrons. The energy of the X-rays is character-

istic for every element in the periodic table. That is why EDS is used for the elemental analysis. Not only the qualitative information of the element type, but also the quantitative one can be obtained. The accuracy of EDS depends on many factors, such as: overlapping of the X-ray emission peaks and their energies, nature of the sample and its thickness etc. [Goldstein 2012]. However, EDS is found to be very useful for providing consistent information about the trend as a function of synthesis/process parameters.

A high vacuum scanning electron microscope (JEOL-JSM-7500F) with cold field emitter for high resolution is used. Besides recording of the secondary electrons with the SEI detector, images were also recorded in transmission mode using the TED detector. The instrument has a magnification range of 25x – 1.000.000x and a maximum resolution of 1.0 nm at an acceleration voltage of 30 kV. For scanning transmission electron mode (STEM) with the TED detector the applied voltage is 30 kV. For EDS the samples are prepared on the carbon tape on the aluminum sample holder, while for STEM 1 mg of the powder is dispersed in 10 ml of methanol (semiconducting grade) and ultrasonicated for 15 min and drop casted on a carbon film on 300 mesh TEM copper grids.

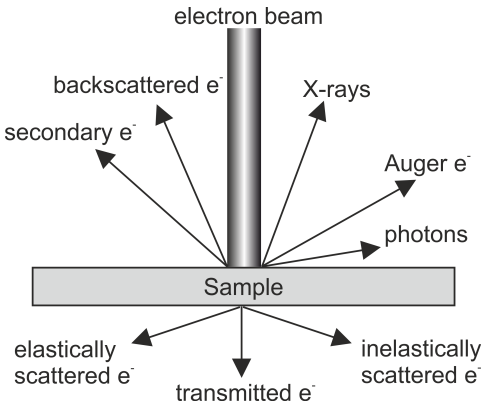

Fig. 3.9: Different electrons-matter interactions when the focused electron beam from the electron gun probes the sample

3.4.10 High Resolution Transmission Electron Microscopy (HRTEM)

HRTEM is an analytical technique used to study very thin specimens in a 2D plane (usually with thickness of few nanometers), which is different compared to SEM where sample surfaces are investigated. It has a much higher resolution than SEM and electrons are transmitted through a specimen (Fig. 3.9) to produce high-resolution images. It can structurally characterize samples at an atomic level making it very useful for characterization of nanoparticles. The working principle is similar to SEM, it has a TEM gun to produce electron current towards a sample in the vacuum, as well the lenses and apertures to control the beam. Electrons penetrate the sample causing partial scattering. After a series of lenses an intermediate image is generated, which is magnified by further objective lenses (more than 50 million times possible). The image can be displayed directly on a fluorescent screen or on the computer screen by using a charge-coupled device of a so called CCD camera. Bright field is displayed when using the unscattered intensity and it switches to dark field when suppressed [Reimer 1989]. Complementary to EDS, which is used in SEM / TEM, Electron Energy Loss Spectroscopy (EELS) can only be realized in a HRTEM system in STEM mode. It enables the investigation of the composition of the samples and their electronic properties. The sample is exposed to a beam with a known narrow range of kinetic energies. Some of the electrons are inelastically. By measuring the energy loss using an electron spectrometer it is possible to obtain information similar to the previously described XAFS technique. However, EELS works the best with relatively low atomic numbers where excitation edges tend to be sharp. In this work EELS technique was used to determine the presence of the impurities in the sample, that could inhibit photocatalytic activity.

(TITAN Themis microscope), a transmission electron microscope, is used in this work and samples are usually prepared identically to the STEM integrated in SEM with prior plasma cleaning to remove organic residuals. For some samples special high quality TEM grids of amorphous Si or Si_3N_4, which sustain temperature even up to 1000°C, are used. For example, grids with thicknesses of 15 – 20 μm can survive the nitridation process where particles are transformed from oxides to nitrides. TEM windows are marked to find the same spot with identical nanoparticles

before and after nitridation, but since the particles are highly charged due to low conduction of the grid itself it was impossible to capture such images. All the measurements are carried out by Dr. Spark (Siyuan) Zhang (Max-Planck Institut für Eissenforschung, Düsseldorf).

4 Results and Discussion

4.1 Optimization of the CVS Process using Gallium Oxide as Model Material

Very high process temperatures are required in CVS to completely decompose the low evaporable solid precursors in the reactor and generate nanoparticles with high degree of crystallinity. Optimization of the CVS process is based on systematic experiments to generate Ga_2O_3 from gallium(III)acetylacetonate. Change of the process parameters, in particular the pressure, causes a change in the yield of Ga_2O_3 nanoparticles. The desired production rate and yield of CVS generated nanoparticles at the end of the synthesis is determined by the amount of the powder required for the photocatalytic overall water splitting experiments (optimally 600 mg). There are several limiting factors, which are presented in this section. First and foremost, the quality of the synthesized powder must meet the qualitative criteria for photocatalysis. Once optimized, CVS is used to develop more complex material structures, starting from the doped oxides (Zn, Mn and Rh doped β-Ga_2O_3) over nitrides (GaN) to the final desired structure of Zn-Ga oxynitride ($Ga_{1-x}Zn_x$)($N_{1-x}O_x$), as described in chapters 4.2 to 4.4.

4.1.1 Volatility and Decomposition of Ga(III)acetylacetonate

Precursor evaporation rate and mass flow are influenced by the temperature in the precursor delivery zone, carrier gas flow and the total system pressure. To ensure an efficient CVS process an appropriate selection of precursor material is necessary. This selection is based on different factors, such as: precursor cost, amount of the precursor used per experiment, yields of synthesized powder, precursor volatility data etc. Alternatives to acetylacetonates, such as chlorides, are avoided because of generation of HCl, which is a corrosive gas and can damage the equipment. Figure 4.1 depicts the simultaneous DTA/TG curves obtained for $Ga(acac)_3$ from ambient temperature up to 517°C in the nitrogen atmosphere. In the first 60 min with heating rate of 2.72 °C/min up to 163°C small changes are observed due to evaporation of

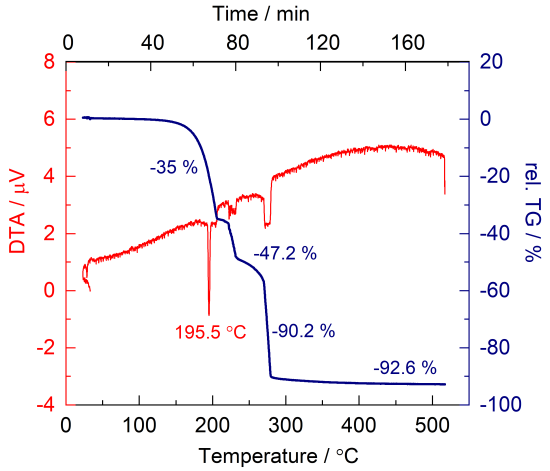

Fig. 4.1: Simultaneous DTA/TG curve of $Ga(acac)_3$ in nitrogen atmosphere

water and other volatile impurities. The endothermic peak at 195.5°C is followed by a sudden decrease of the sample mass by 35 % due to the simultaneous melting, evaporation and decomposition of $Ga(acac)_3$. Two minor endothermic peaks correlate to loss of 47.2 % and 90.2 % in the range 195 – 270 °C and they are interpreted as degradation of intermediates. Al-Khamis et al. [2010] describes in detail the thermal behavior of $Ga(acac)_3$ to form solid Ga_2O_3 through multiple decomposition steps in a temperature range between 150°C and 310°C. The overall chemical reaction is presented as:

$$2GaC_{15}H_{21}O_{6(s)} + 36O_{2(g)} \rightarrow Ga_2O_{3(s)} + 30CO_{2(g)} + 21H_2O_{(g)} \qquad (4.1)$$

The typical amount of precursor used per experiment is 5 g. Assuming that all of the evaporated $Ga(acac)_3$ is converted into Ga_2O_3, the theoretical amount that could be synthesized is 1.28 g, calculated from stoichiometry of the balanced chemical reaction (4.1). The acquired yield varies with change of the process parameters. The amount of powder collected also depends on the thermophoretic particle collector efficiency. Too high temperature in the evaporation zone can easily lead to precursor pyrolysis. The equilibrium vapor pressure of $Ga(acac)_3$ as a function of the temperature in the evaporation zone is presented in Fig. 4.2.

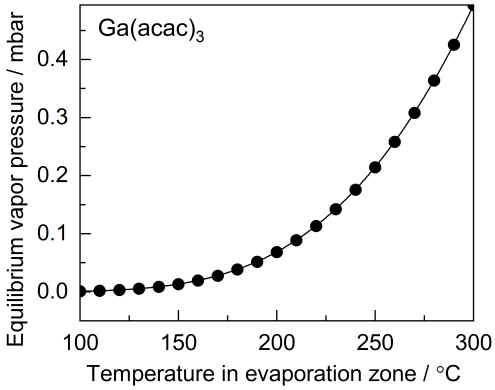

Fig. 4.2: Vapor pressure curve as the function of the temperature for $Ga(acac)_3$

4.1.2 Particle Properties as a Function of the Process Parameters

Parts of this section are published in: Sasa Lukic, Jasper Menze, Philipp Weide, Wilma G. Busser, Martin Muhler and Markus Winterer. Decoupling the Effects of High Crystallinity and Surface Area on the Photocatalytic Overall Water Splitting over β-Ga_2O_3 Nanoparticles by Chemical Vapor Synthesis. ChemSusChem, Volume 10: 4190-4197, 2017. DOI: 10.1002/cssc/201701309.

4.1.2.1 Influence of Pressure in CVS Reactor

Subsequent synthesis of Ga_2O_3 from solid precursor are carried at pressures between 20 – 300 mbar at a constant temperature of 1200°C in this work. The pressure does not only influence the evaporation rate and the precursor partial pressure, but also the residence time. With increase of pressure the residence time is prolonged and particles have more time to grow in the reactor (primary particles coagulate / coalesce). As presented in Fig. 4.3a larger crystallites with lower microstrain (measure of the point defects density) are synthesized at higher pressures. The intensity of the diffraction peaks increases and they become sharper and narrower with more visible characteristic peaks for β-Ga_2O_3 above 100 mbar (Fig. 4.3A). This is accompanied by an increase of the degree of crystallinity (absence of defects) from 10 to 78 % with parallel decrease of surface area from 108 to 62 m^2/g of the synthesized Ga_2O_3

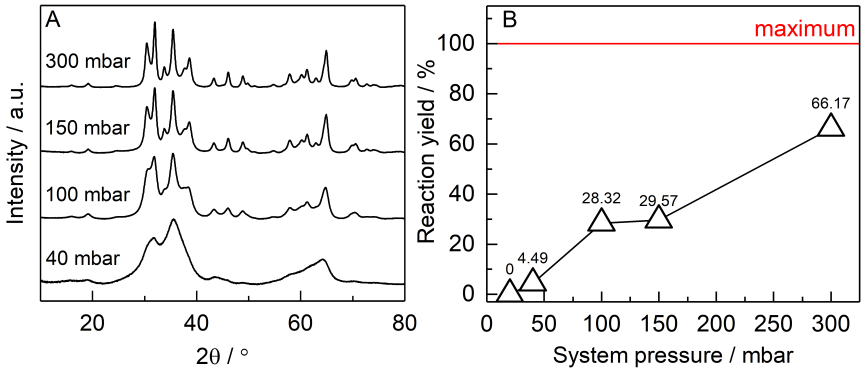

Fig. 4.3: Influence of the pressure variation in CVS system (const. T = 1200°C) on: **A** – X-ray diffractograms of the synthesized Ga_2O_3 nanoparticles and **B** – Reaction yield

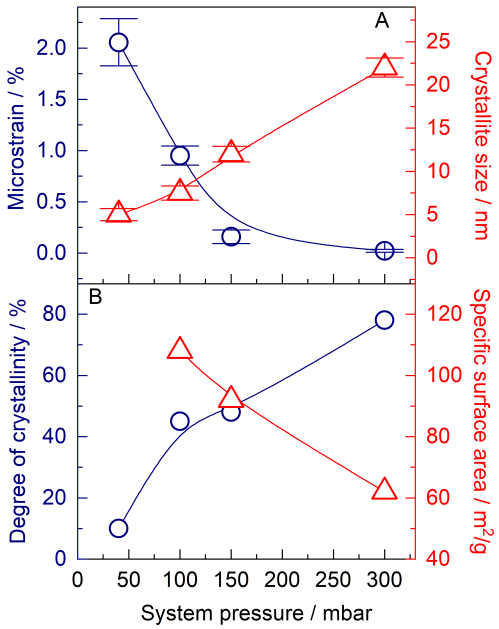

Fig. 4.4: A – Microstrain and crystallite size and **B –** Degree of crystallinity and surface area as a function of the system pressure. (B-splines are intended as a guide to the eye)

(Fig. 4.4). In addition, samples synthesized at low pressures have slightly greyish color indicating probably not complete decomposition of the precursor and the presence of the organic residues in the collected powder. In this work at pressures below 40 mbar the total residence time in the reactor is either too short for a decomposition

of the precursor or primary particles do not collide and coagulate. In high vacuum the mean free path of the Ga_2O_3 monomers increases significantly. If the mean free path is higher than diameter of the reaction tube the frequency of the collisions reduces significantly or no reaction occurs. However, it is also not possible to collect very small particles in the present thermophoretic collector. As a measure of the synthesis and collector efficiency the reaction yield is presented in Fig. 4.3B. It represents amount of the powder collected at the end of the synthesis compared to theoretical maximum amount that could be synthesized. It changes from only 4.5 % at 40 mbar, which is not sufficient for powder characterization (as visible in Fig. 4.4B) to 66 % at 300 mbar. It is obvious, that the system pressure is a major limiting factor and also strongly influences the particle characteristics. In general, solid $Ga(acac)_3$ precursor is less flexible when changing CVS process parameters compared to liquid (TEG for example) and, therefore, it is more challenging to obtain particles with desired properties.

4.1.2.2 Influence of Temperature in CVS Reactor

A second series of experiments is prepared at constant pressure of 300 mbar at temperatures from 1000°C to 1500°C. The time-temperature profile controls the powder characteristics, such as: particle size distribution, degree of crystallinity and degree of hard agglomeration on their way through the reactor. If the temperature is high enough solid-state diffusion is activated and particles may coalesce. After formation of the primary particles or agglomerates new monomers reach their surface and are incorporated into the structure. Further increase of the temperature enhances sintering kinetics, which leads to formation of larger primary particles. This is observed in Fig. 4.6 where crystallites grow from 9 nm to 31 nm with parallel increase of the crystallinity from 31 % to 85 %, while microstrain decreases. The specific surface area is closely correlated to crystal growth and sintering (hard agglomerates are formed) and decreases from 120 m^2/g to 41 m^2/g within the temperature range from 1000 – 1500 °C. An increase of the specific surface has positive impact on the photocatalytic activity of the samples. However, as crystallinity Γ decreases, defect

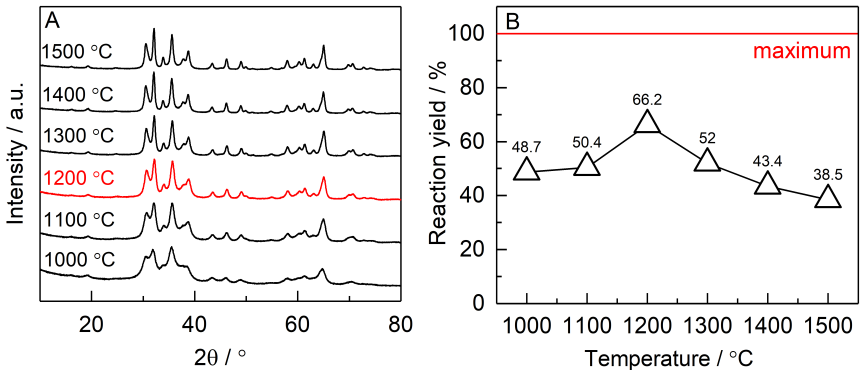

Fig. 4.5: Influence of the temperature variation (const. p=300 mbar) on: **A** – X-ray diffractograms (normalized) of the synthesized Ga_2O_3 and **B** – Reaction yield

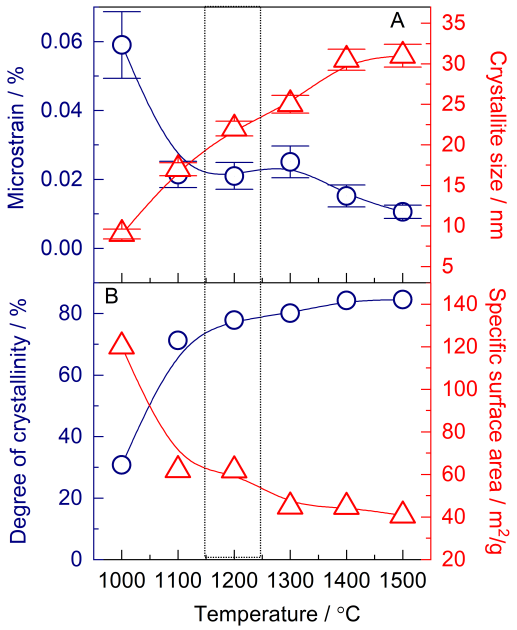

Fig. 4.6: A – Microstrain and crystallite size and **B** – Degree of crystallinity and surface area as a function of temperature in CVS (B-splines are intended as a guide to the eye)

density increases and electron-hole pair recombination becomes more probable. It should be mentioned that the surface is the largest defect of the nanocrystalline particles. Based on the experimental results, the optimum synthesis temperature is found to be for the sample produced at 1200°C (Fig. 4.6), characterized by both a

high degree of crystallinity and a high surface area, as it shows the highest photo-catalytic activity (chapter 4.1.2.3).

Table 4.1. CVS process parameters optimization and particle characteristics

#	*T*	*p*	*MS*	*Γ*	*SSA*	d_{XRD}	d_{BET}	N_{agg}	*LP [a ; b ; c]*
‡	°C	mbar	%	%	m^2/g	nm	nm	-	Å
1	1200	20	*	*	*	< 5	*	*	*
2	1200	40	2.10(2)	10	/	5 (0.7)	/	/	12.426 ; 2.995 ; 5.781
3	1200	100	0.95(9)	45	108	7.5 (0.8)	8.6	1.5	12.276 ; 3.023 ; 5.815
4	1200	150	0.16(7)	48	92	12 (0.9)	10	0.6	12.219 ; 3.018 ; 5.781
5	**1200**	**300**	**0.02(1)**	**78**	**62**	**22 (1.1)**	**15**	**0.3**	**12.258 ; 3.039 ; 5.816**
6	1000	300	0.06(1)	31	120	9 (0.6)	7.8	0.7	12.359 ; 3.041 ; 5.856
7	1100	300	0.02(0)	71	62	17 (0.8)	15	0.7	12.267 ; 3.040 ; 5.826
8	1300	300	0.02(0)	80	45	25 (1.1)	21	0.6	12.285 ; 3.049 ; 5.832
9	1400	300	0.02(0)	84	45	30 (1.3)	21	0.3	12.230 ; 3.040 ; 5.800
10	1500	300	0.01(0)	85	41	31 (1.4)	23	0.4	12.257 ; 3.043 ; 5.818
11	1200	300	0.02(3)	73	62	23 (1.2)	15	0.3	12.255 ; 3.039 ; 5.815
Bulk literature values for β-Ga_2O_3 by Geller [1960]									12.232 ; 3.041 ; 5.801

#	sample number	*SSA*	Specific surface area
‡	units	d_{XRD}	crystallite size from XRD
T	reaction temperature	d_{BET}	particle size calculated from BET
p	total system pressure		
MS	microstrain	N_{agg}	degree of agglomeration
Γ	degree of crystallinity	*	no particles collected

Varying the temperature rather than total system pressure, a better control over the process is established with greater chance to 'tailor' the desired material properties. In addition, the reaction yield change (from 38 % to 66 %) observed in Fig. 4.5B by varying temperature is not as drastic as obtained with pressure variation. All the X-ray diffractograms in this work, as presented in Fig. 4.3A previously and 4.5B here, are normalized to the individual maximum intensity for graphical clarity. Therefore, an overview of the CVS process parameters and detailed particle characteristics data for process optimization is given in Table 4.1.

The degree of agglomeration or number of primary particles per agglomerate *N* is estimated from XRD and BET, as presented in Table 4.1 and it ranges from 0.3 to 1.5. Agglomerates consist of primary particles and agglomeration values should be higher than 1. BET measures the surface of the solid particles assuming that all particles are spherical and dense. We use an equivalent diameter to the diameter of a sphere and the error in the estimation of degree of agglomeration is due to fact

that our particles are not typically spherical, which is shown later in this work. The nitrogen adsorption-desorption isotherm for all tested CVS samples is of type IV with a hysteresis loop H2 according to IUPAC classification. This is common for mesoporous particles with micropores (2 – 50 nm). XRD measures crystallite (domain) size and BET average particle size.

The spectral data in Fig. 4.7 are derived from the Kubelka-Munk function $[F(R\infty)hv]^2$ calculated from the reflectance spectra R vs. hv plot. It reveals small differences between the band gap energies of the Ga_2O_3 samples obtained for temperatures between 1000°C and 1500°C. Direct band gap energies are found to be within a range between 4.85 eV and 4.9 eV, which is in good agreement with values reported for bulk β-Ga_2O_3 by [Li 2012].

Samples are also compared using FTIR (fingerprint region at wavelengths of 4000 – 400 cm^{-1}) to identify the functional groups. No significant difference between samples is observed (Fig. 4.8). The peaks around 3500 cm^{-1}, 2970 cm^{-1} and 1400 cm^{-1} can be assigned to stretching and bending of hydroxyl O-H group and to bending vibration of H-O-H. Nanostructures with high surface areas are easily adsorbing water and hydroxylated groups and Girija [2013] reported increase in their number with increase of pH. The band around 2340 cm^{-1} is due to absorption of atmospheric CO_2. The peak at 1630 cm^{-1} represents C-H group bending and it is probably related to some organic compounds from incompletely decomposed pre-

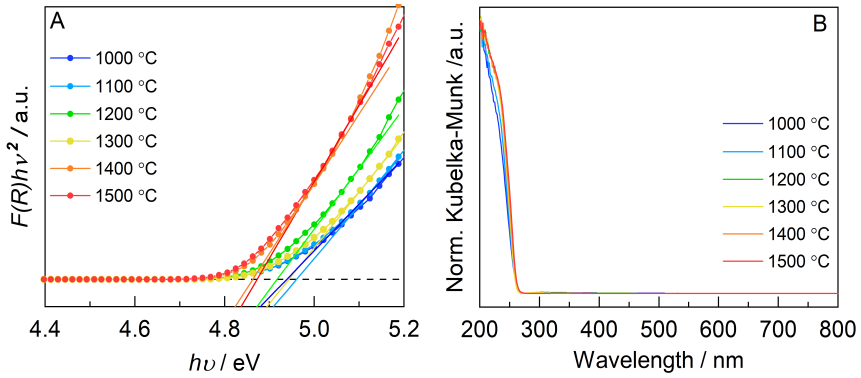

Fig. 4.7: A – Energy of direct band gaps determined by Tauc plots and **B** – Absorbance spectra (Kubelka-Munk function) of samples obtained in range 1000 – 1500 °C

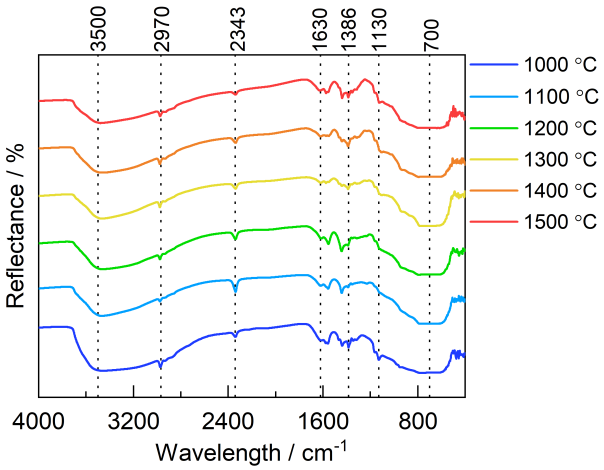

Fig. 4.8: FTIR spectra and identification of functional groups comparing samples 5 – 10 synthesized in the temperature range 1000 – 1500 ºC via CVS

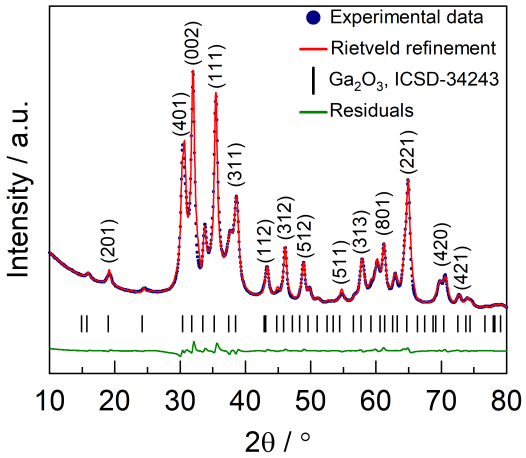

Fig. 4.9 XRD pattern of the Ga_2O_3 sample 5 made by CVS and fitted by Rietveld refinement using MAUD. Compared with Ga_2O_3 (ICSD #34243) as initial studying parameters

cursor, especially for the samples synthesized at lower temperatures. The region around 700 cm^{-1} is linked to Ga-O bending, but it is difficult to explain whether the band arises due to vibration of Ga-O bonds at octahedral GaO_6 or tetrahedral GaO_4 sites. Rietveld refinement showed that all samples consist of pure β-Ga_2O_3 with

monoclinic structure. A typical refinement is shown in Fig. 4.9 and experimental data fits very well with computed data.

4.1.2.3 Aqueous Methanol Reforming and Overall Water Splitting

Measurements of the photocatalytic activity of the CVS samples are performed by P.Weide and G.W.Busser (Ruhr University in Bochum), as part of the project supported by Mercator Research Center Ruhr (MERCUR).

Methanol can be used as sacrificial agent to improve hydrogen evolution reaction (HER) and acts as a good hole scavenger. Holes in the valence band will oxidize methanol to CO_2 instead of oxidizing water to O_2 and the half reaction of H_2 production is favored. The nanoparticles prepared by CVS at different temperatures (1000 – 1500 °C) are suspended in an aqueous solution of methanol and values of their H_2 and CO_2 production rates are compared (Fig. 4.10). The evolved H_2 is a direct relative measure for the number of H_2 evolution sites. CVS samples are modified by stepwise sequential reductive photodeposition of the binary co-catalyst Rh (0.1 wt.%) / Cr_2O_3 (0.09 wt.%) by aqueous methanol reforming (4.2 – 4.5):

$$Rh^{3+} + 3e^- \rightarrow Rh^0 \tag{4.2}$$

$$2CrO_4^{2-} + 10H^+ + 6e^- \rightarrow Cr_2O_3 + 5H_2O \tag{4.3}$$

$$2H^+ + 2e^- \rightarrow H_2 \tag{4.4}$$

$$CH_3OH + H_2O + 6h^+ \rightarrow CO_2 + 6H^+ \tag{4.5}$$

After the 500 W Hg lamp is switched on H_2 evolution is immediately detected. Even without addition of co-catalysts pure Ga_2O_3 nanoparticles possess catalytically active sites for HER. Meanwhile, the observation of CO_2 is temporally delayed due to a higher solubility in water or adsorption of other methanol oxidation products on the surface of Ga_2O_3 nanoparticles. Slow evolution rate of CO_2 is also explained by its formation from methanol, which is first oxidized to intermediates, like formates or carbon-monoxide. CO is further easily oxidized to CO_2. Both intermediates can

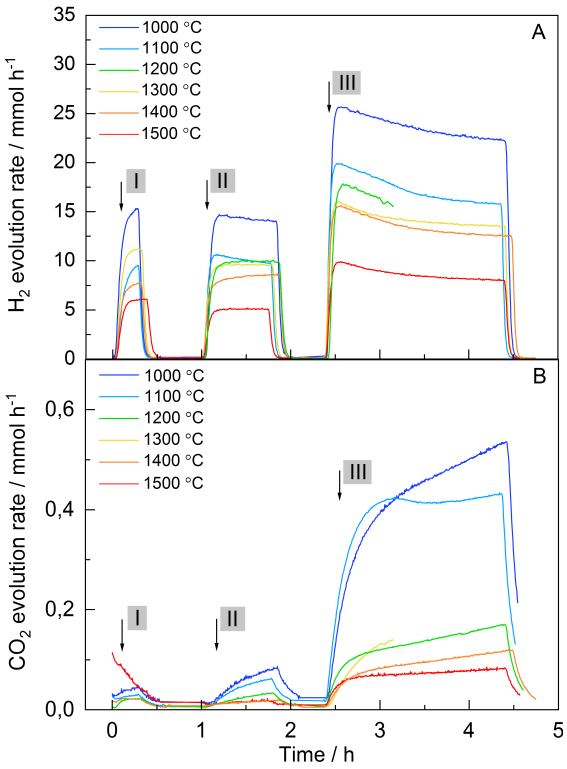

Fig. 4.10: A – H_2 evolution and **B** – CO_2 evolution during reductive photodeposition of the Rh/Cr_2O_3 for samples 5-10 I: light on, no co-catalyst added; II: light on, addition of K_2CrO_4 (0.09 wt.% of Cr_2O_3), 45 min and III: light on, addition of $Na_3RhCl_6 \cdot 3H_2O$ (0.1 wt.% of Rh), 120 min

react with evolved H_2 to generate CH_4 as well, which is an undesired reaction. After addition of Cr_2O_3 methanol reforming activity does not increase in the first step. Interestingly, for the samples synthesized at 1100°C, 1300°C and 1500°C the activity even shows a slight decrease. It is very likely that the deposition of Cr_2O_3 blocks the active sites on the surface of the particles for HER. However, addition of Rh leads to higher methanol reforming activities and the highest value is observed for the sample obtained at 1000°C. As example, in the three photodeposition steps, H_2 evolution rate for pure β-Ga_2O_3 is 15.3 mmol h^{-1}, while after addition of Cr_2O_3 and

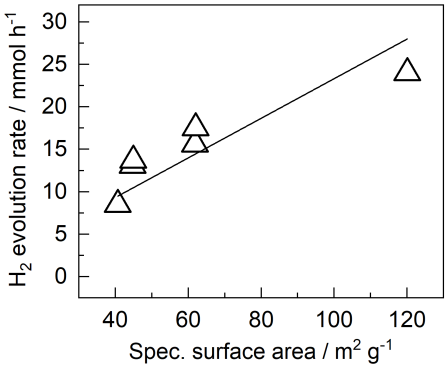

Fig. 4.11: H_2 evolution after co-catalyst addition by aqueous methanol reforming as a function of the specific surface area for samples 5 – 10 (solid line is intended as a guide to the eye)

Rh amounts observed are 14.6 mmol h^{-1} and 25.6 mmol h^{-1}, respectively. This subsequent gradual decrease as a function of time on stream by methanol reforming activity corroborate the previous results by [Busser et al. 2012 and 2015]. Methanol reforming activity decreases for samples obtained at higher temperatures in CVS. This is correlated to the specific surface area (see Fig. 4.11), which may affect the number of HER sites or increase the adsorption capacity of methanol. It supports previous research in this area by [Grewe and Tüysüz 2015] which highlights the increase of the methanol reforming activity with increasing of the specific surface area.

After methanol reforming experiments the $Rh/Cr_2O_3/Ga_2O_3$ powders are washed, filtrated and freeze-dried to remove methanol to be able to perform overall water splitting (OWS) measurements. As anticipated, methanol cannot be completely removed and adsorbed methanol residuals cause significant detection of CO_2 in µmol h^{-1} for all catalysts (in the first 60 min), as visible in Fig. 4.12. However, plotting it together with POWS results measured in mmol h^{-1} methanol evolution values are of minor contribution. From the data in Fig. 4.13 it is apparent that sample 5 (synthesized at 1200°C and 300 mbar) exhibit the highest photocatalytic activity for overall water splitting. Initial evolution rates are 4.9 mmol h^{-1} and 2.10 mmol h^{-1}, while after 5 h it decreases to 2.06 mmol h^{-1} and 0.86 mmol h^{-1} for H_2 and O_2, respectively.

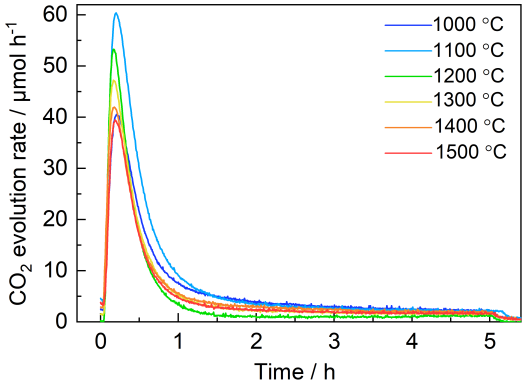

Fig. 4.12: Initial increase of CO_2 evolution rate due to methanol residuals by POWS for CVS samples obtained at different temperatures on the µmol scale (1000 – 1500 °C)

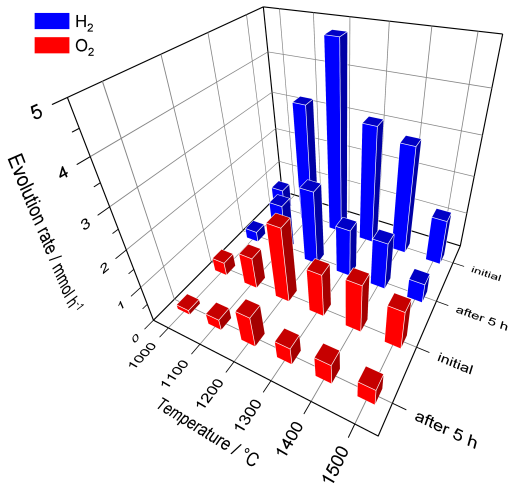

Fig. 4.13: H_2 and O_2 evolution as a function of the time on stream (initial values and after 5 h) for CVS Ga_2O_3 samples obtained at different temperatures (1000 – 1500 °C). To estimate photocatalytic activities per 1 gram of catalyst the results should be multiplied by factor of 6.7 (150 mg of powder is used for POWS) – given in Chapter 8

It is obvious that stoichiometric ratio of H_2:O_2 production rate is slightly higher and differs from expected 2:1. As already mentioned, possible reason is the incomplete removal of methanol, which inhibits the production of O_2. Another important finding is a decrease of the O_2 evolution in the first 2 h, which could be caused by

photocorrosion of the catalyst. There are, however, other possible explanations. Co-catalyst particles may be weakly attached to the surface of the Ga_2O_3 particles and may be easily washed away, especially during stirring of the dispersion. Stationary evolution is achieved between 2 and 5 h and no further decrease in the activity is detected. Comparing POWS results with those from methanol reforming it is noticed that the main requirement for high methanol reforming activity is high specific surface area. On the other hand, for POWS both the degree of crystallinity and a high specific surface area determine the photocatalytic activity. Sample 5 obtained at 1200°C and 300 mbar by CVS has a high degree of crystallinity at a sufficiently high specific surface area. Maeda and Domen [2016] claimed that photocatalytic activity of conventional metal oxide photocatalysts for overall water splitting is known to depend strongly on the crystallinity and particle size of the material, as determined by the preparation conditions. These properties allow efficient charge carrier separation, which results in a high number of HER and OER active sites, which is also supported by [Kudo et al. 2009] and [Hisatomi et al. 2015].

4.1.2.4 Possibility of the Sample Reproduction

This section of the study sought to determine the reproducibility of the sample 5 with the prior highest photocatalytic activity among the CVS samples, as changes in the CVS process parameters can cause significant structural change of the sample. The results given previously in Table 1 indicate that samples 5 and 11, synthesized at the same conditions of 1200ºC and 300 mbar, have almost identical particle characteristics with the same composition and electronic structure. Crystallite sizes are 22 nm and 23 nm, as well they have the same specific surface area of 62 m^2/g, but a small change is observed in decrease of the degree of crystallinity from 78 % to 73 %. As shown in Fig. 4.14 with addition of 0.1 wt.% Cr_2O_3 and 0.1 wt.% Rh co-catalyst the photocatalytic activity of the sample 11 decreases to 1.042 mmol h^{-1} for H_2 and 0.462 mmol h^{-1} for O_2 after 5 h compared to sample 5 (2.06 mmol h^{-1} and 0.86 mmol h^{-1}). From the point of view of the structural characterization both samples show good reproducibility. The lower activity could be attributed to some

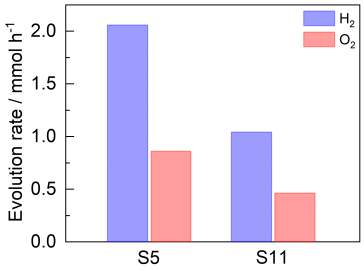

Fig. 4.14: Comparison of POWS activity of the CVS samples 5 and 11 synthesized at exactly the same conditions with addition of 0.1 wt.% of Rh and Cr_2O_3 after 5 h

change during water splitting or the interaction Ga_2O_3-Rh/Cr_2O_3 differs and demands further investigation. Electron energy loss spectroscopy (EELS) is performed and found that O K- and Ga L-edges of both samples are identical within the experimental error. EDS/SEM analysis has shown a small presence of copper or as EDS software indicates a message 'Copper fluorescence through gallium'. Presence of copper could arise during synthesis or even from the precursor using different batches (not specified by chemical purity of precursor composition or either obtained after EDS analysis). Its origin remains unclear even with prior help of the technical support from *BRUKER* suggesting it is probably a software error. However, as observed in Fig. 4.15 the Cu L-edge is below the detection limit and Cu is not identified in any of the samples analyzed by EELS. Carbon on the surface of the particles can inhibit the photocatalytic activity by blocking the active sites.

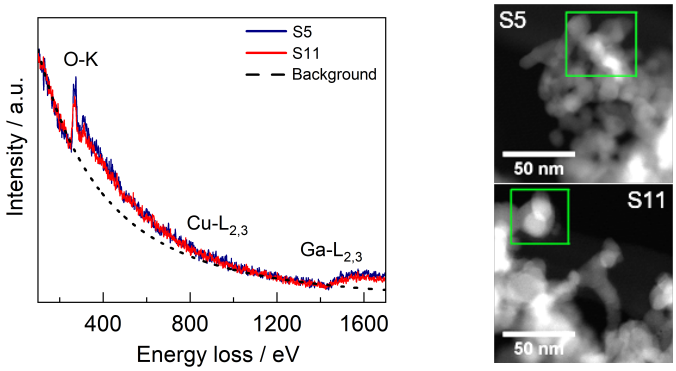

Fig. 4.15: EELS analysis of the samples 5 and 11 synthesized by CVS at exactly the same conditions (1200°C and 300 mbar) showing no difference

4.1.3 Comparison of CVS and Commercial β-Ga_2O_3 Powders

A considerable amount of literature has been published on Ga_2O_3. A systematic literature review on conducted studies is provided by Chen et al. [2017]. Most of the data presented are related to microscaled (commercially available) powders. Commercial Ga_2O_3 (Chempur) powder and Ga_2O_3 synthesized by CVS at 1200°C and 300 mbar (sample 5) are compared. In Fig. 4.16 it can be seen that in the initial state the commercial powder exhibits higher HER and OER activities than CVS sample, while the activity decreases within the time. On the other hand, the activity of the CVS sample increases significantly during the first 3 h and then becomes constant demonstrating a better stability for long time irradiation under UV light.

As a measure of the surface charge the zeta potential is measured as a function of pH. In this work, overall water splitting experiments are carried out in three-phase reactor, where Ga_2O_3 samples are dispersed in the water. Most metal oxides are amphoteric in aqueous media, while the zeta potential is positive in the acidic region and negative in the alkaline region. The isoelectric point (IEP) for the CVS sample is at pH of 7.5 (Fig. 4.17) and consistent with results reported by [Kosmulski 2009]. In the pH range 2 – 4.5 the zeta potential values are around +40 mV and the particle surface is positively charged, while at high pH values 9 – 12 negatively charged. The IEP of commercial Ga_2O_3 is found to be at pH of 3.2 and surface charging of the Ga_2O_3 dispersion is mostly negative in a wide range of pH with zeta

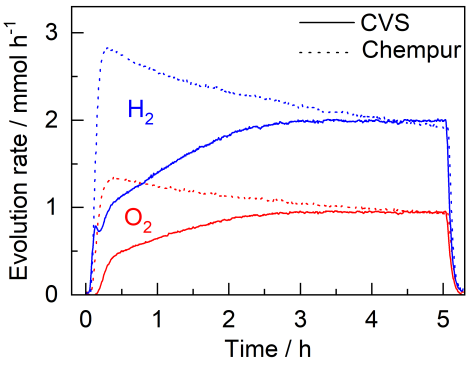

Fig. 4.16: Comparison of POWS activity for sample 5 made by CVS and Chempur commercial powder as a function of time

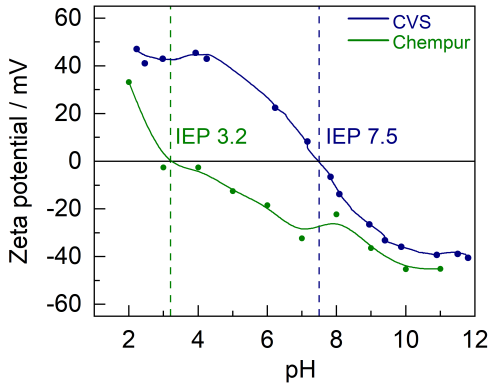

Fig. 4.17: Zeta potential as a function of pH for Ga_2O_3 made by CVS (blue) and commercial Chempur (green). Error bars are smaller than the points

potential values to -40 mV. At the isoelectric point dispersions are typically the least stable, particles agglomerate and sediment. Poor electrostatic stabilization is expected for CVS samples due to their dispersion in water (pH typically around 7) during POWS experiments rather than for the commercial powder. This is prevented by stirring of the dispersion during POWS experiments.

HRTEM images in Fig. 4.18 show remarkable differences between CVS and commercial samples in the morphology. Nanoparticles made by CVS have more or less equiaxed shape and the commercial powder consists of particles with rod like structure with about six times smaller specific surface area.

DLS measurements show two different hydrodynamic diameters (Fig. 4.19). The average hydrodynamic diameter of the commercial Ga_2O_3 rod-like particles is about 4.7 µm. As can be seen on TEM micrographs single rods are around 5 µm in length and whether they agglomerate or simply rotate during diffusion their hydrodynamic diameter doesn't differ too much. The hydrodynamic diameter is much higher for the commercial sample than for the CVS nanoparticles (average size of 70 nm for samples 5 – 10). However, nanoparticles usually agglomerate easier due to the Van der Waals forces. Single particle size of the CVS powders (see Table 4.1) are 3 to 4 times smaller compared to the average hydrodynamic diameter, which indicates their tendency to agglomerate and sediment in aqueous dispersion, evident by the IEP.

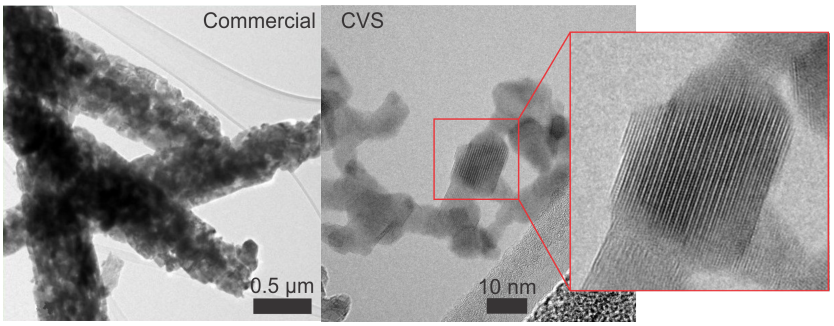

Fig. 4.18: TEM micrographs of commercial Ga_2O_3 nanorods (microsized) and granular CVS Ga_2O_3 particles (nanosized) with high crystallinity

In heterogeneous catalysis the surface to volume ratio is important. Nanoparticles possess a large fraction of the surface atoms per unit volume, which depends on the particle diameter. In Fig. 4.20 the particle is modeled as a cube. When the volume of the cube is broken into smaller cubes the specific surface area increases, as well the total surface energy. Surface atoms, with fewer surrounding neighboring atoms, are under-coordinated and have a higher energy compared to atoms in the bulk due to free dangling bonds. For POWS catalytically reactive atoms are located at the surface of the particle.

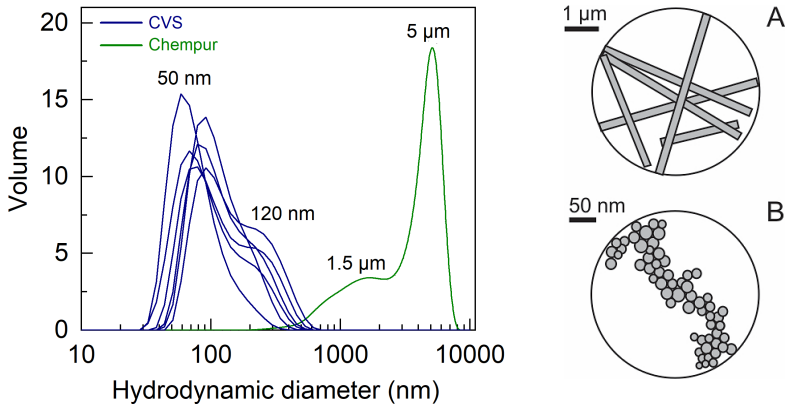

Fig. 4.19: Hydrodynamic diameter measured by DLS of agglomerated: **A** – rod-like particles and **B** – CVS nanoparticles when dispersed in the water

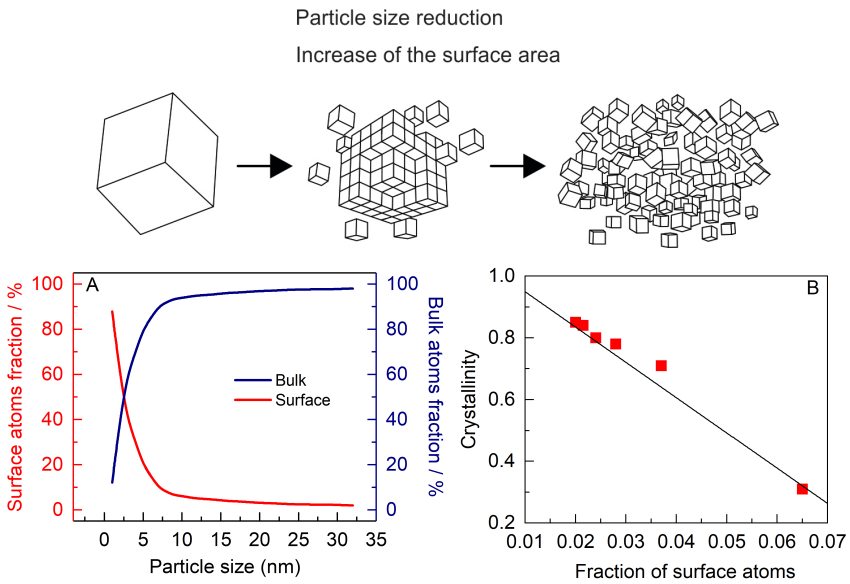

Fig. 4.20: A – Surface and bulk atoms fraction as a function of the particle size and **B** – decrease of the surface atoms fraction of the CVS samples with increase of the crystallinity

For CVS samples a crystallinity increases from 0.31 to 0.85 and it is linearly correlated to the fraction of surface atoms calculated from the primary particle size (Fig. 4.20B). Therefore, very small particles may not always be favorable (i.e. < 3 nm), because the surface itself represents the largest and dominant defect. In addition, due to quantum size effect electrons are confined and VBM and CBM are shifted resulting in a larger band gap [Fendler 2008]. Sample 5 (at 1200ºC and 300 mbar) with the highest POWS production rate and crystallite size of 22 nm has 2.7 % of total number of atoms located on the surface, while for the commercial rod-like particles this number is significantly smaller.

4.1.3.1 Investigation of the Local Structure (XANES / EXAFS)

XRD provides only information averaged over the entire volume of the sample about the periodic, long-range order part of the structure. Local structure is measured by element selective X-ray spectroscopy (XAS). It provides information about

oxidation state and coordination environment of metal atoms to investigate differences between commercial and CVS Ga_2O_3. Here, XAS is used to investigate both samples before and after the POWS experiments, without addition of co-catalysts. XAS deals with measurements of the absorption coefficient μ as the function of the photon energy. Measurements, as well as the data analysis in this work was performed by Markus Winterer. In Fig. 4.21, the XANES spectra reveal two peaks at 10375 eV and 10379 eV contributed to tetrahedral Ga(1) and octahedral Ga(2), as previously described by Nishi et al. [1998]. Slightly higher intensities are observed for CVS Ga_2O_3 sample compared to commercial. Between 10370 eV and 10385 eV, the difference in spectra of the samples before and after POWS becomes more pronounced (Fig. 4.22). A possible explanation is due to different particle morphology and surface charging. CVS nanoparticles are small with higher fraction of the surface atoms (higher surface energies) and also more hydroxylated (contain -OH groups) when dispersed in the water. Still, this differences are very small.

Results of FEFF simulations of XANES spectra, which uses ab initio multiple scattering calculations, are displayed in Fig. 4.23. Functions of Ga(1) and Ga(2) in tetrahedral and octahedral positions in monoclinic β-Ga_2O_3 (light and dark green line, respectively) are shifted and differ in their maximal intensities. Red line shows

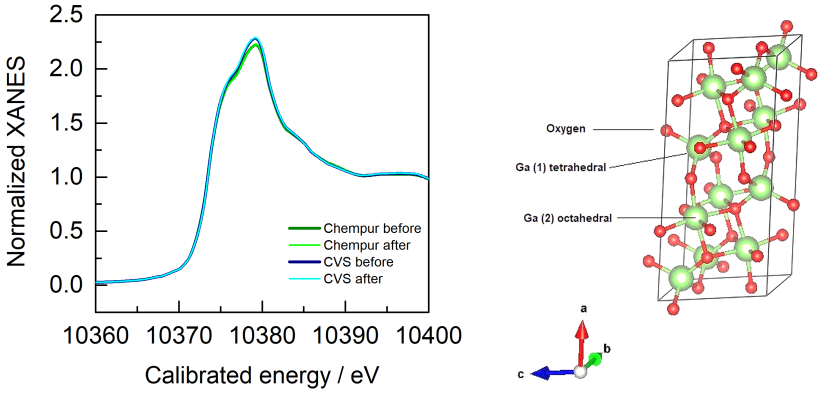

Fig. 4.21: Overview of XANES spectra of the CVS and commercial Ga_2O_3 with characteristic peaks for Ga K-Edge before and after POWS without co-catalysts (left) and unit cell of the monoclinic β-Ga_2O_3 presented using visualization software VESTA (right)

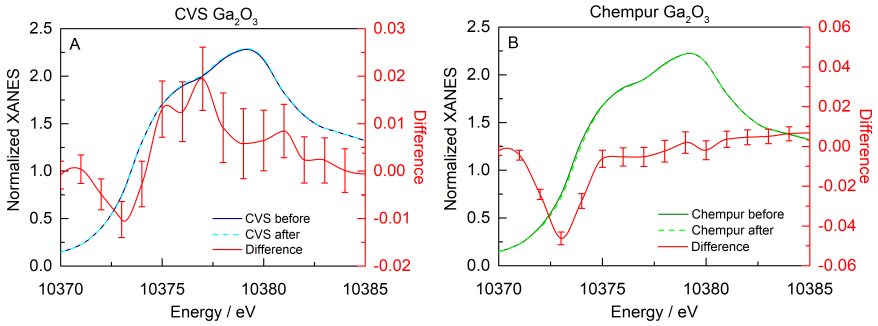

Fig. 4.22: XANES spectra in the energy range 10370 eV to 10385 eV indicating very small differences before and after POWS for **A** – CVS and **B** – commercial Ga_2O_3

the XANES spectra of monoclinic β-Ga_2O_3 and a ratio of 1:1 for Ga(1):Ga(2) in β-Ga_2O_3, as previously reported by Akatsuka [2016] and confirmed by Rietveld refinement of X-ray diffractogram in this work, as displayed in Fig. 4.23. Blue lines indicate $Ga(OH)_3$ and GaOOH in XANES spectra, which might be present at the surface of the particles, as supported by FTIR results.

EXAFS refers to the oscillatory behavior of the absorption coefficient above the X-ray absorption edge. Frequency of this isolated signal is directly proportional to the bond distances between the absorber atom and its neighbors. No significant difference in the local structure between CVS and commercial Ga_2O_3 before and after POWS is observed in the Fourier transformation of the EXAFS data (Fig. 4.24).

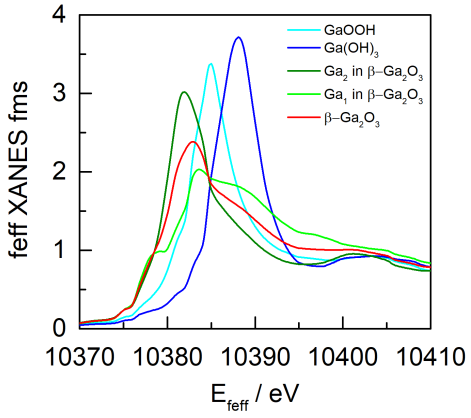

Fig. 4.23: Theoretical XANES obtained by FEFF simulations

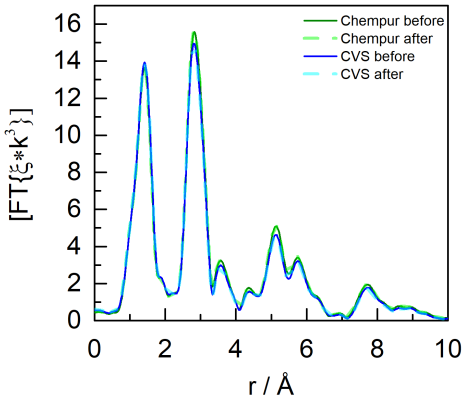

Fig. 4.24: Overview of the EXAFS data of the CVS (sample 5) and commercial Chempur Ga_2O_3 before and after POWS

For RMC analysis the theoretical phase and amplitude functions are obtained by FEFF. RMCXAS code reduces the 3D arrangement of atoms in a model to a pPDF, which is then optimized by varying bond distances in generated atomic configurations to best reproduce the measured EXAFS data. From computation of the complete unfiltered EXAFS signal from the partial radial distribution function in *k*-space atomic configuration of Ga_2O_3 can be generated using RMCXAS software (Fig. 4.25), as well as the Fourier transformed data in *r*-space. Atoms are moved away

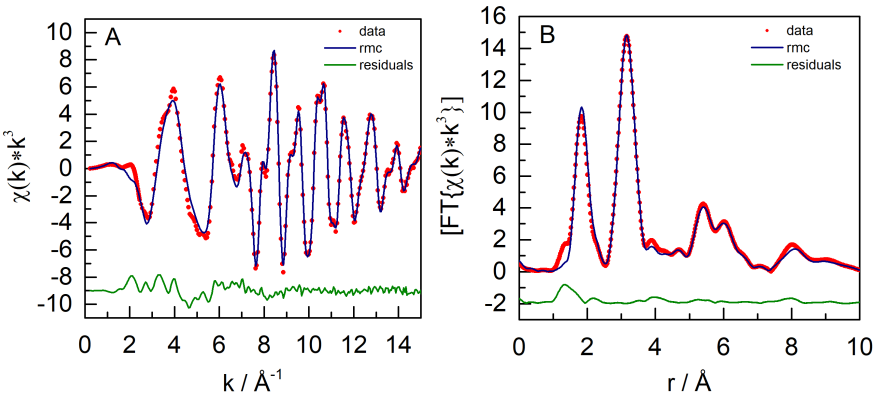

Fig. 4.25: RMC analysis of the Ga K-edge spectra of the **A** – d_{xrd} = 25 nm Ga_2O_3 nanoparticles (sample 5) using perfect, infinite monoclinic crystal and **B** – phase corrected Fourier transformation of the spectra in *r*-space

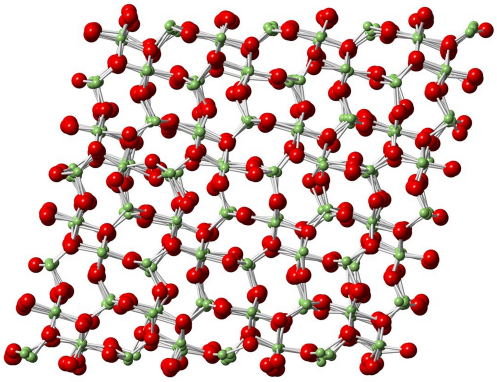

Fig. 4.26: Ga_2O_3 model with monoclinic structure after RMC optimization. Oxygen atoms are shown in red and gallium atoms in green.

from their initial, crystallographic positions until RMC data fits the experimental EXAFS data to obtain actual atomic configuration in the nanocrystals (Fig. 4.26).

Partial pair distribution functions (pPDF) provide information of Ga-Ga and Ga-O bond distances, coordination number and mean squared displacement (Fig. 4.27). pPDF shows no significant difference before and after POWS experiments. CVS Ga_2O_3 nanoparticles do not undergo local structural changes and stay unchanged during POWS experiments.

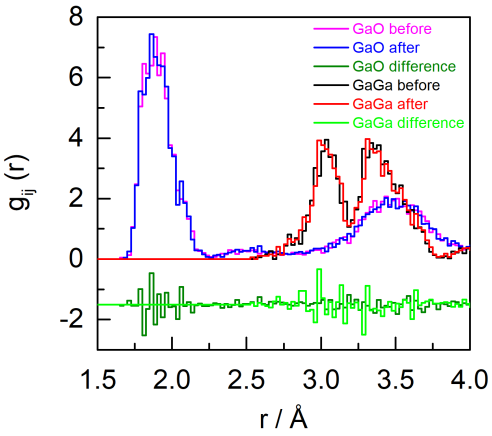

Fig. 4.27: pPDF obtained from the RMC analysis reveals Ga-Ga and Ga-O bonds of Ga_2O_3 before and after POWS experiments

4.2 Structure and Properties of Doped Gallium Oxide

Undoped β-Ga_2O_3 is a wide band gap semiconductor with an absorption edge of 253 nm (4.9 eV) and, therefore, active only when irradiated with UV light, $\lambda < 300$ nm [Yanagida et al. 2004, Sakata et al. 2008, Yuliati et al. 2008, Shimura et al. 2010]. Applying an external voltage will help to reach enough potential energy for electron-hole transfer to make wide band gap semiconductors active under visible light in the photoelectrochemical systems [Arai et al. 2016 and Zhou et al. 2017]. However, working with simple photocatalysts for POWS demands a different approach. The absorption edge shifts to $\lambda > 300$ nm when β-Ga_2O_3 is doped with appropriate dopants, while band gap decreases theoretically promoting photocatalytic activity. Karakitsou et al. [1993], Ishihara [1999] and Kato [2003] proposed that n-type metal oxides when doped with metal ions of low oxidation number the oxygen vacancies introduced into the crystal lattice change n-type semiconductor to p-type. Li et al. [2012], Zhang et al. [2012] and Tang et al. [2016] reported that the addition of divalent cations like Zn^{2+} does not change the basic electronic structure of Ga_2O_3, but generates an empty energy level above the maximum of the valence band, which is enough to form p-type semiconductors. Sakata et al. [2008] and [2011] reported on the improvement of photocatalytic activity by a factor more than 10 by improving migration of photoexcited electrons in the conduction band when adding Zn^{2+}. Hou et al. [2007] investigated the incorporation of trivalent Rh^{3+} cations in β-Ga_2O_3, which causes shift of the absorption edge to 370 nm (3.4 eV). Undoped β-Ga_2O_3 exhibits a valence band formed by the O 2p orbitals and conduction band of empty 4s and 4p orbitals of Ga. Kikkawa et al. [2018] found that trivalent Rh species substitute not tetrahedral, but octahedral Ga sites in the crystal structure. The radius of tetrahedral Ga cation with 4 oxygen coordination environment is 0.47 Å and octahedral Ga cation of 6 oxygen coordination environment is 0.62 Å [Geller 1960], while Rh^{3+} ionic radius is 0.67 Å [Shannon et al. 1976]. Rh d orbitals are located in the conduction band. Sun et al. [2019] doped Ga_2O_3 with Mn^{2+} ions (0.7 Å). Due to coupling of Mn 3d with O 2p orbitals the impurity states in the forbidden zone E_g

decrease the band gap energy to 4.14 eV. The doped impurity causes that neighboring Ga atom leaves the lattice site generating vacancies, which represent an acceptor level in the band gap, while oxygen vacancies behave as deep donor levels [Sun et al. 2019].

Depending on the type of the dopant and its ionic radius when incorporated into the crystal structure of β-Ga_2O_3, Bragg reflections in a X-ray diffractogram may be shifted, as well their intensities changed. If the ionic radius of the dopant is larger than Ga^{3+} ion, as described here, the lattice parameters *a*, *b* and *c* will expand causing an increase in the volume of the unit cell followed by increase of the interplanar distance *d*. Based on Bragg's law the position of the diffracted intensities (peaks) will thus be shifted to smaller values. The electronic density of the dopant is different from Ga, which causes a change in the peak intensity. The degree of these changes, as well the phase purity depends on the concentration of the dopant. For example, the formation of $Fe_x^{3+}O_y$ clusters when Ga_2O_3 is doped with 5% of Fe inhibits the photocatalytic activity, as reported by Toloman et al. [2015].

Excess amount of Rh remains on the surface of the Ga_2O_3 particles and act as co-catalyst, as used in this work, which could enhance the activity [Nishi et al. 1998]. Sufficient Zn on the surface of the Ga_2O_3 particles diffuses into the structure forming spinel zinc-gallate $ZnGa_2O_4$ with band gap around 5 eV at unfavorable band edge positions resulting in low activity [Shimura et al. 2012]. In this case, doping of the Ga_2O_3 samples with Zn is carried out by homogenous precipitation (HP) method.

In this work β-Ga_2O_3 is doped during synthesis in the gas phase with Mn, Rh, Fe and Zn dopants with the goal to directly and uniformly implement dopant ions in the crystal structure. The synthesis is performed at the same conditions as for sample 5 (pure undoped β-Ga_2O_3 nanoparticles). Results of POWS activities, expressed in mmol h^{-1} per gram of catalyst, are compared.

4.2.1 Mn-doped β-Ga_2O_3

β-Ga_2O_3 is synthesized and doped with Mn using $Mn(acac)_2$ precursor with different Mn concentrations between 0.26 % and 7.30 % (as observed from EDS of the final powder comparing atomic concentrations of Ga and Mn).

Fig. 4.28A shows the X-ray diffraction (XRD) patterns of the CVS prepared $(Mn_xGa_{2-x})O_3$ semiconducting nanoparticles. The diffraction intensities derived from monoclinic β-Ga_2O_3 are still observed in the diffractograms of Mn-doped β-Ga_2O_3 (space group C2/m). For further detailed analysis, Bragg positions between $2\Theta = 34.5° - 36.5°$ are shown in Fig. 4.28B for (111) plane of β-Ga_2O_3. It is assumed that Mn has an oxidation number of 2 with characteristic pink pale color, which is the most stable oxidation state, just as CVS synthesized Mn doped Ga_2O_3 powders. The peak shift to the lower angle is due to the lattice expansion caused by substitution of Ga^{3+} with Mn^{2+} and their different ion radius, especially at higher concentrations (see Table 4.2). According to [Hayashi et al. 2012] and first-principles calculations Mn ions prefer the tetrahedral sites, while cation vacancies prefer octahedral sites and these preferences are energetically favorable. Clearly, higher dopant concentration causes a higher number of gallium vacancies (defects) and indicates a degradation of crystallinity for Ga_2O_3 nanoparticles. The overall intensity of the XRD peaks decreases with increase of dopant concentration, which is also found by Popa et al. [2015] for Cr-doped Ga_2O_3. Correspondingly, the crystallite size changes from 22 nm for undoped β-Ga_2O_3 to 17 nm for β-Ga_2O_3 doped with 7.3 % of Mn. Oxygen vacancies induce deep donor levels, while gallium vacancies induce acceptor levels in the band gap. This impurity states decrease the energy of the band gap and the absorbance spectra as a function of wavelength for doped samples differ slightly (Fig. 4.28C). With increasing Mn concentration the band gap is shifted from 270 nm to 290 nm. In Fig 4.28D the band gap energy, derived from Tauc plots, is typically 4.9 eV for undoped pure β-Ga_2O_3 phase and changes from 4.82 eV to 4.75 eV with higher dopant concentration. Although a small decrease of the band gap energy is observed with increasing Mn concentration the expected energy of 4.14 eV, as previously reported, is not reached.

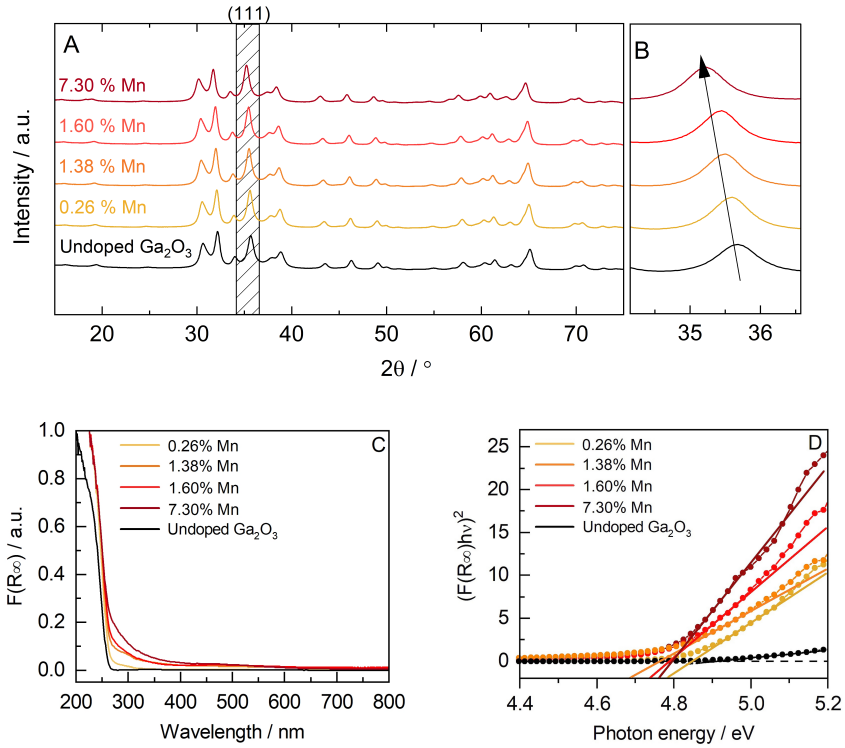

Fig. 4.28: A – X-ray diffraction patterns of the synthesized Mn doped β-Ga_2O_3 in the gas phase, **B** – Diffraction intensities between 34.5 – 36.5° showing a shift to lower angles with increasing amount of Mn (direction shown by arrow), **C** – Reflectance spectra of Mn doped β-Ga_2O_3 samples and **D** – Band gap energy of the samples determined by Tauc plots. The color of the samples changes from pure white to pink with increasing Mn concentration)

Table 4.2. Microstructural data of the Mn-doped β-Ga_2O_3

$C_{[Mn^{2+}]}$ (%)	Color	d_{XRD} (nm)	Cell parameters				*MS* (%)	*Cell vol.* (Å^3)
			a (Å)	*b* (Å)	*c* (Å)	*β*(°)		
0		22 (1.1)	12.258	3.039	5.816	103.7	0.02(1)	210.5
0.26		20 (0.7)	12.279	3.046	5.832	103.7	0.02(3)	211.9
1.38		19 (1.2)	12.293	3.049	5.840	103.8	0.02(5)	212.6
1.60		19 (0.7)	12.295	3.048	5.843	103.8	0.02(4)	212.6
7.30		17 (0.8)	12.303	3.050	5.851	103.7	0.03(3)	213.3
Bulk literature values for β-Ga_2O_3 by Geller [1960]			*a* = 12.232 ; *b* = 3.041 ; *c* = 5.801					

$C_{[Mn^{2+}]}$	dopant concentration	*MS*	microstrain
d_{xrd}	crystallite size	*Cell vol.*	cell volume = $a \cdot b \cdot c \cdot \sin\beta$

The POWS results obtained for Mn doped Ga_2O_3 samples are summarized in Fig. 4.29. The H_2/O_2 production rates are presented as a function of Rh co-catalyst concentration from 0 to 0.3 wt.%, while the concentration of the Cr_2O_3 is constant at 0.1 wt.% for all samples. Previously, in chapters 4.1.2.4 and 4.1.3 pure undoped Ga_2O_3 made by CVS and commercial Ga_2O_3 are compared and co-catalyst loadings were constant with 0.1 wt.% of both Cr_2O_3 and Rh, which is optimal for those samples. The results of doped samples are given in mmol h^{-1} per gram of catalyst. The results of the pure undoped Ga_2O_3 are given previously per 150 mg of powder (2.06 mmol h^{-1} and 0.86 mmol h^{-1} for H_2 and O_2). To compare those results with results of doped samples the production rates for pure undoped Ga_2O_3 are recalculated per gram of catalyst (13.7 mmol h^{-1} g_{cat}^{-1} and 5.7 mmol h^{-1} g_{cat}^{-1} for H_2 and O_2). Therefore, the photocatalytic activities of Mn doped Ga_2O_3 samples are lower than for the pure undoped Ga_2O_3. Due to high expenses, as for example Rh precursor, not always the same quantity of the powder via CVS could be produced for POWS testing, therefore, the activities are recalculated. The optimal co-catalyst loading per system is also important. For Mn-doped Ga_2O_3 an optimal loading of 0.2 wt.% of Rh and 0.1 wt.% of Cr_2O_3 is deposited. The activity of all doped samples in this thesis is expressed per gram of the catalyst and values obtained at optimal loading conditions are relevant and compared.

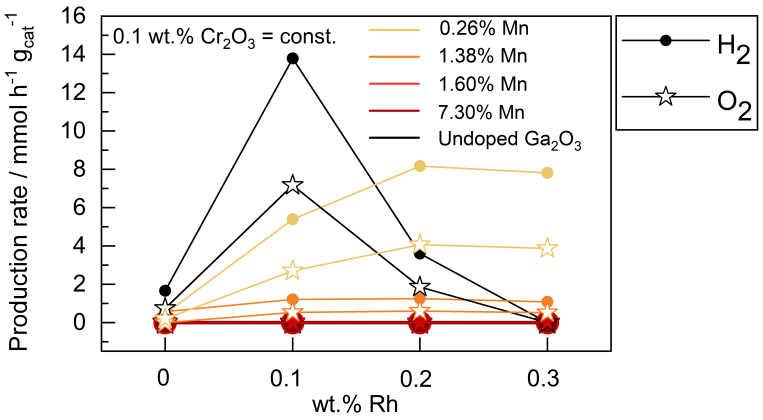

Fig. 4.29: POWS of the undoped and Mn-doped β-Ga_2O_3 samples as a function of Rh co-catalyst concentration in wt.% (concentration of the Cr_2O_3 co-catalyst is 0.1 wt.% = const.)

Addition of 0.2 wt.% of Rh co-catalyst to the sample doped with the smallest amount of 0.26 % of Mn shows the highest activity from all doped samples, but it is not higher compared to pure Ga_2O_3 with optimal loading. Higher dopant concentrations cause higher probability of defects in the material. This explains that with higher dopant concentration activity decreases and for samples doped with 1.6 % and 7.3 % it reaches zero regardless of amount of Rh co-catalyst. In addition, as will be shown by other doped systems, pure undoped Ga_2O_3 has in general the highest activity due to lowest defect density. For Rh co-catalyst concentration higher than 0.2 wt.% the activity level drops.

The results of the methanol reforming are shown in Figure 4.30 and again undoped β-Ga_2O_3 is the most active material with 105 mmol g_{cat}^{-1} h^{-1} and 3.5 mmol g_{cat}^{-1} h^{-1} of H_2 and CO_2, respectively. Samples doped with 1.6 % and 7.3 % of Mn show almost no activity at all. The methanol reforming activity strongly depends on the interaction of methanol molecule with the surface of the Ga_2O_3 nanoparticles, which is determined by the local surface chemical environment. Analyses of different types of methanol – gallium oxide adsorption interactions emerged during the study of Branda et al. [2006] involving DFT calculations, also experimentally supported by Pt:Ga_2O_3 – methanol systems. The calculations showed that methanol can react in three different ways with the surface of the Ga_2O_3 particles labeled as: non-dissociative and dissociative adsorption and oxidative decomposition. In general,

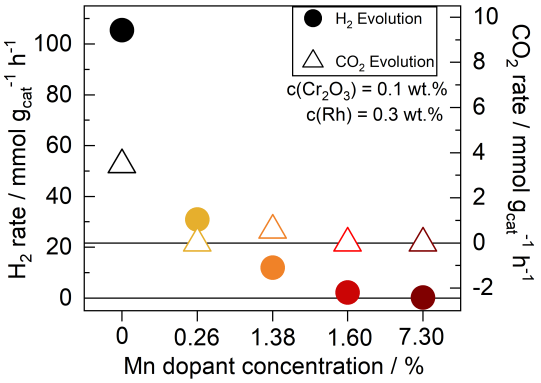

Fig. 4.30: Methanol reforming activity of the undoped and Mn-doped β-Ga_2O_3 samples, where c(Cr_2O_3) = 0.1 wt.% and c(Rh) = 0.3 wt.%

the study has found that if the surface of β-Ga_2O_3 contains no oxygen vacancies and defects it is very reactive. When methanol is adsorbed, a total oxidative decomposition occurs leading to the formation of intermediates and finally H_2 and CO_2. It is also expected that by doping with Mn the concentration of defects increases, therefore, lowering the decomposition efficiency of methanol on the surface. Also, as previously stated, a surplus amount of dopants on the surface can block active sites.

4.2.2 Rh- and Fe-doped β-Ga_2O_3

β-Ga_2O_3 is doped with 1% and 5% of Rh and 5 % of Fe in this work using $Rh(acac)_3$ and $Fe(acac)_3$ precursors, respectively. The XRD patterns are presented in Fig. 4.31A-B and the position of the diffraction peak assigned to the (512) lattice plane of β-Ga_2O_3 in the range 2Θ = 64° – 66° shifted to lower angles with increased amount of Rh, analogous to Mn-doped β-Ga_2O_3. Data observed from Rietveld refinement of the XRD patterns are presented in Table 4.3. The crystallite size of doped Ga_2O_3 is similar to undoped Ga_2O_3 and is in the range of 19 – 22 nm. The highest intensity of the most dominant reflection assigned to (002) for all samples is very similar. The lattice parameter expansion of Ga_2O_3 doped with 5% of Fe is slightly less than in case of doping with 5 % of Rh, as can be seen from Fig. 4.31. The radius of Rh^{3+} (0.67Å) is slightly larger than Fe^{3+} (0.64 Å) and Rh^{3+} is substituting octahedral Ga^{3+} ion (0.62Å) in the monoclinic structure. With increasing the Rh and Fe amount the band gap energy decreases (Fig. 4.31D) from 4.9 eV for the undoped sample to around 4.7 eV with 5 % of dopant. The intensity of the absorption edges becomes stronger with increasing dopant concentration, which originates from the new energy levels formed, as described before.

Concentration of the dopants in % presented in the Tables 4.2 and 4.3 are determined values when amounts of dopant and Ga (measured in at. % by EDS) are compared. Different areas of each sample with general chemical formula given as $(Dopant_xGa_{1-x})_2O_3$ are scanned at least six times for one hour to minimize the error.

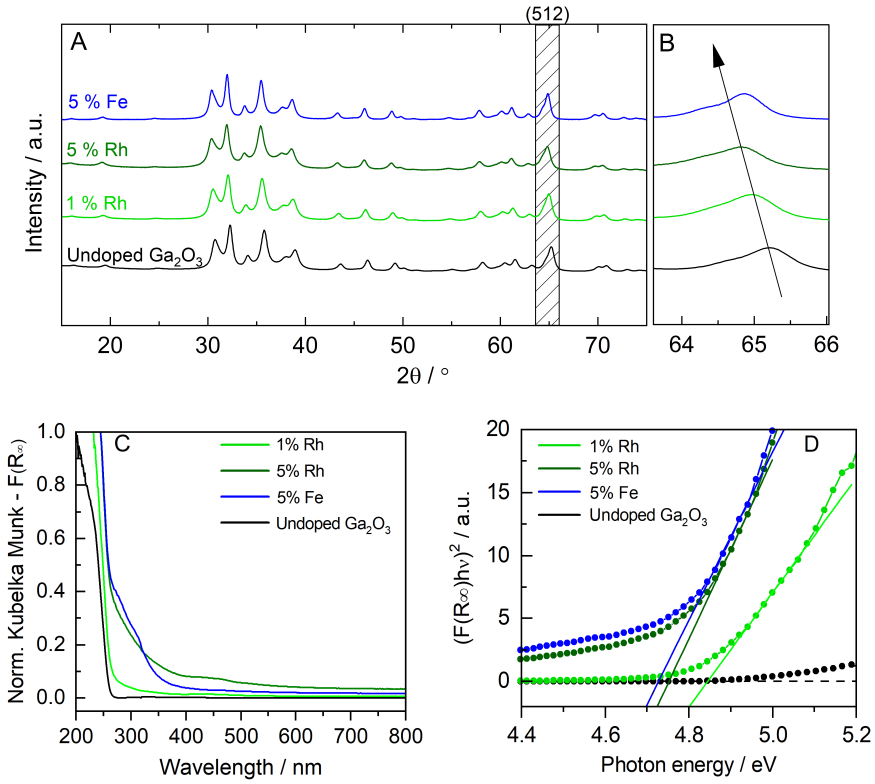

Fig. 4.31: A – X-ray diffraction patterns of the synthesized Fe- and Rh-doped β-Ga_2O_3 by CVS, **B** – Diffraction intensities between 64° – 66° showing a shift to a lower angle with increasing amount of dopants (direction shown by arrow), **C** – Reflectance spectra of undoped and doped Ga_2O_3 and **D –** Band gap energy of the samples determined by Tauc plots

Table 4.3. Structural data for the Rh- and Fe-doped β-Ga_2O_3 samples

C_{dopant} (%)	Color	d_{XRD} (nm)	Cell parameters				*MS* (%)	*Cell vol.* (Å^3)
			a (Å)	*b* (Å)	*c* (Å)	*β*(°)		
0		22 (1.1)	12.258	3.039	5.816	103.7	0.02(1)	210.5
1 (Rh)		21 (0.2)	12.268	3.045	5.817	103.7	0.02(5)	211.1
5 (Rh)		19 (0.7)	12.284	3.051	5.821	103.8	0.02(7)	211.9
5 (Fe)		20 (0.4)	12.263	3.041	5.816	103.8	0.01(5)	210.6
Bulk literature values for β-Ga_2O_3 by Geller [1960]			*a* = 12.232 ; *b* = 3.041 ; *c* = 5.801					

C_{dopant}	dopant concentration	*MS*	microstrain
d_{xrd}	crystallite size	*Cell vol.*	cell volume = $a \bullet b \bullet c \bullet sin\beta$

The activity for POWS, as well as for methanol reforming of pure Ga_2O_3 is again higher than for the doped samples, clearly evident in Figures 4.32 and 4.33. Toloman et al. [2015] in his study showed that doping with more than 3 % of Fe leads to the formation of a secondary α-Fe_2O_3 phase or as aforementioned $Fe^{3+}{}_xO_y$ oligomeric clusters, which when attached to the surface block active sites. This could be an explanation why the overall water splitting and methanol reforming activity is equal to zero for this sample. On the other hand, for 5 % Rh-doped Ga_2O_3 photocatalytic activity is detected. Without Rh co-catalyst and 0.1 wt.% of Cr_2O_3 loaded, only H_2 production of 0.461 mmol h^{-1} g_{cat}^{-1} is detected. With addition of 0.1 wt.% of Rh both H_2 and O_2 production rate of 0.241 mmol h^{-1} g_{cat}^{-1} and 0.085 mmol h^{-1} g_{cat}^{-1}, respectively, is detected. Still, those values are rather low. For additional Rh of 0.2 wt.% no catalytic activity is observed. Excess amount of Rh on the surface represents active sites for H_2 formation explaining the dominant non-stoichiometric production rate of H_2 compared to O_2. Yet, if the concentration is too high the activity decreases and Rh species represent recombination centers for photogenerated electrons and holes.

The conclusion drawn from the observed experiments is that incorporation of dopants into the crystal structure of CVS β-Ga_2O_3 does not improve the photocata-

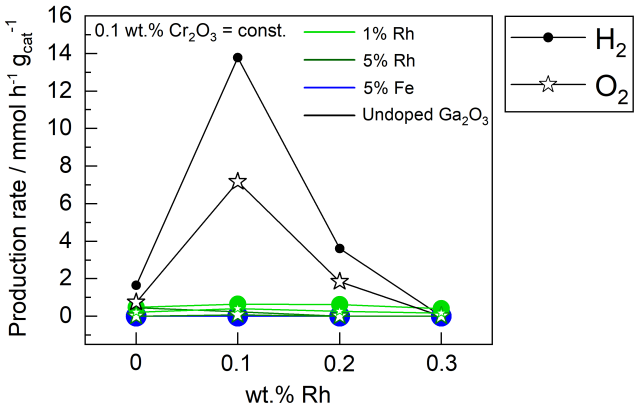

Fig. 4.32: POWS of the undoped and Rh and Fe-doped β-Ga_2O_3 samples as a function of Rh co-catalyst concentration in wt.%, where c(Cr_2O_3) = 0.1 wt.% remains constant

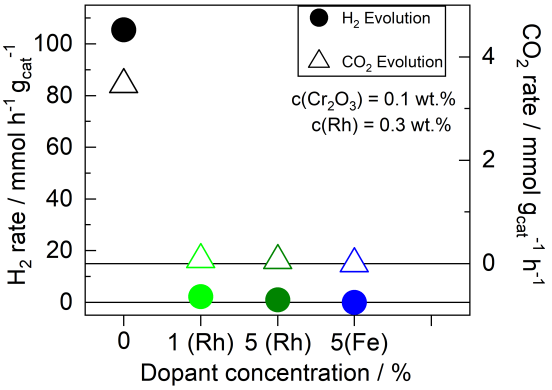

Fig. 4.33: Methanol reforming activity of the undoped and Rh and Fe-doped β-Ga_2O_3 samples, where c(Cr_2O_3) = 0.1 wt.% and c(Rh) = 0.3 wt.%

lytic activity when compared with activity of the starting oxide material. Therefore, such samples are not further investigated.

4.2.3 Synthesis of $(Zn_xGa_{1-x})_2O_3$ from Mixture of Two Solid Precursors

An intermediate step to obtain Zn-Ga oxynitride materials is the formation of oxide materials in the gas phase by evaporating combined Ga and Zn solid precursors. They are mixed and evaporated thermally with different starting weight ratios of 90:10, 80:20 and 70:30 %. 5g of $Ga(acac)_3$ precursor is evaporated together with 0.5, 1 and 1.5 g of $Zn(TMHD)_2$ in three separate syntheses. Process parameters are the same as for pure Ga_2O_3, but the evaporation temperature is set to 150°C instead of 190°C. From all acetylacetonate precursors used for doping in this work, $Zn(acac)_2$ has the lowest melting point (T_m = 125°C) and that is why $Zn(TMHD)_2$ is used instead (T_m = 150°C), which is closer to thermodynamic properties of $Ga(acac)_3$ (T_m = 196°C). Slower evaporation of the $Ga(acac)_3$ at T_{evap} = 150°C decreases the concentration of the monomers in the reaction zone and reduces further primary particle growth. As shown in Table 4.4 the observed crystallite sizes are between 11 nm and 14 nm and differ from 20 nm for pure Ga_2O_3, as previously reported. Correspondingly, the specific surface area is 20 – 30 m^2/g higher.

Table 4.4. Phase composition as a function of starting amount of $Zn(TMHD)_2$ mixed with $Ga(acac)_3$ in the precursor delivery zone in the CVS system

$Ga(acac)_3$: $Zn(TMHD)_2$	Zn:Ga Initial	Zn:Ga EDS	*SSA*	Phase composition			d_{XRD}		
				Ga_2O_3	$ZnGa_2O_4$	ZnO	Ga_2O_3	$ZnGa_2O_4$	ZnO
wt.%	ratio	ratio	m^2/g	wt.%			nm		
90:10	9	3.9	81	100	/	/	11	/	/
80:20	18	9.6	70	59	41	/	13	14	/
70:10	27	14.6	89	49	46	5	13	11	10

SSA specific surface area d_{XRD} crystallite size

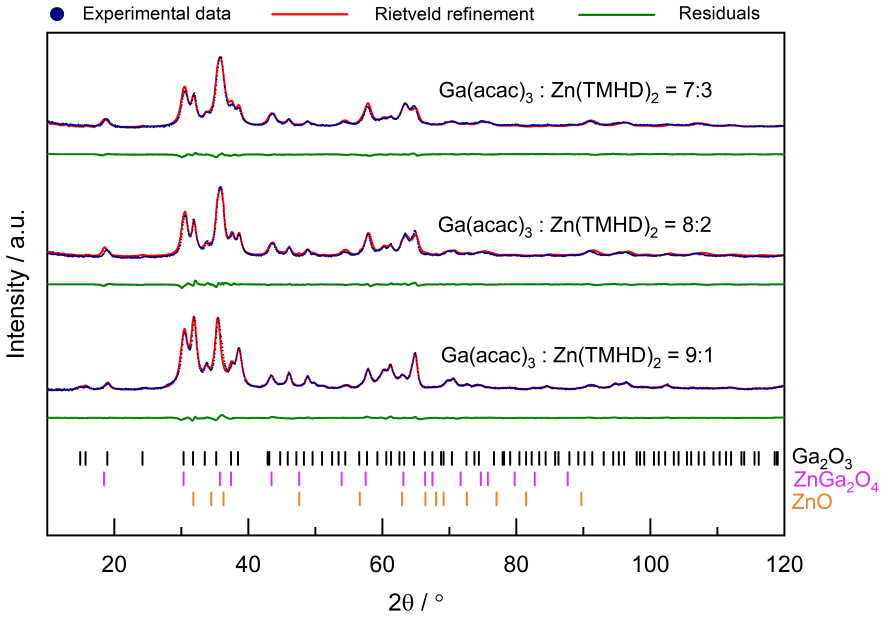

Fig. 4.34: Rietveld refinement of the XRD patterns of the $(Zn_xGa_{1-x})_2O_3$ samples synthesized from the starting mixtures of $Ga(acac)_3$ and $Zn(TMHD)_2$ with different weight ratios

The real values of the amount of Zn and Ga present in the sample are obtained from the EDS. At this high percentage of Zn, the material cannot be considered as doped, but as solid solution of ZnO and Ga_2O_3. With increasing Zn content, the formation of the spinel $ZnGa_2O_4$ and wurtzite ZnO as additional phases are observed. $(Zn_{0.03}Ga_{1.97})_2O_3$ sample (addition of 3% of Zn^{2+} with ionic radius of 0.74 Å) is the only sample that could be considered as doped and XRD pattern shows only monoclinic β-Ga_2O_3 phase. For this sample the shift of the Bragg reflections to lower

angles is insignificant, as well the change of unit cell volume, but also the band gap energy is typical as for pure Ga_2O_3 of 4.9 eV. Shimura et al. [2012] reported that the addition of 0.5 – 3 % of Zn^{2+} ions do not influence the crystallite size, specific surface area and the UV-Vis spectra. Those samples are made by homogenous precipitation (HP) method and also showed improved activity. However, doping of Ga_2O_3 with a metal like Zn^{2+} which has a smaller oxidation number than Ga^{3+} means the introduction of the oxygen vacancies in the crystal structure. The n-type semiconductor can gradually become a p-type. Below the conduction band at the donor level the original trap sites for the photoexcited electrons would decrease. Correspondingly, above the valence band the additional trap sites for photogenerated holes increase (Fig 4.35). According to Shimura et al. [2012] with substitutional Zn-doping and the formation of the additional trap sites the entire photocatalytic reaction rate is increased. In their work this is explained by a slight increase in thermal activation energy required for the smooth migration of holes. The migration of both electrons and holes is improved by the presence of an optimum amount of the dopant. However, when the concentration of Zn dopants is higher than 3 % an additional spinel $ZnGa_2O_4$ phase is formed decreasing the thermal activation energy and thus the migration of charge carriers. The formation of $ZnGa_2O_4$ in the bulk may generate recombination sites for the photogenerated electrons and holes at the boundary. As well, with doping structural strain in the crystal structure of Ga_2O_3 occurs and these morphological changes lower the photocatalytic reaction rate. However, in CVS the doping can be performed beyond thermodynamical limits [Winterer 2002].

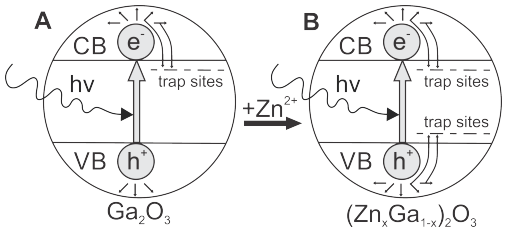

Fig. 4.35: Effect of the Zn doping on the migration of the photogenerated carriers: **A** – the photoexcited electrons in CB cannot smoothly migrate without Zn doping **B –** smooth migration of both electrons and holes when optimum amount of Zn dopant is present. Adjusted and reprinted from [Shimura et al. 2012]

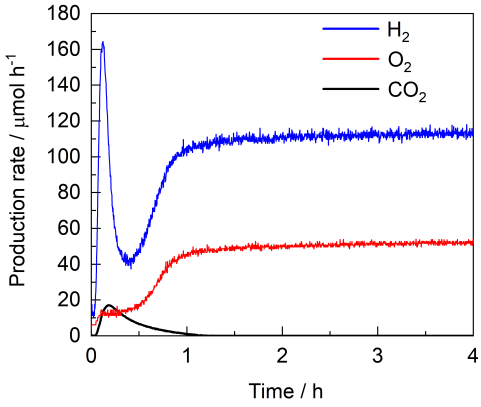

Fig. 4.36: 3 % Zn-doped Ga_2O_3 (150 mg) shows low POWS activity on µmol h^{-1} scale compared to pure Ga_2O_3 (H_2 = 2.06 mmol h^{-1} and O_2 = 0.86 mmol h^{-1} for 150 mg)

Considering that during the CVS process the Zn precursor sublimes faster than Ga precursor it is expected that Zn is not completely incorporated into the crystal structure of Ga_2O_3 or not uniformly distributed in the powder. With much shorter reaction times during CVS process Zn could be located on the surface of the particles or forming small ZnO nanoparticles which are in contact with surface of Zn-doped Ga_2O_3 blocking active sites. Unlike in the previous case, the Zn species will not diffuse into particles to form the spinel phase. Therefore, CVS 3% Zn-doped Ga_2O_3 shows low photocatalytic activity on the µmol h^{-1} g_{cat}^{-1} scale (Fig. 4.36), which is about two orders of magnitude lower than for pure Ga_2O_3 previously reported. H_2 and O_2 production rate of 150 µmol h^{-1} g_{cat}^{-1} and 30 µmol h^{-1} g_{cat}^{-1}, respectively, get constant after 1 h. Obviously, using solid precursors it is hard to control the process and get the desired end phase composition and specially to dope materials in the same way as with Mn, Rh and Fe ions.

4.3 Structure and Properties of Ga-Zn-Oxynitride

Nitridation can be considered as a process of partial or full substitution of oxygen atoms by nitrogen atoms in metal oxides like Ga_2O_3 and ZnO to form the desired

$(Ga_{1-x}Zn_x)(N_{1-x}O_x)$ material. The valence band maximum (VBM) in metal oxides consist of O 2p orbitals and, therefore, by doping with N atoms the new VBM of oxynitrides will consist of hybridized N 2p and O 2p orbitals. Since N 2p orbitals have a higher energy than O 2p orbitals it is expected that the VBM of the oxynitride is higher than the VBM of the metal oxide without affecting the conduction band minimum (CBM) [Wei and Zunger 1988]. By shifting the band edge positions, the band gap energy decreases potentially to values lower than 3 eV. Additionally, when Zn is incorporated into the crystal structure the electrons from Zn 3d orbitals and N 2p orbitals cause so called p-d repulsion in the upper part of the valence band [Maeda and Yashima 2005]. Therefore, the VBM will shift even higher decreasing the band gap energy to 2.4 – 2.8 eV [Maeda and Domen 2016]. In Figure 4.37 the electronic structures of the oxide materials before and after conversion into nitride and oxynitride phases are schematically presented.

For obtaining oxynitrides it is necessary to synthesize starting materials, such as mixture of Ga_2O_3 and ZnO or spinel structure $ZnGa_2O_4$. In this chapter the synthesis progress of such oxides by CVS is explained, as well the conventional and novel method of plasma nitridation process is described.

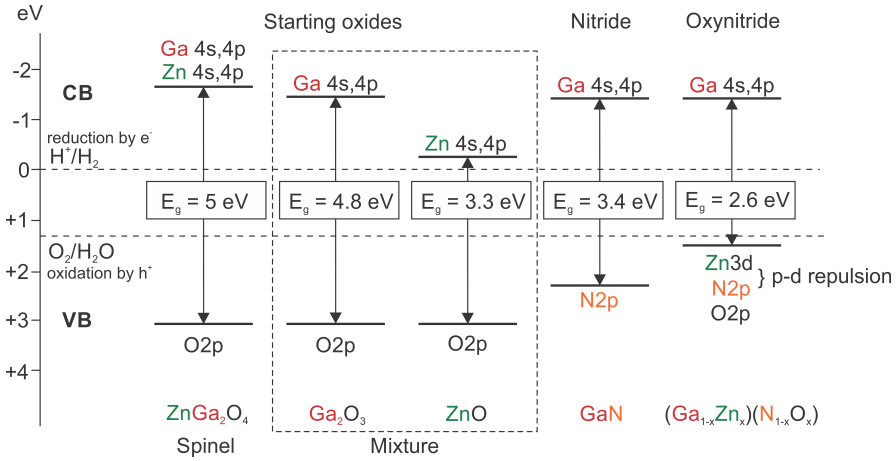

Fig. 4.37: Band edge positions and band gap energies of starting oxide materials like mixture of ZnO-Ga_2O_3 and $ZnGa_2O_4$ before and GaN and $(Ga_{1-x}Zn_x)(N_{1-x}O_x)$ after nitridation. Compiled from data of [Maeda and Domen 2016]

4.3.1 Route I: Synthesis of β-Ga_2O_3 and ZnO Mixture in the Gas Phase

Parts of this section are published in: Sasa Lukic, Gerdina Wilhelmina Busser, Siyuan Zhang, Jasper Menze, Martin Muhler, Christina Scheu and Markus Winterer. Nanocrystalline Ga-Zn Oxynitride Materials: Minimized Defect Density for Improved Photocatalytic activity? Z. Phys. Chem., 2019, 234, 1133-1153. doi:10.1515/zpch-2019-1432.

$(Ga_{1-x}Zn_x)(N_{1-x}O_x)$ or for simplification a solid solution of GaN and ZnO is formed during the nitridation process. ZnO incorporation into a GaN matrix takes place when the Ga-O bond is broken and converted to Ga-N. Therefore, the solid solution is not only formed on the solid-solid boundary between ZnO-GaN [Maeda et al. 2009]. These prior studies have noted the importance of particle sizes, especially if ZnO is much larger than Ga_2O_3, which leads to poor contact between particles and ZnO is not incorporated into the Ga-oxynitride matrix during nitridation. Therefore, a grinding/milling process of commercially available ZnO and Ga_2O_3 powders throughout few hours is one of the key factors for successfully obtaining a desired final material. Diffusion of Zn has an important role and depends on prior particle distribution homogeneity.

During synthesis of Ga_2O_3 and ZnO nanoparticles in the gas phase the intimate contact between particles is achieved. Photocatalytically active Ga_2O_3 nanoparticles are made by standard recipe from $Ga(acac)_3$ [Lukic et al. 2017] in a first reactor at 1200°C and 300 mbar. Using solid Zn precursor, as discussed in the previous chapter, narrows the process window making it impossible to control the end phase composition. On the other hand, crystallite sizes obtained for both ZnO and Ga_2O_3 are very similar and reaction takes place in only one reactor. In these series of experiments, as alternative a liquid diethylzinc (DEZ) precursor is added before the second reactor. The aim is to mix the nanoparticles homogeneously already in the gas stream in just few milliseconds, which is advantageous compared to commercial powders. Since the evaporation kinetics of $Ga(acac)_3$ and DEZ precursors completely differs, two separate evaporation zones are used. It is necessary to optimize

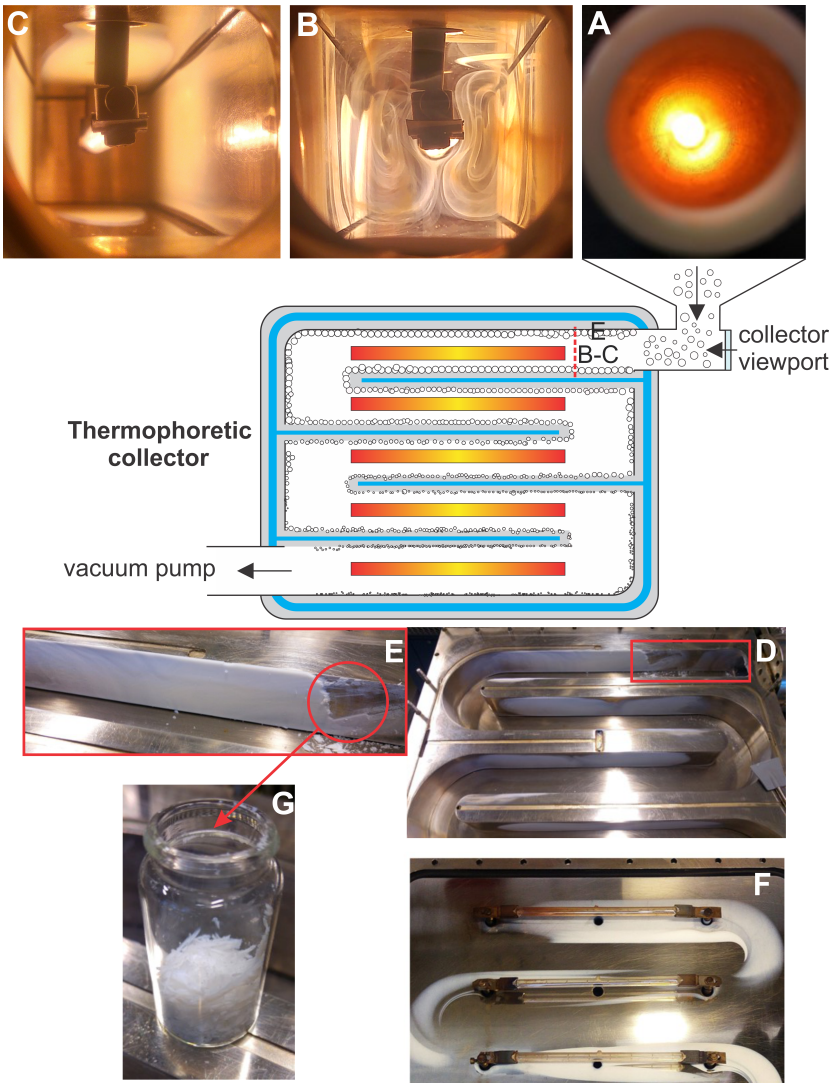

Fig. 4.38: Thermophoretic collector with 5 channels. **A** – reaction tube, **B** – mixed particles in the gas stream inside collector visible through glass CF port, **C** – particles deposited on the cold walls after synthesis, **D/E** – collector and enlarged first channel with particles being scraped of the wall, **F** – top of the collector with quartz lamps, **G** – collected fluffy powder

the process to enable good distribution of the particles. The schematic representation of the thermophoretic collector, as well as the flow process of gas stream with

particles and their collection is shown in Figure 4.38. DEZ starts to decompose already at room temperature (at applied pressure). Thus, formation of ZnO and their particle size is influenced by changing the temperature of the second wall reactor from low values such as: 300°C, 400°C and 500°C up to high value of 1000°C. At low temperatures a carbon layer surrounds the Ga_2O_3 particles due to partially decomposed DEZ decreasing the crystallinity of the collected powder. In Figure 4.39 the ratio of Zn/(Zn+Ga) obtained from EDS and from the phase composition according to Rietveld refinement of XRD data are compared. Here, XRD provides information only about the crystalline part of the materials, more specifically atomic fractions – in other words amount of Ga in crystalline monoclinic Ga_2O_3 or Zn in wurtzite ZnO. EDS, on other hand, gives information about the total amount of Zn or Ga in the sample regardless of crystallinity. The EDS and XRD values, as expected, differ much at lower temperatures due to incomplete precursor decomposition. At 1000°C the crystallinity of mixed semiconducting nanoparticles improves significantly (minimum defect density) and results are in very good agreement. Therefore, the focus is on Ga_2O_3-ZnO mixture synthesized at T_1 = 1200°C (first hot wall reactor) and T_2 = 1000°C (second hot wall reactor).

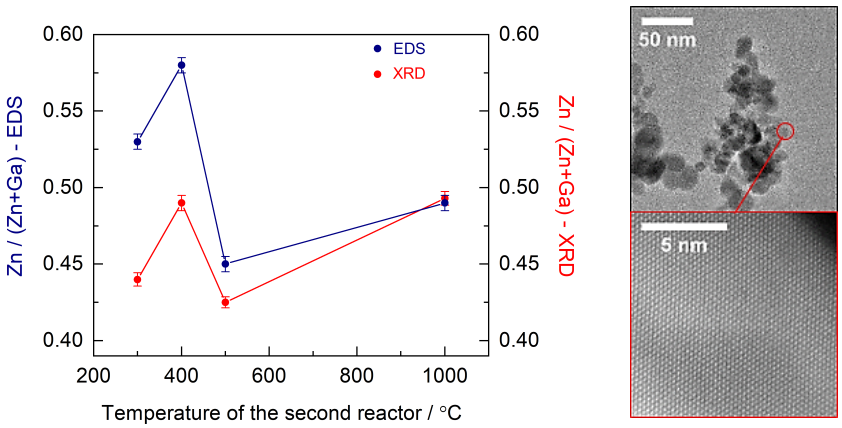

Fig. 4.39: Zn/(Zn+Ga) ratios obtained from EDS and computed from phase fractions extracted from Rietveld refinement of XRD data (left) and TEM images of the highly crystalline Ga_2O_3-ZnO nanoparticles (right)

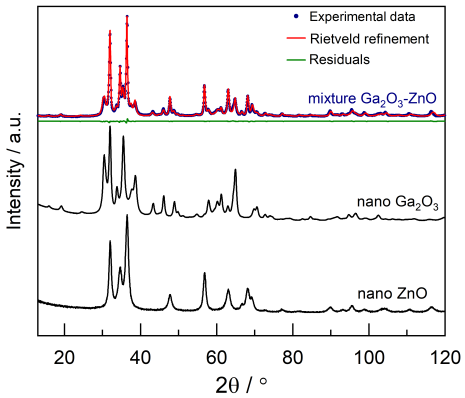

Fig. 4.40: Rietveld refinement of XRD data of a Ga_2O_3-ZnO mixture (51:49 wt%) compared to typical X-ray diffraction patterns of nanoscaled Ga_2O_3 and ZnO at the same CVS conditions

The XRD pattern in Figure 4.40 of the Ga_2O_3-ZnO mixture of nanoparticles is the combination of corresponding XRD patterns of pure monoclinic Ga_2O_3 and wurtzite ZnO, made previously by CVS at the same conditions. Very similar crystallite size of 16 nm and 18 nm and with weight ratio of 1:1 for Ga_2O_3 and ZnO, respectively, suggest that the process is well under control with narrow particle size distribution. Knowing the experimental yield of Ga_2O_3 it is possible to adjust the evaporation rate of DEZ for ZnO production, which will correspond to 450 mg/h of Ga_2O_3 usually made at standard conditions via CVS. At a pressure of 300 mbar a temperature of the bubbler of 15°C and a flow of helium of 50 sccm, DEZ will evaporate continuously with a rate of $1.58 \cdot 10^{-6}$ mol/s. The evaporation is much slower than at 20 mbar (usually used for liquid precursors in the CVS system). At these conditions the amount of the produced ZnO powder is about 450 mg/h.

Diffuse reflectance spectra presented in Figure 4.41 shows two different absorption edges and Tauc plots display typical direct band gaps (DBG) of 3.3 eV for ZnO and 4.8 eV for Ga_2O_3. Good elemental distribution of Ga and Zn in the mixed nanoparticles is displayed in Figure 4.42. Increasing the flow of helium to 75 sccm and 100 sccm through the bubbler caused higher concentration of DEZ in the carrier gas. This led to higher amount of Zn in the final powder with ratios Zn/(Zn+Ga) of 0.6 and 0.8, respectively.

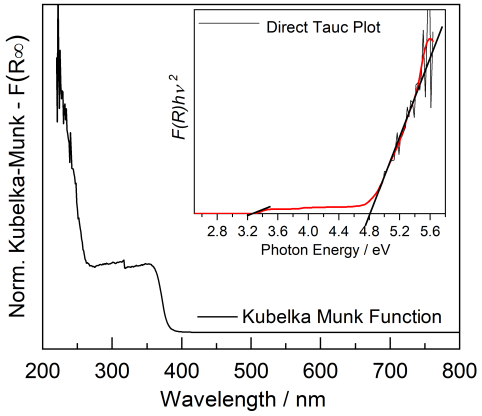

Fig. 4.41: UV/Vis absorbance spectra and direct Tauc plot of Ga_2O_3-ZnO mixture with typical band gap energies of 4.8 eV and 3.3 eV, respectively.

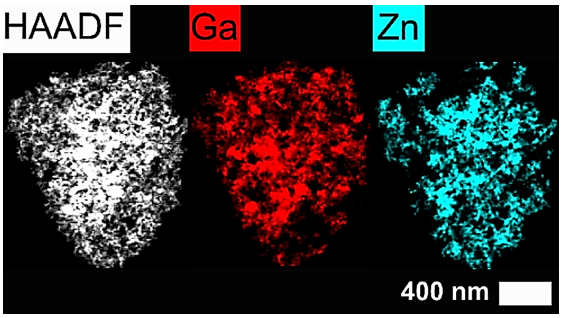

Fig. 4.42: High-angle annular dark field (HAADF) – STEM micrograph and the EDS elemental maps of Ga and Zn of Ga_2O_3-ZnO mixed nanoparticles

4.3.1.1 Nitridation of Ga_2O_3-ZnO Particles

The biggest challenge of the nitridation process is to control and reduce Zn volatilization. A ratio of Zn/(Zn+Ga) = 0.5 after the nitridation process could lead to very efficient water splitting under visible light according to DFT calculations [Jensen et al. 2008], but is experimentally still not accomplished using commercial powders. However, increasing flow of carrier gas and, therefore, concentration of Zn monomers in the reaction zone leads also to poor crystallinity of the ZnO nanoparticles. Optimal conditions are used to reach maximal Zn/(Zn+Ga) ratio of 0.49 in the starting mixture still preserving the desirable characteristics nanoparticles, which are

nitrided by varying nitridation time from 0.17 h to 10 h at 850°C. The effects of nitridation time on the microstructure and chemical composition of oxynitride nanoparticles are investigated in detail in this chapter. Since NH_3 decomposes at temperature above 850°C this is the optimal temperature and commonly used for the nitridation of Ga-Zn oxynitride material since discovery by [Maeda et al. 2005 and 2006]. In their work they obtained the highest activity for sample nitrided for 15 h with $x = 0.12$. For Ga_2O_3-ZnO CVS powders much shorter nitridation times can be used. Nanoscaled particles can have improved crystallinity and shorter diffusion distances for photoexcited carriers transported to the surface [Kay et al. 2006 and Osterloh et al. 2012]. As a common issue, during nitridation ZnO is reduced by H_2 (a byproduct of the NH_3 decomposition) and Zn becomes highly volatile. The rapid decrease of the Zn content from Zn/(Zn+Ga) = 0.29 after 0.25 h to 0.03 after 10 h of nitridation is presented in Figure 4.43. Additionally, Zn loss can be also directly observed as deposit on the inner wall of the nitridation tube in form of metallic Zn or ZnO after exposing the setup to ambient air, supported by XRD data (Fig. 4.44). Decrease of the Zn content causes a lower electron occupation in the upper valence band and shifts the VBM downward. Based on the onsets of diffuse reflectance spectra the band gap energy increases from 2.4 eV to 2.6 eV, which is substantially smaller than the band gap energies of GaN (3.4 eV) and ZnO (3.3 eV).

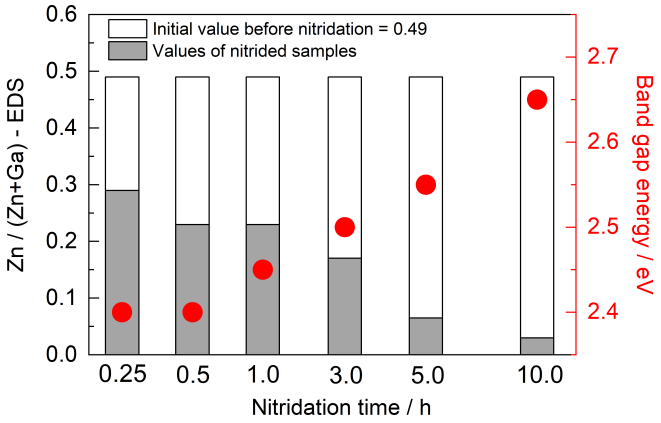

Fig. 4.43: Ratio of Zn/(Zn+Ga) is decreasing from 0.29 to 0.03 with increasing nitridation time, while band gap energy increases due to Zn evaporation

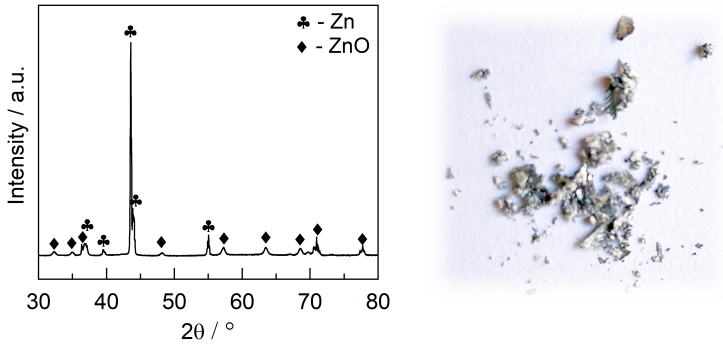

Fig. 4.44: XRD data confirms the presence of metallic Zn and ZnO deposited on the wall after nitridation (example shown for sample nitrided for 5h)

The band gap of a semiconductor is either direct (DBG) or indirect (IBG). Diffuse reflectance can be converted to absorbance using Kubelka-Munk equation: $A=(1-R_\infty)^2/2R_\infty$ where: $R_\infty = R_{sample} / R_{reference}$ and diffuse reflectance spectra are observed with $BaSO_4$ as reference material. Tauc plots are used to determine the optical band gap of semiconductors [Tauc et al. 1958 and Stenzel et al. 2005]. A Tauc plot is displayed as a function of $(ahv)^{1/r}$, where hv – photon energy, a – absorption coefficient of the material and r – exponent which denotes the nature of the transition [Davis et al. 1970]. If r is: ½ – direct transition and if 2 – indirect transition. Figure 4.45 displays that all oxynitride samples have indirect band gaps.

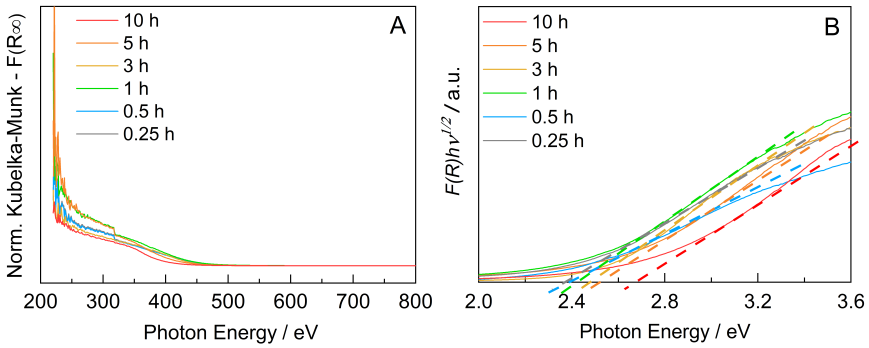

Fig. 4.45: A – Reflectance spectra presented by Kubelka-Munk equation and **B** –Tauc plot functions with exponent ½ indicating indirect band gap of all nitride samples from 2.4 eV to 2.65 eV with decrease of Zn/(Zn+Ga) from 0.29 to 0.03

IBGs lower the probability of light absorbance compared to semiconductors with DBG. This can be explained by energy states of CBM and VBM, which are characterized by a specific crystal momentum (*k*-vector). If *k*-vectors are identical, the momentum of electrons and holes is the same and the band gap is direct. Electrons can be directly excited when nanoparticles are irradiated with UV or visible light. On the other hand, if the vectors differ, those electrons must pass through an intermediate state and transfer the momentum to the crystal lattice. This demands absorption or emission of a phonon with momentum equal to difference of momentums between holes and electrons. This difference is schematically presented in Figure 4.46. Maeda et al. [2010] demonstrated that nitridation for less than 5 h did not lead to the formation of single wurtzite phase of GaN-ZnO solid solution. Particles were irregularly shaped when nitridation process took less than 15 h, while samples nitrided for even 30 h suffered from very low surface area. In addition, due to simultaneous diffusion of the Ga^{3+} and Zn^{2+} ions in the starting oxide mixture (commercially available) atomic composition strongly deviated even for the same particle. Using a mixture of CVS Ga_2O_3-ZnO and nitriding from 0.17 h to 10 h the crystalline GaN wurtzite phase is observed already after 0.25 h. Exposing to a reductive atmosphere the nitrided samples are not a physical mixture of GaN and ZnO, but a solid solution of these materials.

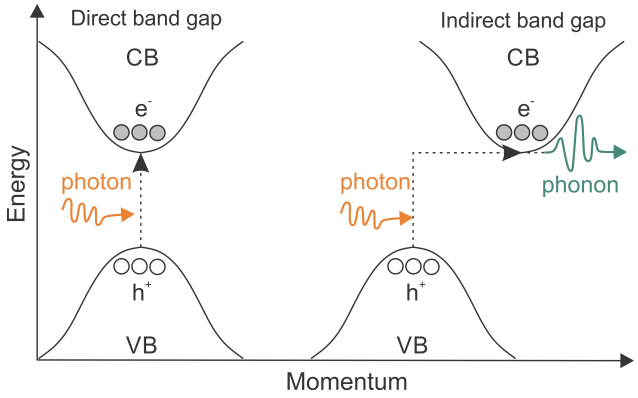

Fig. 4.46: Excitation and transition of an electron in semiconductors with direct and indirect band gap. Adapted and adjusted from [Valavanis 2009]

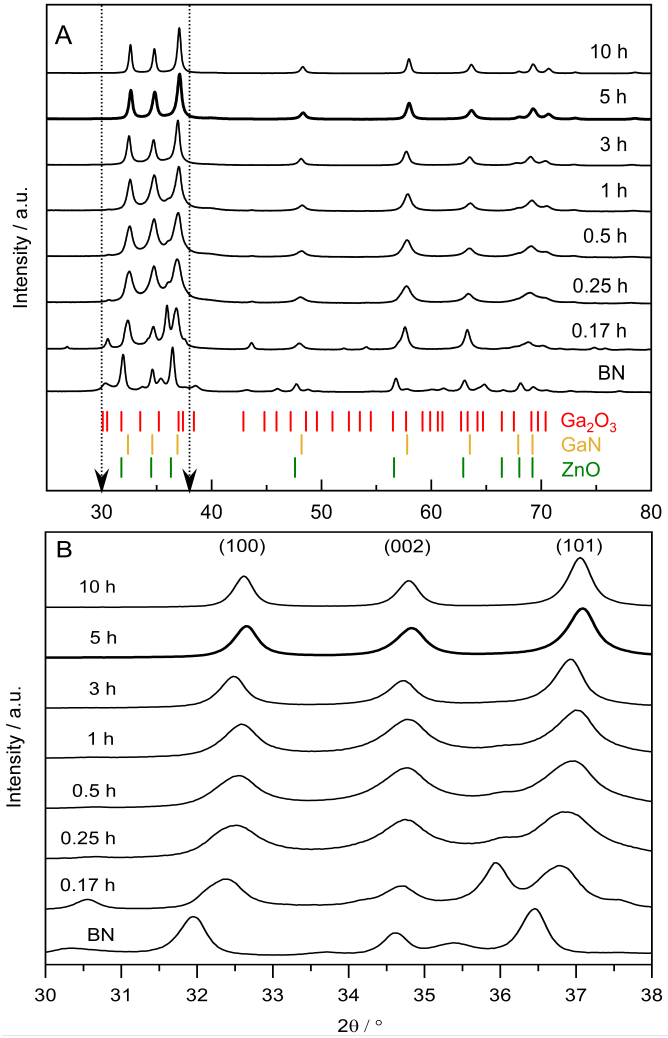

Fig. 4.47: A – overview of the X-ray diffractograms of the samples starting from the Ga_2O_3-ZnO mixture as a function of the nitridation time. Compared with Ga_2O_3 (ICSD #34243), ZnO (ICSD #26170) and GaN (ICSD #54698) as initial studying parameters and **B** – enlarged diffracted intensities in range 30° – 38°

In Figure 4.47 X-ray diffraction patterns are normalized to the individual maximum intensity for graphical clarity. GaN and ZnO as the main constituents of the solid solution have both wurtzite crystal structure and very similar lattice parameters. Diffraction intensities with positions (100), (002) and (101) shift to higher angles

upon loss of Zn. Suhulz et al. [1977] and Garcia-Martinez et al. [1997] reported that due to the small difference in *c*-axis lengths between GaN and ZnO the diffracted intensity with position (002) did not undergo a shift. However, for CVS nanoparticles this shift is visible and *a*- and *c*-axis length decreases almost linearly with decreasing Zn concentration. After a very short nitridation time of 0.17 h (10 min) the wurtzite phase is not observed, neither a monoclinic Ga_2O_3 phase. Excess amount of ZnO (68 wt.%), GaN (5.6 wt.%) and an intermediate $ZnGa_2O_4$ phase (26.4 wt.%) are observed. The spinel $ZnGa_2O_4$ converts to the desired $(Ga_{1-x}Zn_x)(N_{1-x}O_x)$. Therefore, the Zn content in the oxynitride made by this synthetic route is limited by the spinel intermediate composition to a maximum Ga/(Ga+Zn) = 0.33 and the rate of Zn volatilization [Chen et al. 2009]. The detailed change of the phase composition as a function of time is presented in Figure 4.48. At 0.25 h and longer nitridation times a shift of the Bragg reflection in the region $2\Theta = 30° – 38°$ is observed due to an increase of GaN and a decrease of ZnO content, as previously described by Domen et al. [2005]. The energy necessary to break the Zn-O bond is lower (1.65 eV) than for the Ga-O bond (3.66 eV) which explains the loss of Zn during nitridation with GaN being the dominant constituent after 10 h with a very low ratio of Zn/(Zn+Ga) = 0.03.

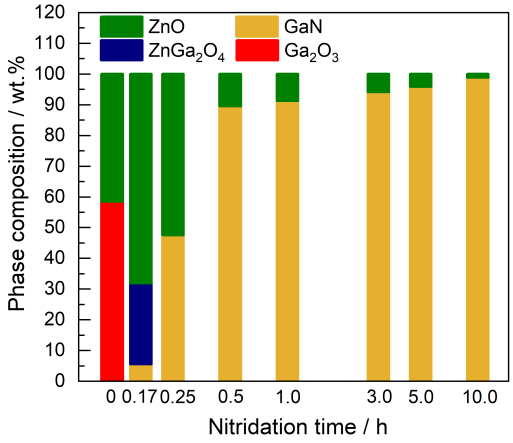

Fig. 4.48: Change of the phase composition with nitridation time from starting Ga_2O_3-ZnO mixture (58.6 : 41.4 wt.%)

Table 4.5. Compiled data of nitrided CVS samples as a function of nitridation time

t	*CS*	*MS*	*Γ*	*SSA*	*IF*	*TF*	*LP [a ; b ; c]*
h	nm	%	/	m^2/g	%	%	Å
0	16.2 ± 0.8 17.9 ± 2.8	0.21 ± 0.066 0.68 ± 0.086	0.46	65.6	/ 4.6 ± 0.40	/ 4.3 ± 0.73	12.248; 3.037; 5.808 3.252; - ; 5.212
0.25	9.4 ± 0.1	0.28 ± 0.021	0.51	46.2	2.36 ± 0.10	2.48 ± 0.11	3.211; - ; 5.214
0.5	9.4 ± 0.9	0.26 ± 0.014	0.53	42.6	2.45 ± 0.10	2.56 ± 0.12	3.211; - ; 5.217
1	10.6 ± 0.9	0.21 ± 0.027	0.55	33.3	2.36 ± 0.10	2.48 ± 0.11	3.206; - ; 5.212
3	15.6 ± 0.4	0.06 ± 0.002	0.57	32.9	0.40 ± 0.01	0.71 ± 0.05	3.206; - ; 5.202
5	18.9 ± 0.2	0.03 ± 0.003	0.64	17.8	0.42 ± 0.04	0.84 ± 0.07	3.197; - ; 5.197
10	30.4 ± 0.7	0.01 ± 0.002	0.70	14.7	0.36 ± 0.02	0.41 ± 0.03	3.194; - ; 5.193

t	nitridation time	*TF*	Twin fault probability
CS	crystallite size	*LP*	lattice parameters
MS	microstrain	*Red*	β-Ga_2O_3 phase
Γ	degree of crystallinity	*Green*	ZnO phase
SSA	specific surface area	*Black*	$(Ga_{1-x}Zn_x)(N_{1-x}O_x)$
IF	intrinsic (stacking) fault probability		

Crystal structure and microstructure is analyzed using Rietveld refinement of XRD patterns (Table 4.5) to better understand the relation between particle characteristics and their photocatalytic behavior information about phase composition. Local variations of lattice constants are due to defects in the crystal structure [Leineweber 2011]. Using a combination of Popa model for size and strain, as well Warren theory for planar defects for hexagonal closed pack (HGP) crystal structure the probability of intrinsic and twin faults is obtained [Popa 1998 and Warren 1990]. Defects may

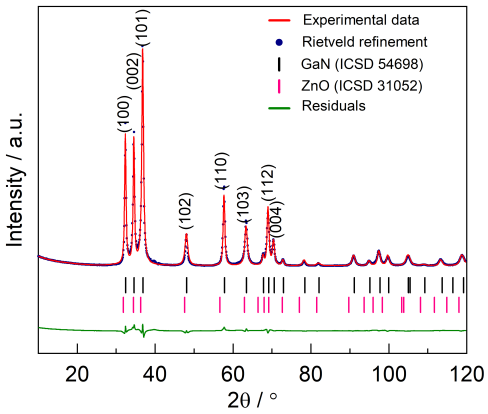

Fig. 4.49: XRD pattern of the sample nitrided for 5 h fitted by Rietveld refinement using MAUD. Compared with GaN (ICSD #54698) and ZnO (ICSD #26170) references as initial studying parameters

act as traps for charge carriers leading to recombination of electrons and holes, thus deteriorating charge carrier transport to the surface and lowering photocatalytic activity. A typical Rietveld refinement for sample nitrided for 5 h, which shows the highest photocatalytic activity, is shown in Figure 4.49.

In Figure 4.50A with increasing nitridation time microstrain decreases, which is associated with formation of $(Ga_{1-x}Zn_x)(N_{1-x}O_x)$. The crystallite size increases from about 9 to 30 nm followed by decrease in specific surface area from 46 m^2/g to 14.7 m^2/g, which are still larger compared to those obtained using solid-state reaction in previous studies with less than 10 m^2/g [Sun et al. 2007, Maeda and Hisatomi 2009]. As well with increasing nitridation time the probability of intrinsic (stacking) and twin faults is decreasing indicating lower defect densities. Contrary to expectations, higher nitridation temperature than 850°C would not lead to higher crystallization, but induce formation of Zn defects in the material [Maeda et al. 2005]. In Figure 4.50D lattice parameters *a* and *c* of the nitrided samples are between values of wurtzite ZnO and GaN crystal structure (space group $P6_3mc$). With longer nitridation time these values approach values for GaN, although it must be mentioned that the remaining deviation from the bulk values could be also due to the nanoscaled nature of the particles [Diehm et al. 2012].

A decrease in specific surface area significantly reduces the number of the reaction sites, thus lowering photocatalytic activity [Kudo et al. 1988 and Ikeda et al. 1998]. Many other factors can also affect the PL activity, like surface structure and surface morphology, as well the type and amount of the co-catalysts. Considering the crystallinity, all the indicators show a decrease of the defect density, which should lower the recombination rate and improve the photocatalytic activity. However, visible light absorption originates from Zn and O impurities [Hirai et al. 2007]. Hence, the nitrided samples may be active only under UV light compared to parent oxide mixtures. Beside planar defects (intrinsic and twin faults), as determined from the XRD data using Rietveld refinement, linear defects (dislocations) and point defects are also present in the crystal structure enhancing the recombination probability. Substituting Ga^{3+} with Zn^{2+}, regarding their ionic radii, an extension of the lat-

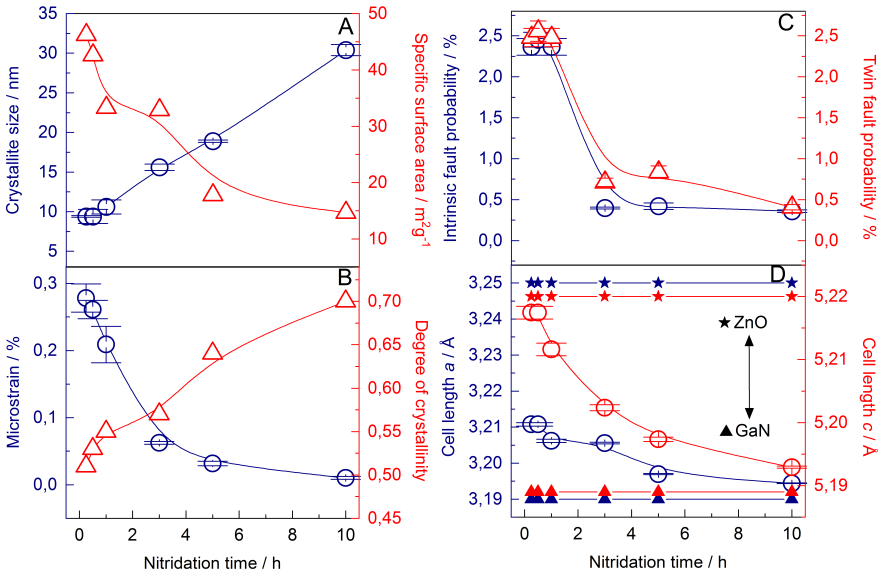

Fig. 4.50: Influence of nitridation time on: **A** – crystallite size and specific surface area. **B** – Microstrain and degree of crystallinity, **C** – Intrinsic (stack) and twin fault probabilities and **D** – Cell length *a* and *c* with ZnO and GaN bulk values (B-splines are intended as a guide to the eye)

tice parameters is observed and the oxygen vacancies are formed due to different oxidation numbers of Ga^{3+} and Zn^{2+}. Group of vacancies could form clusters, as well the impurities and form a different phase. The distribution of the crystal structure constituents also depends on the precursor purity.

In Figure 4.51 PL spectra are presented for pure β-Ga_2O_3, the starting CVS mixture Ga_2O_3-ZnO and the $(Ga_{1-x}Zn_x)(N_{1-x}O_x)$ sample nitrided for 5 h. As noted by Binet [1998], Shimamura [2008], Ho [2010] and Vasyltsiv [2019] the PL spectrum of Ga_2O_3 can be divided into three elementary bands with the maximum near UV (380 nm – 390 nm), blue (440 nm – 450 nm) and green (530 nm – 540 nm) spectral region. Onuma et al. [2018] found that the UV band luminescence is not dependent on impurities in the material, but refers to the recombination of free electrons and self-trapped holes, which cannot be seen in Figure 4.51. However, no significant evidence of luminescence in the UV region (100 – 400 nm) for CVS β-Ga_2O_3 is detected, what might be one of the reasons for higher activity of the oxide compared

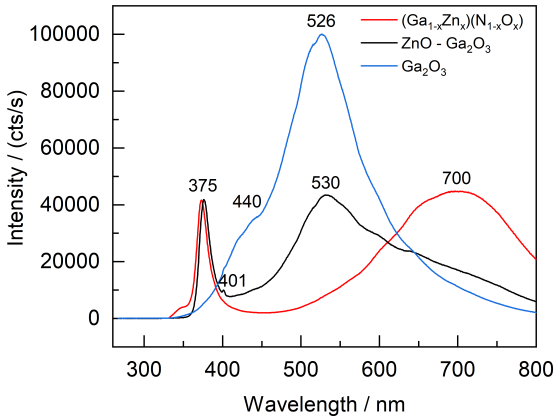

Region	Type/Color	Wavelength (nm)
UV	UV-C	100 - 280
UV	UV-B	280 - 315
UV	UV-A	315 - 400
Visible	Purple	400 - 435
Visible	Blue	435 - 480
Visible	Cyan	480 - 490
Visible	Blue green	490 - 500
Visible	Green	500 - 560
Visible	Yellow green	560 - 580
Visible	Yellow	580 - 595
Visible	Orange	595 - 610
Visible	Red	610 - 750
Visible	Red violet	750 - 800

Fig. 4.51: Photoluminescence spectra (STP – 1 atm and 25°C) of CVS samples: Ga_2O_3 (blue), Ga_2O_3-ZnO (black) and $(Ga_{1-x}Zn_x)(N_{1-x}O_x)$ nitrided for 5 h (red)

to nitrided samples when irradiated with UV light. The band at 400 nm (blue emission) stems probably from the recombination of an electron – a donor formed by an oxygen vacancy (V_o) and a hole – acceptor formed by a gallium vacancy (V_{Ga}) [Qian et al. 2008]. High intensity luminescence with maximum at 526 nm (green emission) could be attributed to some defects due to impurities in the material, as previously found by [Wang 2017, Gupta 2014 and Hu 2017]. Mixed CVS Ga_2O_3-ZnO powder exhibit two emission bands and one at 375 nm in the UV region, typical for ZnO, originates from recombination of free excitons. The other peak at 530 nm is attributed to single ionized oxygen vacancy [Yang et al. 2002 and Prabhakar et al. 2012] or the photogenerated hole interacts with an electron from occupying oxygen vacancy and causing radiative recombination [Vanheusden et al. 1996]. This peak is overlapping with a peak from previously described green emission for Ga_2O_3, but with a lower overall intensity. The weaker this luminescence is, the slower is the rate of electron-hole recombination. This is also observed for the nitrided sample $(Ga_{1-x}Zn_x)(N_{1-x}O_x)$. The solid solution of ZnO and GaN has an emission band at 375 nm in the UV region, the same as for the parent oxide mixture, which could be attributed to both phases coming from electron-hole recombination. On the other hand, the red emission with a peak at 700 nm refers to oxygen vacancies (V_o) due to substitution with nitrogen when the sample is exposed to NH_3 during nitridation.

As previously found by Lorenz et al. [2013] the yellow emission is frequently seen in GaN. The red shift corroborates an increase of defect density followed by heavy doping, where Ga is substituted by Zn and O by N during nitridation. In the work of Zeng et al. [2006] on doping GaN with Mg a strong correlation is shown between the vacancy concentration and the intensity of the red luminescence with a band at 1.8 eV (690 nm). Recently, Ouhbi and Aschauer [2019] reported a self-healing effect of anionic vacancies for TaON. They found an energetic preference for oxygen and nitrogen vacancies preferring surface sites where they are 'healed' by *O and *OH adsorbates under OER conditions.

Atomic high resolution STEM images of the wurtzite crystal structure of oxynitride sample $(Ga_{1-x}Zn_x)(N_{1-x}O_x)$ analyzed in the Figure 4.52 shows high crystallinity from core to the surface of the particles in general. Stacking faults are visible along the [11-20] axis validating the data from Rietveld refinement of XRD pattern for the sample nitrided for 5 h.

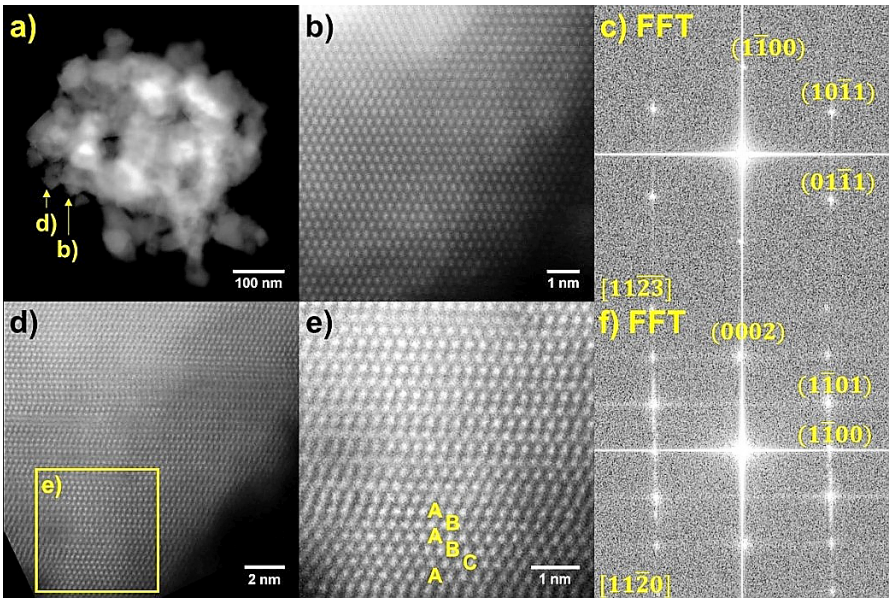

Fig. 4.52: a – STEM images of $(Ga_{1-x}Zn_x)(N_{1-x}O_x)$ nitrided for 5 h, **b/e** – atomic resolution micrographs along [11-23] and [11-20] axis with **c/f** – their Fast Fourier Transformation (FFT) and **e** – stacking faults (layer C) labelled in the hexagonal ABȦḂ layer order along the (0002) plane

4.3.1.2 Photocatalytic Activity of the Ga_2O_3-ZnO Starting Mixture and *in situ* Photo-deposition of Rh/Cr_2O_3 Co-catalysts

As a reference material 150 mg of CVS prepared Ga_2O_3-ZnO mixture is dispersed into 500 mL of water and loaded with Rh- and Cr- containing co-catalysts by stepwise *in-situ* photodeposition. The optimum loading of 0.1 wt.% Cr_2O_3 and 0.1 wt.% Rh for commercial and CVS Ga_2O_3, as well as the order of addition (first Cr_2O_3, then Rh) were determined previously by Busser et al. [2012]. Without adding the sacrificial agent (MeOH) first a small amount of 0.45 mL of a solution containing K_2CrO_4 is added (leads to 0.1 wt.% Cr_2O_3) and flushed with nitrogen for 1 h. After a degassing step, the mercury lamp, which emits light with wavelengths in range 250 – 600 nm is switched on and sensors for H_2, O_2 and CO_2 monitor and measure their initial evolution rate. The corresponding results are presented in Figure 4.53. In the first hour just a small amount of CO_2 is observed due to oxidation of carbonaceous residues. Cr_2O_3 serves as an oxidation catalyst [Soldat et al. 2016]. Adding 0.6 mL of $Na_3RhCl_6 \cdot 3H_2O$ solution (leads to 0.1 wt.% Rh) is performed so many times until the production rate of evolved gases reaches saturation and does not ch-

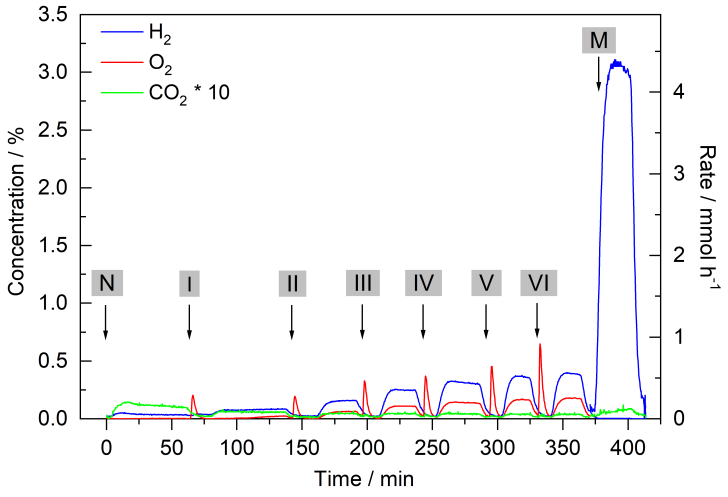

Fig. 4.53: POWS and methanol reforming of CVS prepared Ga_2O_3-ZnO mixture. N : light on, addition of K_2CrO_4 (0.1 wt.% Cr_2O_3); I – VI : light on, addition of $Na_3RhCl_6 \cdot 3H_2O$ (0.1 – 0.6 wt.% of Rh, respectively) and M : light on, addition MeOH (methanol reforming for enhanced H_2 production). The data is obtained for 150 mg of catalyst in real time

ange significantly anymore. Every time the Rh-containing solution is added air is introduced as well and the system needs to be flushed with nitrogen. Consequently, sharp peaks for oxygen evolution are visible in the graph. O_2 evolution starts when the concentration of CO_2 decreases sufficiently. On the other hand, Rh is a powerful H_2 evolution co-catalyst. As shown for pure Ga_2O_3 the optimal loading is 0.1 wt.% Rh, for doped samples 0.2 wt.% Rh, while in the case of mixed Ga_2O_3-ZnO this value reaches 0.6 wt.% Rh. This is probably due to the presence of ZnO on the surface of the particles. Compared to POWS reaction methanol reforming is a relatively facile reaction and methanol is used as a hole scavenger. At the end 20 mL of MeOH is added and during 30 min of irradiation by lamp the H_2 evolution increases significantly above 4 mmol h^{-1}, while the OER rate drops to zero followed by a slight increase of CO_2 concentration, as expected.

4.3.1.3 Photocatalytic Activity of the $(Ga_{1-x}Zn_x)(N_{1-x}O_x)$ and *in situ* Photo-deposition of Rh/Cr_2O_3 Co-catalysts

The POWS results of the starting oxide mixture and the nitrided samples are compared in Figure 4.54. POWS is a thermodynamic uphill and relatively slow reaction, which competes with high recombination rates in defect rich materials. Neither short nor very long nitridation times lead to highest activity, but optimal conditions. A high specific surface area is indeed necessary for the adsorption and photocatalytic degradation of organic compounds, but it decreases significantly with longer nitridation times. In contrast, Kudo and Miseki [2009] point out that the critical factor for POWS is the defect concentration. A high degree of crystallinity is, therefore, more beneficial than a high specific surface area and according to Maeda et al. [2008] the H_2 evolution depends on the structural properties of material and represents the rate determining factor. The optimum nitridation time is 5 h and the sample is regarded as one of the most promising for photocatalytic applications with little microstrain and low defect density (Figure 4.50). The Zn content is considerably lower as in the starting material, but there is still a significant amount (x = 0.06) and reasonably high specific surface area (17 m^2/g). The band gap of 2.55 eV suggest that $(Ga_{1-x}Zn_x)(N_{1-x}O_x)$ should be more active than its parent oxide mixture of Ga_2O_3

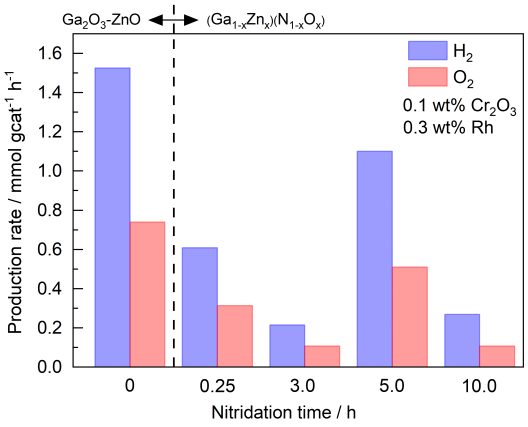

Fig. 4.54: Comparison of POWS activity of Ga-Zn-oxynitrides with parent Ga_2O_3-ZnO starting mixture. All results are recalculated per gram of catalyst and optimal loading for nitrided samples is considered (0.1 wt.% Cr_2O_3 and 0.3 wt.% Rh)

and ZnO. However, photocatalysis favors semiconductors with DBG and for those with IBG the efficiency decreases and this is the most likely the explanation for the lower activity of these oxynitrides. The material shows no activity when a light source with visible light (Xe lamp) was applied.

The problems regarding lower and diverse photocatalytic activities measured for $(Ga_{1-x}Zn_x)(N_{1-x}O_x)$ under visible light irradiation is also reported in the work by Zhang et al. [2014]. It is demonstrated that large differences in activity are the result of small differences in the surface composition of the particles, especially when working with solid precursors. Therefore, creating an active material is a very sensitive process. The other possible reason for low activity could be the contact between semiconductor and co-catalyst, as well the oxidation state of Rh particles. Smaller Rh particles are easier attached to the surface (Figure 4.55) on already small nanoparticles and harder to be washed away during POWS experiments. In chapter 4.2 an excess amount of Rh metal during doping of Ga_2O_3 could oxidize easily when the reactor is opened to add solution and the co-catalyst efficiency decreases.

The optimal co-catalyst loading for $(Ga_{1-x}Zn_x)(N_{1-x}O_x)$ prepared by nitridation of physical mixture of Ga_2O_3-ZnO, previously obtained by performing high tempera-

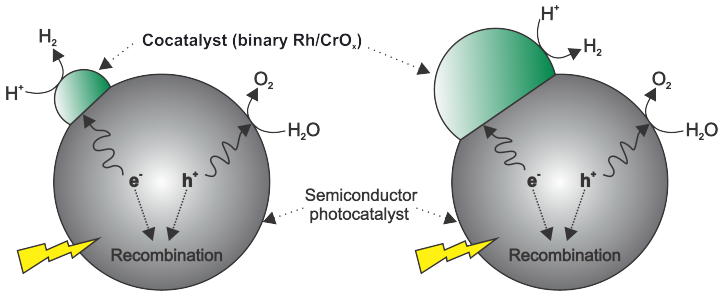

Fig. 4.55: The stability of the co-catalyst attached on the surface of semiconducting nanoparticles is size-dependent. The co-catalyst particles with higher specific surface area should oxidize stronger. Graphical illustration is created using CorelDRAW X8

ture solid-state synthesis by Maeda et al. [2005], is determined to 0.1 wt.% Cr_2O_3 and 0.3 wt.% Rh [Sakamoto et al. 2009 and Busser et al. 2012]. For oxynitrides prepared by a CVS Rh-solution is added to the system already containing 0.1 wt.% Cr_2O_3. The optimum loading is 0.3 wt.% Rh (Figure 4.56), which is in a good agreement with previous results and further addition does not lead to a significant increase in H_2/O_2 evolution.

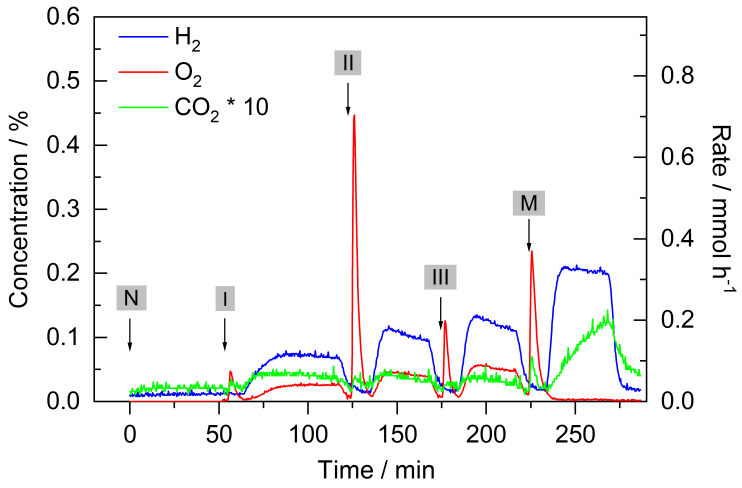

Fig. 4.56: POWS and methanol reforming of $(Ga_xZn_{1-x})(N_{1-x}O_x)$ nitrided for 5 h. N : light on, addition of K_2CrO_4 (0.1 wt.% Cr_2O_3); I – III : light on, addition of $Na_3RhCl_6 \cdot 3H_2O$ (0.1-0.3 wt.% of Rh, respectively) and M : light on, addition MeOH (methanol reforming for enhanced H_2 production). The data is obtained for 150 mg of catalyst in real time

Hyper mapping performed using EDS displays the local element distribution in CVS powder modified with co-catalysts to monitor their homogeneity (Figure 4.57). Optimal loading of 0.3 wt.% corresponds to nominal ratio of Rh/(Ga+Zn) of 0.27. After noise reduction of the EDS spectrum imaging by multivariate analysis [Zhang et al. 2018], only the Rh-L peak is visible. The Cr-K peak is not observed due to very low concentration (three times less than concentration of Rh in the sample) which is below the EDS detection limit. The presence of Cu stems from the TEM grid. Table 4.6 lists the average Rh/(Ga+Zn) ratios for three different EDS mapping performed on different single particles, which are 3-4 times higher than the nominal ratio. This is explained by the variation of the local concentration. Rh is a much heavier element than Ga and Zn and based on the atomic number contrast it should stand out in the HAADF-STEM image. Rh particles are small and observed as subnanometer bright features, which could be attributed to atomic clusters. Rh is not fixed, but moving fast on the surface of the CVS nanoparticles, which is clearly visible while doing the analysis. This explains why Rh is observed uniformly

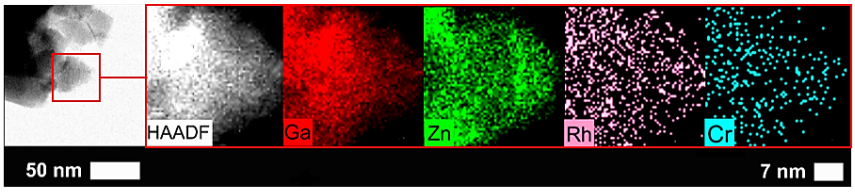

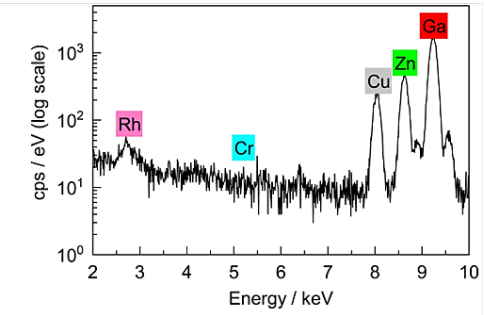

Table 4.6. Local distribution of Rh observed in EDS maps

	Rh/(Ga+Zn)
Nominal composition	0.27
EDS 1	0.89
EDS 2	0.83
EDS 3	1.15
EDS average	0.95

Fig. 4.57: Elemental distribution and homogeneity in $(Ga_xZn_{1-x})(N_{1-x}O_x)$ nitrided for 5 h by EDS/TEM after the *in situ* photodeposition of the binary Cr_2O_3/Rh co-catalysts and POWS experiment is performed

in the elemental map. Unfortunately, due to technical limitations and their fast movement 'catching' this Rh features on the TEM images is not possible. It can be stated that the co-catalyst is present in a fairly dispersed condition.

As part of future work, a synthesis of semiconducting nanoparticles together with co-catalysts via CVS may be considered. Few disadvantages occur regarding this methodology when the synthesis is carried out. In the first step Ga_2O_3-ZnO nanoparticles are made and left uncollected in the thermophoretic collector. In the second step the process parameters are changed (p = 20 mbar), so that the reaction time is shorter and smaller Cr_2O_3 nanoparticles of about 2 – 3 nm are synthesized. Green chromia nanoparticles are attached to the surface of the Ga_2O_3-ZnO layers on the walls of the collector followed by an uneven distribution (Fig. 4.58). Obviously, the main drawback of this method is that the semiconducting nanoparticles are not nitrided. This is necessary to achieve directly in the CVS, which would consequently lead to interaction of Ga-Zn species with Cr and form undesired crystal structures. At the same time, Cr_2O_3 can be also nitrided and form CrN for example. A new approach and technical improvements are necessary to be able to make such a complex structures in the gas phase. This is especially important for nanosized metal Rh nanoparticles, which will be oxidized instantly after opening the particle collector compared to *in situ* photodeposition.

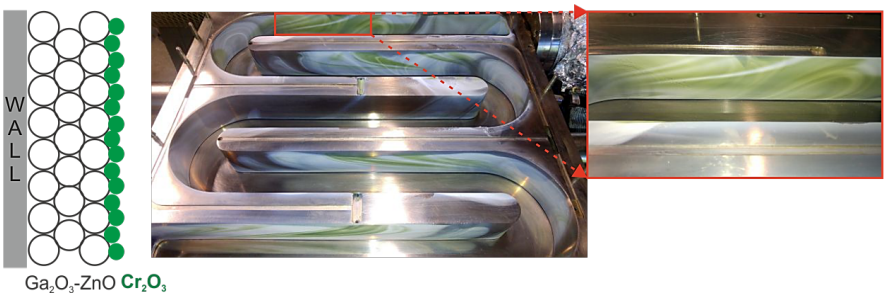

Fig. 4.58: Non-uniform distribution of Cr_2O_3 co-catalyst nanoparticles on the layers of CVS Ga_2O_3-ZnO synthesized powder

4.3.2 Route II: Synthesis of $ZnGa_2O_4$ in the Gas Phase

As an alternative material zinc gallate $ZnGa_2O_4$ is prepared by CVS and nitrided in second step. With E_g about 4.9 eV – 5 eV only photons with wavelengths shorter than 250 nm can be absorbed indicating an inefficient photoelectrochemical conversion. However, Chen et al. [2009] reported that $ZnGa_2O_4$ is the key intermediate in the solid-state reaction for formation of oxynitrides with a Zn/(Zn+Ga) ratio limited to 0.33. Since Zn and Ga are part of a very stable oxide spinel phase ($ZnGa_2O_4$) Zn loss during the nitridation is not as pronounced as in the case of separated oxides (Ga_2O_3-ZnO). The elemental distribution depends on diffusion rates of Ga and Zn atoms as a function of temperature. One of the main drawbacks using commercial powders is the formation of large particles up to 3 microns and with a wide distribution in size and shape, as shown by Adeli et al. [2016]. They reported those synthesis techniques as inefficient due to long nitridation times afterwards limited by use of ammonia. In this chapter $ZnGa_2O_4$ is synthesized directly via CVS at 300 mbar and 1200ºC in the same reactor. $Ga(acac)_3$ is combined with different organic Zn precursors, such as solid: $Zn(acac)_2$, $Zn(OAc)_2$ and $Zn(TMHD)_2$, but the best results are achieved with liquid DEZ added at the beginning of the reaction zone, as well as the Ga source. In this way it is possible to directly compare CVS Ga_2O_3-ZnO with $ZnGa_2O_4$. With an evaporation rate of $6.1 \cdot 10^{-7}$ mol/s, when the bubbler for DEZ is set to 0ºC and system pressure of 300 mbar, the desirable ratio of Ga:Zn = 2:1 in the material is reached. Synthesis is repeated four times and EDX confirms this ratio by comparing atomic percentages of Zn and Ga. For each synthesized powder at least three elemental mappings are observed and average values are calculated (Figure 4.59). The presence of aluminum is due to the sample holder. Pure cubic spinel $ZnGa_2O_4$ phase (*wt.%* = 100) is confirmed by Rietveld refinement of each XRD pattern (Figure 4.60) of synthesized sample. Crystallite size is 25.6(4) nm with low microstrain of 0.012(8) % and with a typical cubic crystal structure - space group Fd-3mS (227), where the lattice parameter is a = 8.337(1) Å. The specific surface area is 40 m^2/g and a theoretical density 6.06 g/cm^3. For non-porous material and spherical particles, the obtained particle size calculated from BET is around 24.5 nm. Figure 4.61 shows typical adsorption/desorption isotherm of

$ZnGa_2O_4$ nanoparticles. According to IUPAC classification sorption isotherm is of type II and typically obtained for non-porous adsorbent (powder) and an unrestricted monolayer-multilayer adsorption occurs described by Lowell et al. [2004]. The non-existence of a hysteresis loop on adsorption-desorption isotherm, which is in general related to pore size distribution, indicates narrow particle size distribution with regular shape.

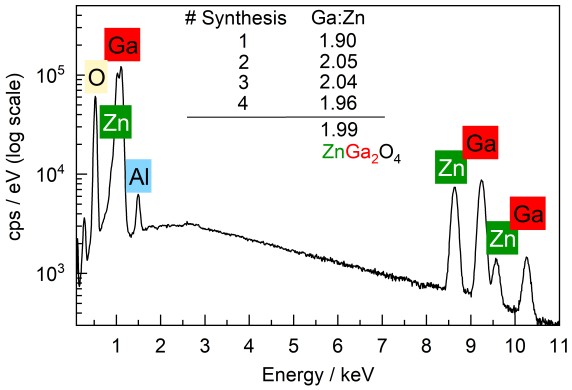

Fig. 4.59: Elemental mappings for $ZnGa_2O_4$ indicate desirable ratio of Ga:Zn = 2:1 achieved during the synthesis

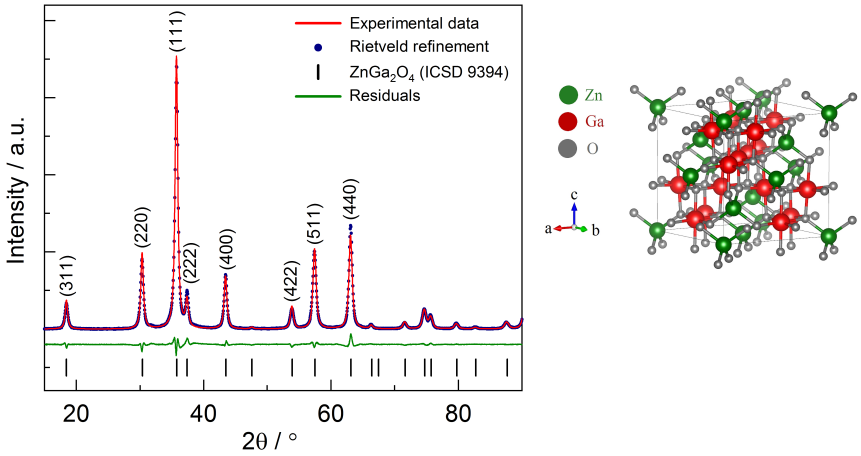

Fig. 4.60: XRD pattern of the $ZnGa_2O_4$ made by CVS (1200ºC and 300 mbar) fitted by Rietveld refinement using MAUD. Compared with $ZnGa_2O_4$ (ICSD #9394) reference as initial study model. Unit cell is presented using visualization software VESTA

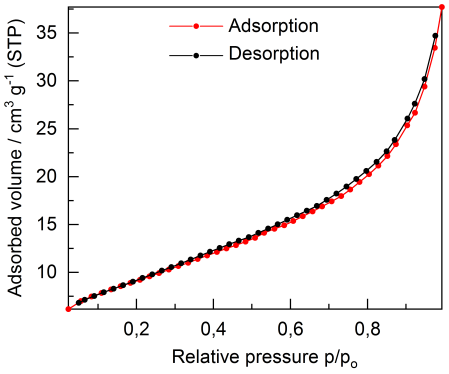

Fig. 4.61: Adsorption-desorption isotherm of type II (IUPAC) of CVS $ZnGa_2O_4$ (1200 ºC, 300 mbar) suggesting non-porous particles with a narrow particle size distribution

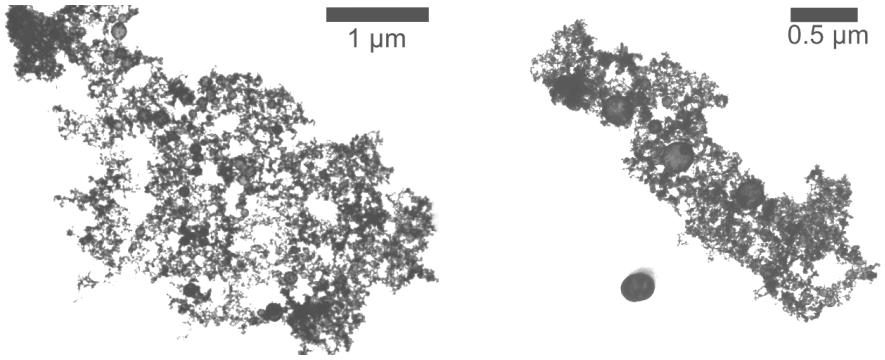

Fig. 4.62: Agglomerated $ZnGa_2O_4$ nanoparticles observed in STEM mode (JEOL-SEM 7500F)

As part of the sample preparation on a TEM grid, particles are previously dispersed into semiconductor grade methanol and tend to form soft agglomerates visible in Figure 4.62, which is easy to break using ultrasonic bath. Beside nanosized particles only a few spots indicate the presence of bigger nanospheres, which occasionally grow to microsize larger than 100 nm. To explain this features and their morphology STEM/EDS on HRTEM is used. In Figure 4.63A those visible-through 'bubble-like' spheres are hollow spheres based on the *Kirkendall effect* and EDS shows it is clearly ZnO. In general, DEZ decomposes already at 36ºC in oxygen-free environment before it reaches the reaction zone and mixes with Ga species and oxygen. The surface of the metallic Zn particles is oxidized and Zn/ZnO - core/shell particles are

formed. The self-diffusion coefficient of Zn^{2+} ions is higher than for O^{2-} ions in the ZnO shell [Raidongia et al. 2008] and this unbalanced diffusion flux causes the formation of vacancies. These vacancies migrate and merge into larger voids located at the interface core/shell, as previously explained by Mel et al. [2015] and schematically presented in Figure 4.64. If the core is completely consumed particles become fully hollow or just partially, as presented in the Figure 4.63B for ZnO. The thickness of the ZnO shell depends on the ratio of Zn outer diffusion rate to the opposite flow rate of vacancies, which is a function of the reaction zone length and process parameters. On standard parameters the thickness of the ZnO shell is about 7 to 10 nm (Fig. 4.64E). Previously, Schilling et al. [2013] made small hollow nanospheres with average diameter of 50-100 nm via CVS. However, the scope of this work is not the synthesis of hollow nanospheres. During the nitridation process by

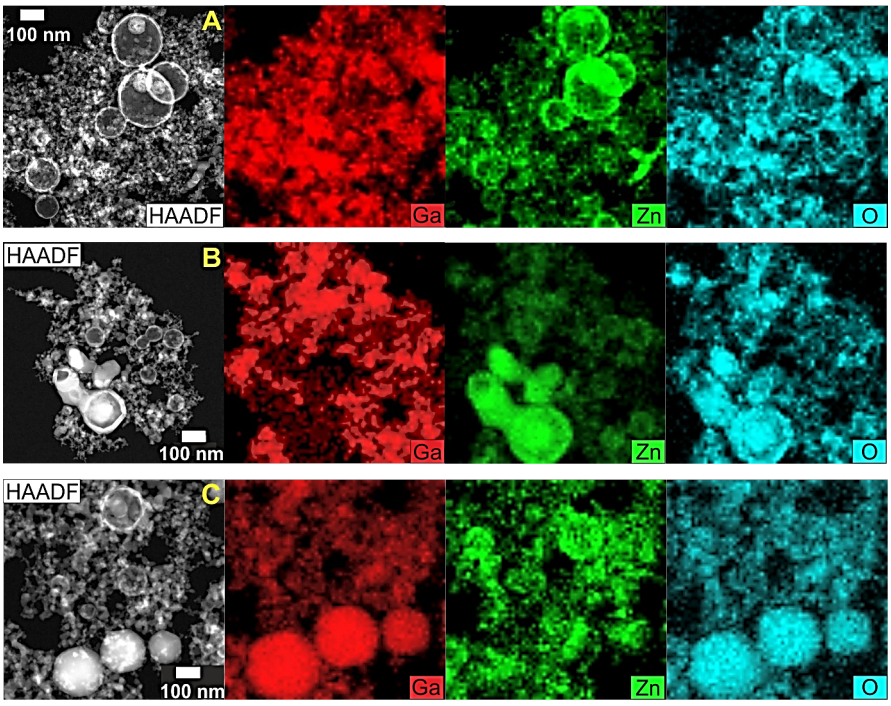

Fig. 4.63: EDS analysis using HRTEM **A** – hollow ZnO nanospheres from 30 – 150 nm, **B** – partially consumed Zn metallic core due to Kirkendall effect (not fully hollow ZnO particles), **C** – solid Ga_2O_3 spheres with sizes from 100 – 200 nm

using ammonia either solid ZnO particles or these hollow spheres of ZnO will be reduced to metallic Zn and finally evaporate. This particular morphology is interesting from the point of view of nanoparticle synthesis, but not for POWS. In Figure 4.63C solid Ga_2O_3 particles are formed. Excess amount of Zn and Ga form separate Ga_2O_3 and ZnO in minority due to fluctuation in evaporation of precursors. No Ga_2O_3 hollow spheres are obtained, while self-diffusion coefficient for Ga^{3+} is much lower compared to Zn^{2+} ions.

$ZnGa_2O_4$ crystallizes in a face centered cubic (fcc) crystal structure and the particles have spherical to slightly ellipsoidal shape, the same as previously shown for other samples made by CVS. High nanoparticle crystallinity reveals the absence of

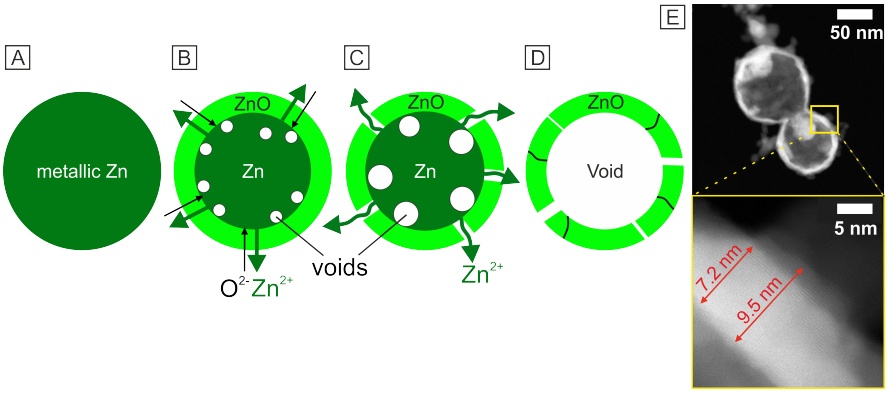

Fig. 4.64: Schematic drawing of Kirkendall effect for CVS nanoparticles. **A** – metallic zinc formed by pyrolysis of DEZ, **B** – Zn particle oxidizes on the surface, diffusion rate of Zn^{2+} is faster than that for O^{2-} across the ZnO shell and formation of voids, **C** – partially consumed metallic Zn core and formation of larger voids and cracks in the shell, **D/E** – Hollow ZnO with shell thickness of about 7 – 10 nm. Adjusted from [Schilling et al. 2013]

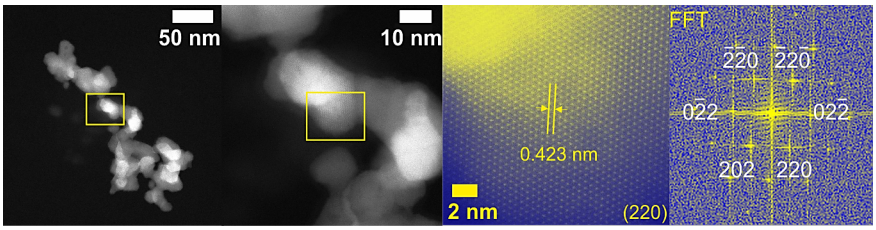

Fig. 4.65: TEM and HRTEM images of highly crystalline $ZnGa_2O_4$ nanoparticles with corresponding FFT pattern. Insets are the lattice distance measurements of (220) plane

1/2D structural defects validating the low microstrain information extracted by Rietveld refinement with lattice parameters a = 8.337 Å typical for spinel $ZnGa_2O_4$. With an optimal loading of co-catalyst (0.1 wt.% CrO_x and 0.5 wt.% Rh) $ZnGa_2O_4$ exhibit fairly good photocatalytic activity of 2.32 mmol g_{cat}^{-1} h^{-1} of H_2 and 0.95 mmol g_{cat}^{-1} h^{-1} of O_2. The electronic structure of the spinel is in general unfavorable for photocatalytic activity. However, the presence of the hollow spheres and larger solid particles, such as Ga_2O_3, may have some significant impact on photocatalytic activity of these materials, which needs to be further investigated.

4.3.2.1 Thermal Nitridation of $ZnGa_2O_4$ Particles using NH_3

Complete conversion to $(Ga_{1-x}Zn_x)(N_{1-x}O_x)$ when using bulk starting materials needs a nitridation temperature of 850ºC, while for nanoparticles it could be lower than 750ºC and even 650ºC if ZnO is added to starting $ZnGa_2O_4$, as suggested by [Lee et al. 2016]. The decomposition rate of NH_3 is faster at higher temperatures. Therefore, higher concentration of nitrogen-contained species are released into reaction and transformation into wurtzite type oxynitride can take place in order of minutes [Adeli and Taghipour 2016]. Diffusion of nitrogen occurs more rapidly over surface and along grain boundaries than through the interior of the crystallites [Fisher et al. 1951]. Using $ZnGa_2O_4$, made by solid-state reaction between ZnO and Ga_2O_3, nitridation at high temperatures leads to the formation of bigger particles. During POWS the crystallites embedded in the center of the clusters are not exposed to the incident photons and the photogenerated charges are trapped in the grain boundaries. Nanoparticles should be used to overcome this problem. Tongying et al. [2017] nitrided a mixture of nanoscaled ZnO-$ZnGa_2O_4$ (max. ratio of Ga : Zn = 1.1 : 1) for 10 h in a temperature range from 650ºC to 900ºC and reported significant Zn loss, again due to free ZnO in the mixture.

Pure CVS spinel $ZnGa_2O_4$ is nitrided for 5 h in order to compare it with oxynitrides previously made by nitridation of CVS ZnO-Ga_2O_3 mixture. The conventional way of nitridation using thermal decomposition of NH_3 is used in a temperature range from 450ºC to 850ºC for 5 h and the XRD results are presented in Figure

4.66. At 450ºC the structure remains almost unchanged and O is not substituted with N, while the Zn/(Zn+Ga) ratio is still 0.33, which is similar compared to the initial value of 0.35. Neither the specific surface area decreases nor the crystallite size increases significantly. The same is observed for the sample at 550ºC. Incomplete phase transformation from spinel $ZnGa_2O_4$ to wurtzite $(Ga_{1-x}Zn_x)(N_{1-x}O_x)$ occurs above 650ºC. Full phase transformation occurs at temperature of 750ºC and above. At the standard temperature of 850ºC crystallite size is 30 nm, which is slightly increased compared to the initial 25 nm for the spinel structure. The specific surface area decreases from 40 m^2/g to 16 m^2/g and it is very similar with 18 m^2/g for oxynitride made from Ga_2O_3-ZnO at the same conditions. In addition, it is not a surprise that the Zn content is reduced, but with a ratio of Zn/(Zn+Ga) of 0.15 the Zn content is not significantly lower than for $ZnGa_2O_4$ used as a starting material compared to the sample nitrided from mixture of Ga_2O_3-ZnO with ratio of only 0.03. The ratio of N/(N+O) is 0.32 obtained by EDS and the chemical formula of oxynitride for this sample can be presented as $(Ga_{0.85}Zn_{0.15})(N_{0.32}O_{0.68})$. The advantage of this oxynitride is even more pronounced when considered that the band gap is direct with an energy of 2.75 eV.

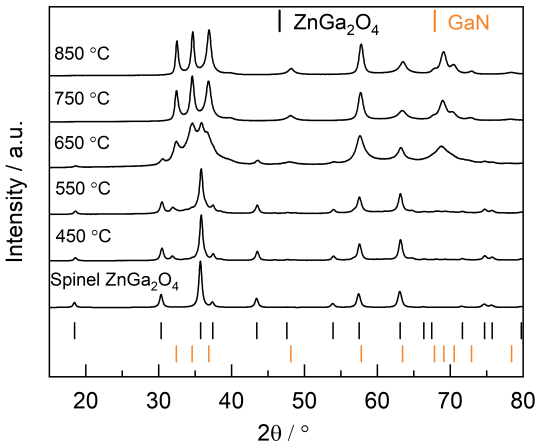

Fig. 4.66: Thermal nitridation under NH_3 for 5 h shows full phase transformation from spinel to wurtzite phase from 750ºC

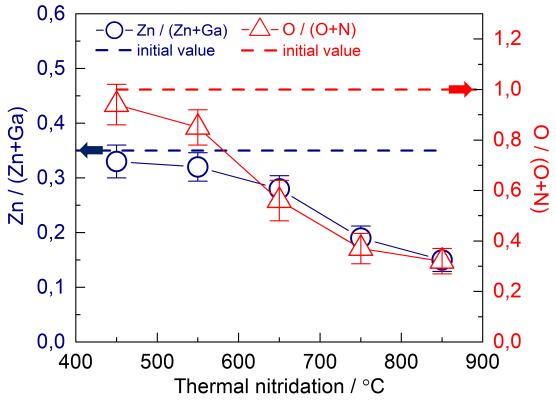

Fig. 4.67: Influence of nitridation temperature (t = 5 h) on Zn/(Zn+Ga) and O/(O+N) ratios obtained by EDS

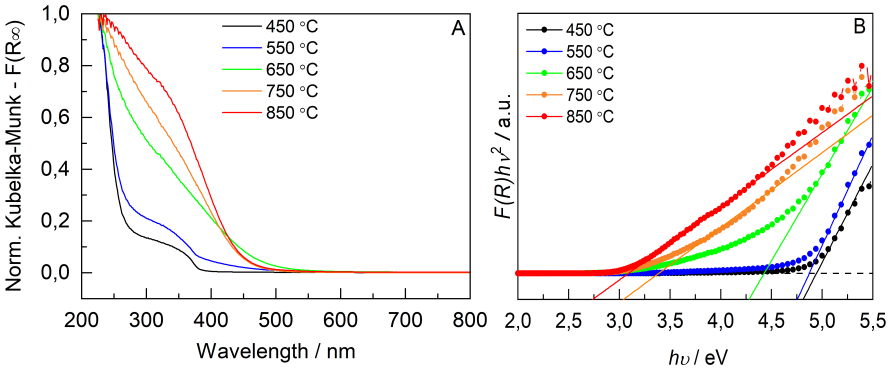

Fig. 4.68: A – Reflectance spectra presented by Kubelka-Munk equation and **B** – Tauc plot functions indicating direct band gap which decreases from 4.7 eV to 2.75 eV with increasing the nitridation temperature from 450ºC to 850ºC

Since the photocatalytic activity of the samples is compared in UV region this area is of great importance in the PL spectra. In Figure 4.69 for samples nitrided at low temperatures (450 – 650 ºC) peak at 375 nm is attributed to the recombination of the free excitons, which is not observed for the starting $ZnGa_2O_4$. Two low emission peaks at 420 and 440 nm appear when the spinel $ZnGa_2O_4$ is nitrided at low temperatures of 450ºC and 550ºC. Liu [2009] and Wani [2017] found that this emission may be due to self-activation center of Ga-O octahedral group, where transfer of

charge occurs between neighboring Ga^{3+} ions. The high intensity of the green emission around 526 nm is due to defects in the crystal structure and the intensity increases with higher concentration of the defects. At 550ºC the intensity of the emission peak is slightly higher confirming higher Zn loss (increase of vacancy type defects) during the nitridation compared to 450ºC. The sample nitrided at 650ºC contains spinel $ZnGa_2O_4$ and $(Ga_{1-x}Zn_x)(N_{1-x}O_x)$ and shows green and yellow luminescence, which is, as reported by Neugebauer et al. [1996], attributed to Ga vacancies (V_{Ga}) or could be due to other defects during substitution of O with N and Ga with Zn. The most interesting sample is obtained at 850ºC – it does not exhibit luminescence in the UV region and shows the highest photocatalytic activity not only comparing these samples, but among all the nitrided samples in this work. The red luminescence with maximum at 700 nm is observed for sample at 750ºC, but not for the sample at 850ºC. Again, when compared with oxynitride made at the same conditions, but from mixture of Ga_2O_3-ZnO this sample has significantly lower defect density. At wavelengths of 405 nm and 810 nm the originate from laser.

The elemental distribution observed by EDS shows a dominant presence of Ga on the surface of the particles, where Zn evaporates easier than inside of the particles (Fig. 4.70). Therefore, the trapped zinc is the reason of the higher Zn/(Zn+Ga) ratio when using spinel phase as the starting material. HRTEM shows highly crystalline

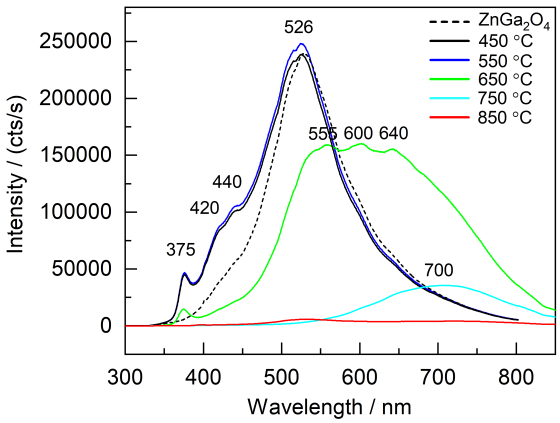

Region	Type/Color	Wavelength (nm)
UV	UV-C	100 - 280
UV	UV-B	280 - 315
UV	UV-A	315 - 400
Visible	Purple	400 - 435
Visible	Blue	435 - 480
Visible	Cyan	480 - 490
Visible	Blue green	490 - 500
Visible	Green	500 - 560
Visible	Yellow green	560 - 580
Visible	Yellow	580 - 595
Visible	Orange	595 - 610
Visible	Red	610 - 750
Visible	Red violet	750 - 800

Fig. 4.69: Photoluminescence spectra (STP – 1 atm and 25°C) of CVS samples: $ZnGa_2O_4$ and $(Ga_{1-x}Zn_x)(N_{1-x}O_x)$ nitrided for 5 h in temperature range from 450ºC to 850ºC

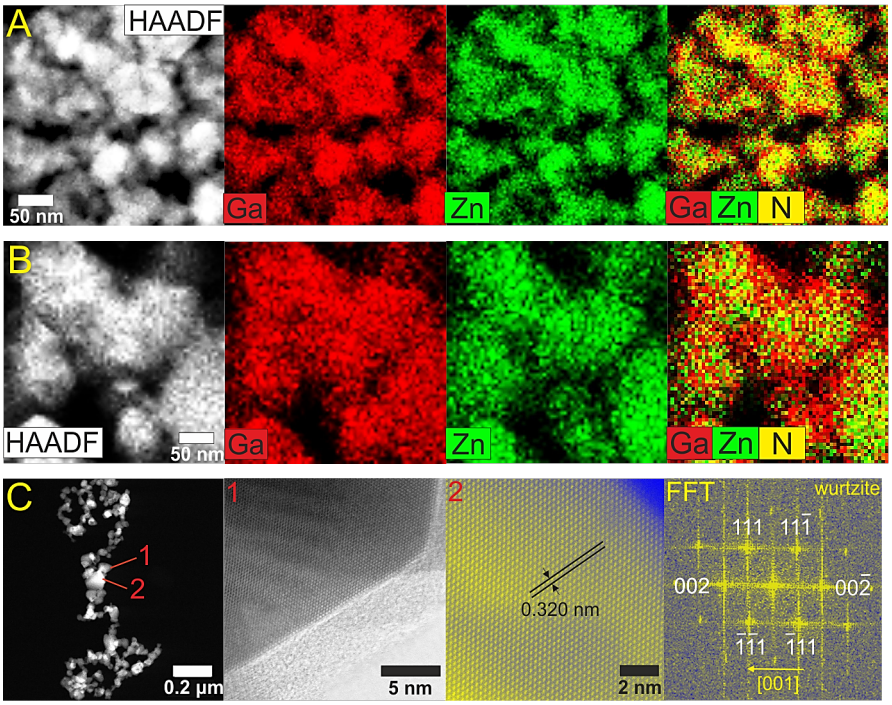

Fig. 4.70: A/B – EDS analysis of $(Ga_{0.85}Zn_{0.15})(N_{0.32}O_{0.68})$ with Zn deficiency on the surface compared to inner of the particles and **C** – HRTEM images showing highly crystalline particles and corresponding FFT pattern

material with no visible disorder of the atoms in the crystal structure. This is in good agreement with the PL results confirming very low defect density. Also the surface terminations of the particles look very crystalline and Fourier transformation pattern confirms the wurtzite phase typical for the oxynitrides.

With a photocatalytic activity of 4.4 mmol g_{cat}^{-1} h^{-1} for H_2 and 3.4 mmol g_{cat}^{-1} h^{-1} for O_2 it is a first time that nitrided sample (t = 5 h; T = 850°C) exhibit higher activity than the parent oxide, which is here $ZnGa_2O_4$. The comparison with other samples is presented in the Figure 4.71. Having two nitrided samples with almost the same specific surface areas it is clear that the determining factor for the high activity is the Zn content and the defect density. With 6.78 mmol g_{cat}^{-1} h^{-1} for H_2 and 0.62 mmol g_{cat}^{-1} h^{-1} for CO_2 this sample is even better for methanol reforming than the sample nitrided at the same conditions, but from Ga_2O_3-ZnO with only 1.76 mmol

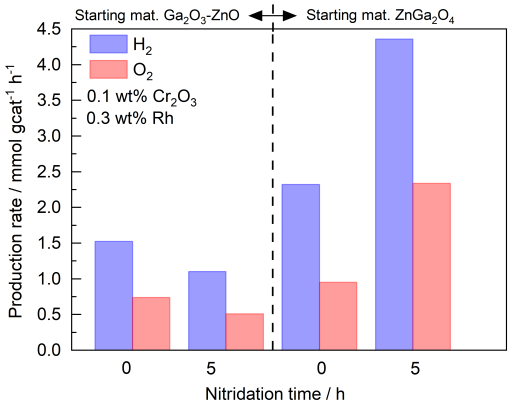

Fig. 4.71: Comparison of POWS activity of Ga-Zn-oxynitrides (nitrided for 5 h at 850 °C) with parent Ga_2O_3-ZnO mixture and $ZnGa_2O_4$ as starting materials. All results are recalculated per gram of catalyst and optimal loading for nitrided samples is considered (0.1 wt.% Cr_2O_3 and 0.3 wt.% Rh)

g_{cat}^{-1} h^{-1} for H_2 and 0.09 mmol g_{cat}^{-1} h^{-1} for CO_2, which is about four time less. All the parameters by now show superiority of the nitrided sample made from the $ZnGa_2O_4$ as starting material.

4.3.2.2 Microwave Assisted Plasma Nitridation of $ZnGa_2O_4$ using NH_3 or N_2 as Reactive Gases

One of the future challenges is to produce samples with higher Zn content by changing the conventional method of nitridation. In this chapter the reactive gases are decomposed previously by a microwave plasma and their influence on the final samples is investigated. In thermal nitridation with NH_3 the nitride coatings are often formed on the surface of the particles which limits the further diffusion of N into the particles affecting the nitridation times, which takes several hours. Microwaves provide a reactive plasma which reacts with the surface of the sample making it rougher. The diffusion rate of N species into the sample is dependent on the surface area of the sample, the gas flux through the quartz tube and length of the microwave plasma reactor. Aguirre et al. [2010] used NH_3 as reaction gas to obtain strontium-titanate oxynitrides and reported the formation of nitrogen rich islands in the near

surface area of the sample when nitrided with low NH_3 flux less than 100 sccm. With higher fluxes oxygen is removed faster from the surface and N species diffuse into the bulk of the material, followed by a higher concentration of stacking faults. Houmes and Loye [1996] used an H_2/N_2 plasma to disrupt Al-O bonds of the Al_2O_3 material to produce AlN. It is much easier to decompose the NH_3 gas than N_2 where the chemical bond is very strong and by conventional thermal technique it demands high temperatures above 1727ºC at atmospheric pressure. Recently, a pure N_2-plasma was employed by Sung et al. [2017] to obtain non-agglomerated AlN powders from Al particles in temperature range from 700ºC to 800ºC. The common challenge is to reduce the nitridation temperature and time. The disadvantage of applying NH_3 is the highly reducing atmosphere due to H_2 generated as a byproduct during gas decomposition, which is already known as a strong reduction agent for $ZnO/ZnGa_2O_4$ to metallic Zn. Applying pure N_2 is clearly advantageous and the formation of active nitrogen species of the afterglow is controlled by variation of the system pressure, the flow rate and applied power of the reactor. Various excited states of N_2, N_2^+ and atomic N species are generated in N_2 plasma [Sakakura et al. 2019]. $ZnGa_2O_4$ sample is nitrided using assisted microwave plasma process with the same nitridation time of 5 h as for conventional (thermal) nitridation method. The temperature is varied from 450ºC to 850ºC analogous to the previous chapter when the same material was nitrided only thermally without employing the microwave plasma for comparison. Still, using nanoparticles with a size of 25 nm the process is very challenging due to a couple of reasons. First, the microwave plasma reactor used in this work is very unstable at atmospheric pressure and demands vacuum conditions (50 mbar). It also demands certain flow of the gases, like mixture of NH_3 or N_2 with Ar (150 sccm both), which is also reported by Dias et al. [2016]. One of the main drawback is the use of the small $ZnGa_2O_4$ nanoparticles with a size of 25 nm placed in a MACOR boat inside a quartz tube. Setting the pressure to 50 mbar must be performed very carefully with a slow decreasing rate to avoid that the nanoparticles fly away into the pump. One of the main problems is a generation of the highly charged nanoparticles in the plasma afterglow, which then simply fly away. Positioning the plasma reactor is also one of the crucial points and if it is

placed too far from the hot wall reactor the decomposed gas species will recombine forming N_2 molecules again. The solution is provided in the form of pellets made by dry pressing of $ZnGa_2O_4$ nanoparticles, which is a different approach than for the powders nitrided only thermally (Fig. 4.72).

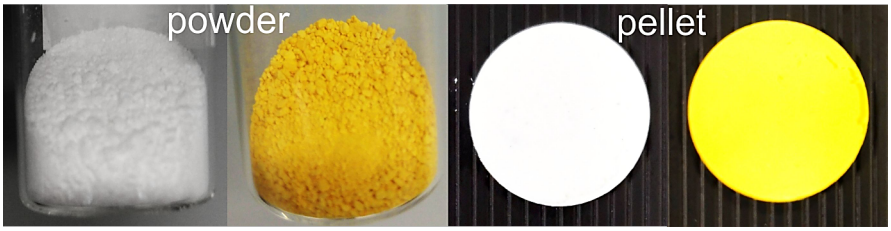

Fig. 4.72: $ZnGa_2O_4$ powder nitrided only thermally and $ZnGa_2O_4$ pellet nitrided thermally with assisted microwave plasma reactor. Both samples are nitrided for 5 h and color changes from pure white into pure yellow.

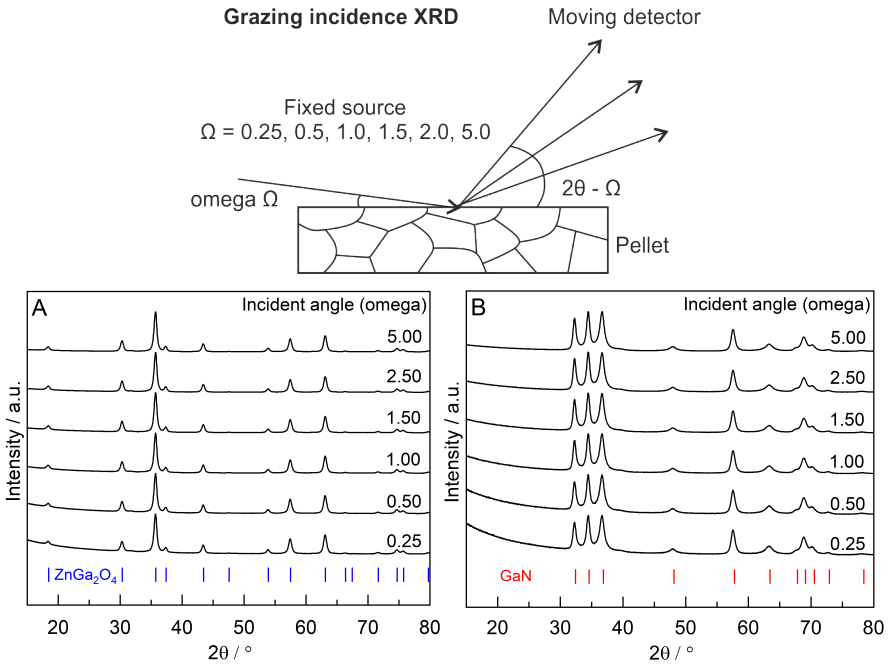

Fig. 4.73: GIXRD with different fixed incident angles (omega) from 0.25 to 5.0 for **A** – spinel $ZnGa_2O_4$ and **B** – $(Ga_{1-x}Zn_x)(N_{1-x}O_x)$ nitrided thermally with microwave assisted plasma at 850ºC for 5 h to investigate the penetration depth of reactive nitrogen species showing very good homogeneity of the nitridation process using pellets

As presented in Figure 4.73A-B grazing incident XRD is performed to analyze the penetration depth of the nitrogen species into the pellet for the sample nitrided at 850ºC either with NH_3 or N_2. This is the representative sample for comparison to other samples in this work. By changing the fixed source described by the omega angle Ω from 0.25 to 5.0 the X-rays are penetrating deeper into the pellet, while the detector is moveable in range of $2\theta = 15^{o} - 80^{o}$. The $ZnGa_2O_4$ pellet is in general exposed to reactive gas (NH_3 or N_2), previously decomposed by microwave plasma reactor and all the examined layers show wurtzite structure typical for the oxynitride. This discovered method is clearly suitable for nitridation of the pellets. This

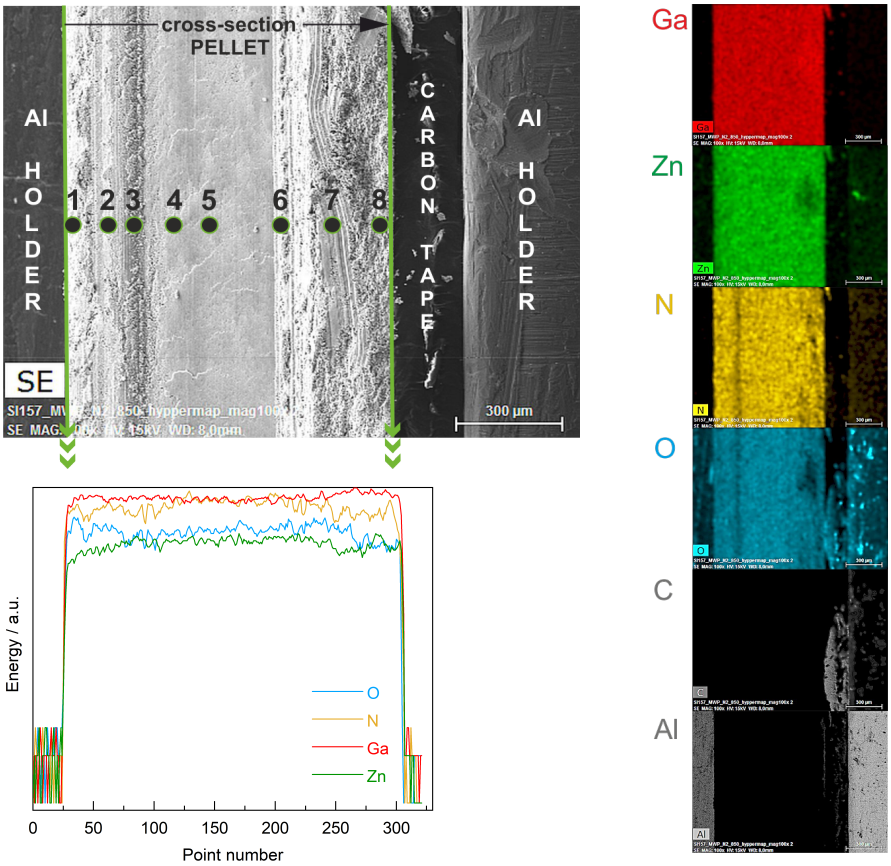

Fig. 4.74: Uniform elemental distribution in the cross-section of the nitrided pellet with thickness of 650 µm, where Ga and N presence is more dominant than Zn and O

fact is underlined by line and point scan in EDS (points 1-8) from the cross-section of the pellet (Fig. 4.74), which show very little local deviations in the chemical composition.

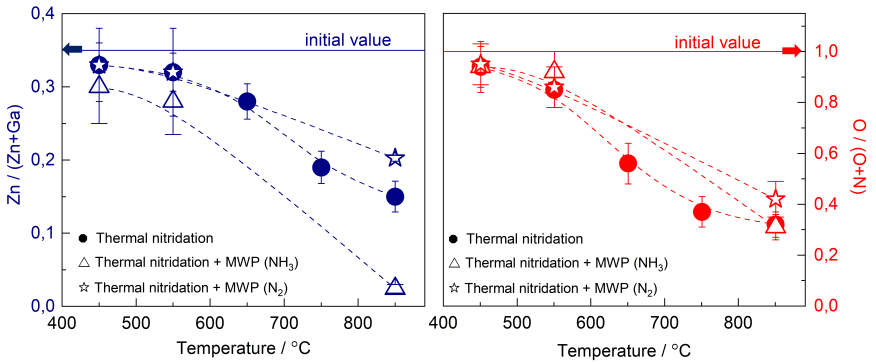

Fig. 4.75: Contents of Zn/(Zn+Ga) and O/(O+N) on different temperatures after nitridation of $ZnGa_2O_4$ powder and pellets thermally with NH_3 (circles) and with assisted microwave plasma using NH_3 (triangles) and N_2 (stars). (B-splines are intended as a guide to the eye)

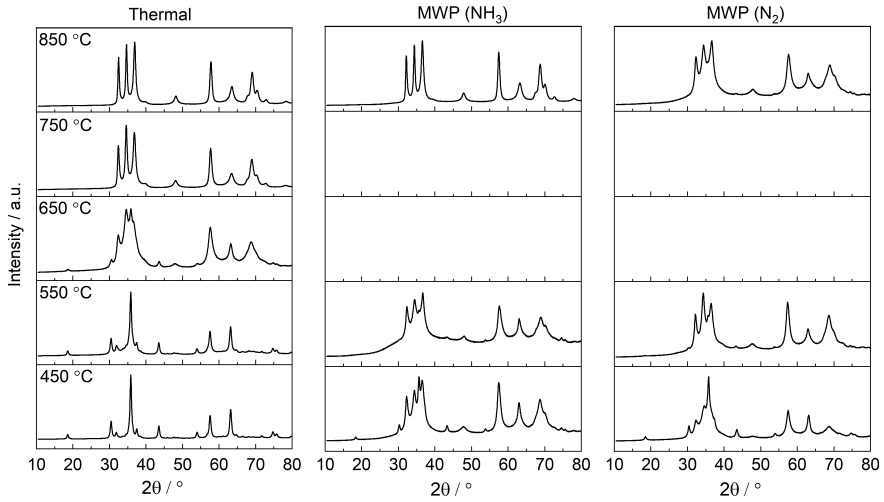

Fig. 4.76: $ZnGa_2O_4$ powder nitrided thermally (NH_3) and pellets nitrided thermally with assisted microwave plasma – MWP (NH_3/N_2) cause significant differences in crystal structures. MWP shows advantage over conventional thermal nitridation with early formation of wurtzite structure typical for oxynitrides on lower temperatures, as displayed in X-ray diffractograms

Nitridation with N_2 and NH_3 is essentially the same, except that the amount of Zn is further decreased when NH_3 is used due to strong reductive atmosphere formed by its pre-decomposition. Ratios of Zn(Zn+Ga) and O/(O+N) are presented in Fig. 4.75 and in Table 4.7. This study systematically provides the data for the new technological solutions. The key research question in this chapter was whether the microwave assisted plasma process is better than the conventional thermal method. Thermal nitridation is not efficient on lower temperatures and the desired wurtzite structure is not obtained (Fig. 4.76). In general, a temperature of 450ºC is too low for any of the shown processes, but in case of nitridation with assistance of MWP using NH_3 the XRD pattern shows early transformation from spinel to the wurtzite phase. However, a major problem with this kind of nitridation is the generation of a very aggressive atmosphere when NH_3 is decomposed by MWP. The higher concentration of H_2 leads to even faster loss of Zn species. Comparing samples nitrided thermally and with MWP (NH_3) at standard temperature of 850ºC the Zn/(Zn+Ga) ratios are 0.15 and 0.02, respectively. The samples are not nitrided at 650ºC and 750ºC using MWP, since the targeted temperatures were lower temperatures in order to observe any advantages of the process, as well at 850ºC for comparison with

Table 4.7. Phase transformation of the spinel structure as a function of nitridation method

NM	*T*	*Zn/(Zn+Ga)*	*O/(O+N)*	*CF*	*CS*	Color
/	ºC	/	/	/	/	/
Initial	0	0.35	1.00	$ZnGa_2O_4$	Spinel	
Ther.	450	0.33	0.94	$(Ga_{0.51}Zn_{0.49})(N_{0.06}O_{0.94})$	Spinel	
Ther.	550	0.32	0.85	$(Ga_{0.53}Zn_{0.47})(N_{0.15}O_{0.82})$	Spinel	
Ther.	650	0.29	0.57	$(Ga_{0.59}Zn_{0.41})(N_{0.25}O_{0.75})$	Transition	
Ther.	750	0.19	0.38	$(Ga_{0.77}Zn_{0.23})(N_{0.39}O_{0.61})$	Wurtzite	
Ther.	850	0.15	0.33	$(Ga_{0.82}Zn_{0.18})(N_{0.51}O_{0.49})$	Wurtzite	
NH_3	450	0.30	0.92	$(Ga_{0.57}Zn_{0.43})(N_{0.09}O_{0.91})$	Transition	
NH_3	550	0.28	0.90	$(Ga_{0.61}Zn_{0.39})(N_{0.11}O_{0.89})$	Wurtzite	
NH_3	850	0.02	0.31	$(Ga_{0.98}Zn_{0.02})(N_{0.55}O_{0.45})$	Wurtzite	
N_2	450	0.33	0.95	$(Ga_{0.51}Zn_{0.49})(N_{0.05}O_{0.95})$	Transition	
N_2	550	0.32	0.86	$(Ga_{0.53}Zn_{0.47})(N_{0.16}O_{0.84})$	Wurtzite	
N_2	850	0.20	0.39	$(Ga_{0.65}Zn_{0.25})(N_{0.64}O_{0.36})$	Wurtzite	

NM nitridation method *CF* chemical formula
T temperature *CS* crystal structure type

other samples. With increasing temperature, the final color of the powder changes into pure yellow. Depending on the atmosphere created in the process low temperature samples are yellow greyish with more pronounced grey color when the concentration of H_2 is increased. Finally, nitridation with MWP using N_2 shows the formation of the wurtzite phase already at 550ºC. At 850ºC the Zn/(Zn+Ga) ratio is high with value of 0.20. One problem of this methodology is pelleting the powder, which causes co-sintering of the particles during the process. For POWS experiments pellets have to be grinded for longer time to regenerate a powder. When the particles are co-sintered sintering necks are formed and it is very hard to break those hard agglomerates, thus minimizing the surface area of the particles where the co-catalyst can later be attached. As a part of the future work it is necessary to improve the nitridaton process using MWP, so that the charging of the powder is avoided or to make it more stable at atmospheric pressure.

From Figure 4.77 it can be concluded that MWP (NH_3/N_2) samples produced at 550ºC and standard 850ºC have similar band gap energies of about 2.8 eV like the oxynitride nitrided just thermally at 750ºC or 850ºC (see Fig. 4.68). Common for all these samples is that they are nitrided from the same CVS $ZnGa_2O_4$ powder for 5 h and that the wurtzite phase is formed. Still, minor differences are observed, but the key aspect is that direct band gap energies are observed, unlike for the samples

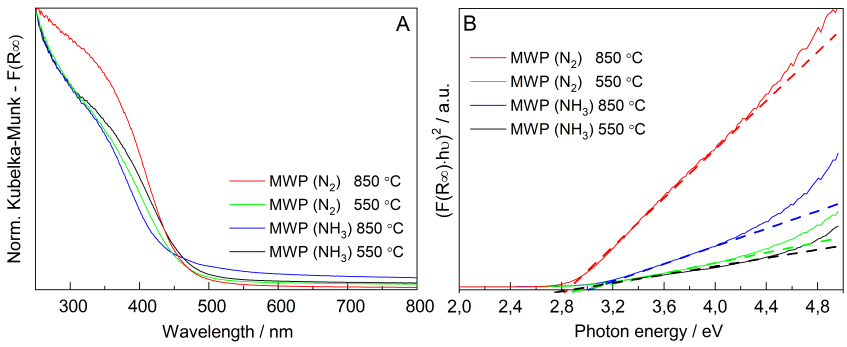

Fig. 4.77: A – Absorbance spectra presented by Kubelka-Munk equation and **B** – Tauc plot functions indicating direct band gap of 2.8 – 2.9 eV for samples nitrided with MWP using N_2 and NH_3 as reaction gases

nitrided from mixture of Ga_2O_3-ZnO (see Fig. 4.45). As presented in Figure 4.78 POWS testing is carried out to compare the activities of the samples. The activity of thermally nitrided $ZnGa_2O_4$ is still higher than for samples when MWP is used. This may be explained by the fact that the particles are co-sintered and hard agglomerates are formed during nitridation of pellets, therefore, showing lower activities. Comparing MWP samples internally the low temperature of 550ºC is advantegous over 850ºC whether the NH_3 or N_2 is used, but only when the pellets are nitrided. At higher temperatures the sintering effect is more pronounced and thus unfavorable. On the other hand, if the powder could be nitrided directly using MWP it is possible that due to very high crystallinity of the powder, as well the high Zn content these samples would show much higher activities. Using NH_3 the phase transformation to wurtzite structure during nitridation is faster than for N_2 and suitable at lower nitridation temperatures. As a general conclusion, all observed results using NH_3 are higher compared to samples nitrided from mixture of Ga_2O_3-ZnO. This confirms the benefits of using spinel $ZnGa_2O_4$ as a starting material.

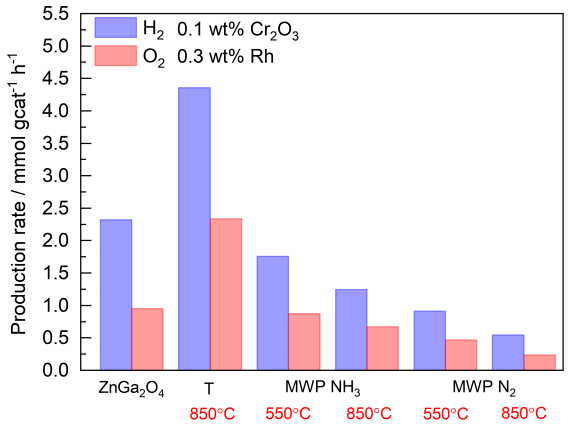

Fig. 4.78: Comparison of POWS activity of Ga-Zn-oxynitrides made from $ZnGa_2O_4$ using thermal or microwave plasma assisted nitridation with NH_3 or N_2. All results are recalculated per gram of catalyst and optimal loading for nitrided samples is considered (0.1 wt.% Cr_2O_3 and 0.3 wt.% Rh)

4.4 Direct Nitridation in CVS

As previously seen, each synthesis route has its advantages and drawbacks. Due to a narrow process window for the solid precursor route and further nitridation steps certain material properties are improved at the disadvantage of others. The possibility of the modular construction of CVS system enables use of numerous precursor materials. The decomposition kinetics of these precursors (reactants), their reaction enthalpies (contribute to the heat balance) and delivery method, among other factors, influence the time-temperature profile of the process [Winterer 2002]. With variation of precursor material, the composition, properties and yield of the final powders can be changed. The evaporation of TEG is investigated previously by Baev and Sokolovskii [1994] with Antoine parameters a = 8.08 and b = 2162 K. Standard pressure for liquid precursors used in CVS is 20 mbar and below a bubbler temperature of 40ºC the process is stable (Fig. 4.79). If compared to evaporation of solid precursors (i.e. $Ga(acac)_3$) it is obvious that the process window of TEG is much larger and low pressures can be used. Therefore, it is much easier to adjust the parameters and target the desired powder properties.

TEG with a chemical formula $C_6H_{15}Ga$ does not contain oxygen and it is suitable for production of GaN directly via CVS. Analogously, [Ognjanovic 2019] used triethylaluminium (TEAL) to generate AlN nanoparticles via CVS. TEG is thermally

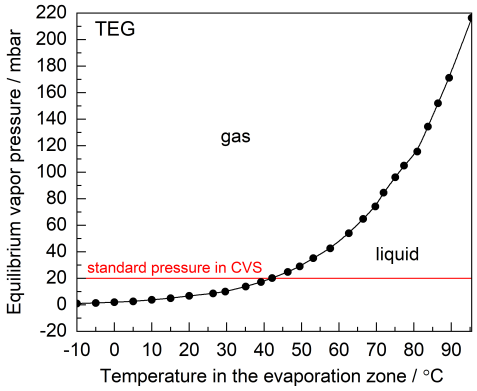

Fig. 4.79: Vapor pressure curve as the function of the temperature for TEG

decomposed forming Ga atoms and C_2H_4 and C_2H_5 as byproducts. GaN is chosen as a model to test the newly designed precursor delivery module – the inert gas box, as previously described in chapter 3.1.1. This chapter describes the proof of principle that GaN nanoparticles are directly synthesized via CVS. The synthesis of more complex structures like oxynitrides directly via CVS is possible, but technically more challenging and demands further modification of the CVS system.

GaN has a band gap about 3.4 eV with inadequate band edge positions and, therefore, photocatalytically not active. Two additional GaN powder were synthesized from $Ga(acac)_3$: first one in one step directly via CVS and second one in two steps starting from CVS Ga_2O_3 (Sample 5) and nitrided thermally for 5 h at 850ºC. These powders are compared to GaN powder made from TEG. All samples are scanned ten times in XRD at the same conditions as described in chapter 3.4.1 and averaged scans (diffractograms) are presented in Fig. 4.80. XRD patterns are not normalized, so that the differences in intensities are clearly visible. The Ga_2O_3 sample obtained

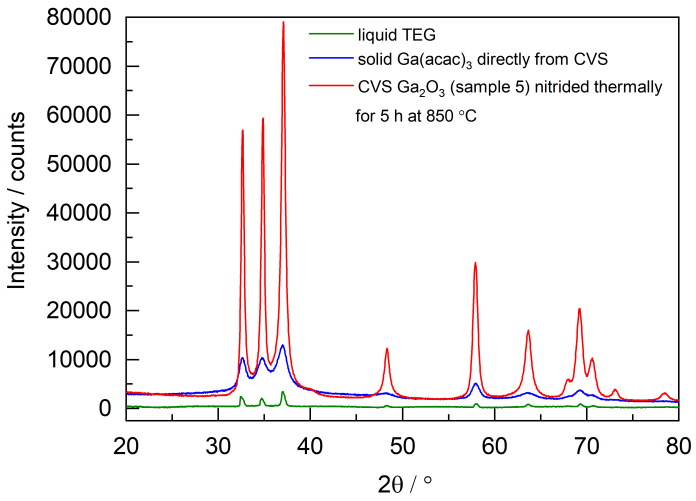

Fig. 4.80: Diffraction pattern reflections differ in intensity among the GaN powders obtained using different synthesis routes. GaN sample made directly via CVS from liquid TEG (green), GaN from solid $Ga(acac)_3$ made directly via CVS using NH_3 (blue) and nitrided CVS Ga_2O_3 (sample 5) in the second step for 5 h and at 850ºC (red). Compared separately with GaN (ICSD #54698) reference as initial studying parameters (data from Rietveld refinement is presented in Table 4.8)

Table 4.8. Phase transformation of the spinel structure as a function of nitridation method

P	*CS*	*MS*	*SSA*	*IF*	*TF*	*LP [a ; b ; c]*
/	nm	%	m^2/g	%	%	Å
$Ga(acac)_3$	33 ± 1.3	0.21 ± 0.005	20	0.43 ± 0.03	1.10 ± 0.08	3.201; - ; 5.201
$Ga(acac)_3$	8.3 ± 1.0	0.78 ± 0.098	102	1.70 ± 0.26	2.48 ± 0.11	3.195; - ; 5.205
TEG	2.8 ± 0.6	0.26 ± 0.014	160	0.94 ± 0.05	1.90 ± 0.11	3.191; - ; 5.190

P	Precursor type	*IF*	Twin fault probability
CS	crystallite size	*LP*	lattice parameters
MS	microstrain	*Red*	GaN from $Ga(acac)_3$
SSA	specific surface area		*nitrided $Ga_2O_{3(CVS)}$*
IF	intrinsic (stacking) fault probability	*Blue*	GaN_{CVS} from $Ga(acac)_3$
		Green	GaN_{CVS} from TEG

from CVS and additionally nitrided in the second step to GaN has the highest intensity and biggest crystallite size of 33 nm with corresponding specific surface area of 20 m^2/g. Since the particles are exposed to a temperature of 850ºC for 5 h they grow being partially sintered with a decrease of the surface area, which is a drawback of this method. For GaN made directly via CVS from solid $Ga(acac)_3$ at standard conditions at 300 mbar and 1200ºC the crystallite size is much lower – around 9 nm and specific surface area is 102 m^2/g. The color of the powder is greyish and as described before this precursor is not suitable for making GaN because it contains a lot of oxygen species released during its decomposition. However, it could be used for synthesis of oxynitrides, but difficult to control the composition and O:N ratio.

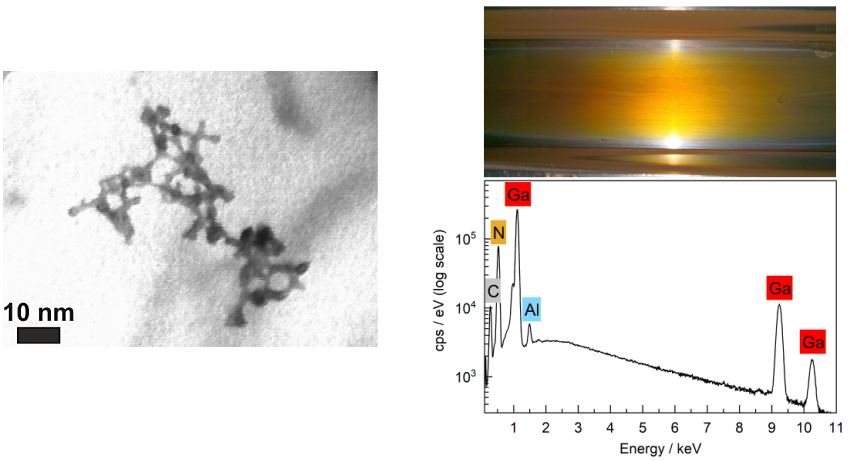

Fig. 4.81: GaN particles smaller than 5 nm detected in STEM (left) with EDX analysis confirming existence of GaN powder with typical yellow color as visible in the collector (right)

Hence, as ideal solution liquid TEG is used and GaN synthesized at 20 mbar and 1200ºC providing yellow powder and indicating successful test of the constructed inert gas box. As shown in chapter 4.1.2.1 synthesis at such a low pressure from solid $Ga(acac)_3$ is not possible. The crystallite size of GaN from TEG is around 3 nm with specific surface area of 160 m^2/g. The small particle size of the GaN powder made from TEG is confirmed by STEM (Fig. 4.81) even though it is very hard to obtain better image quality due to resolution limit of 1 nm at an acceleration voltage of 30 kV of the instrument.

5 Summary and Conclusions

Zinc-gallium oxynitride from CVS has the potential to be active for photocatalytic overall water splitting under visible light. This material system has little hazardous potential, and it is sufficiently stable in aqueous media, but has challenging material optimization problems. The physicochemical properties of nanoparticles and their application potential depend fundamentally on the particle characteristics such as: particle size and distribution, morphology, microstructure, local and crystal structure. CVS is used to tailor the properties of the nanoparticles and improve their photocatalytic activity.

The first part of this thesis is related to the optimization of the synthesis process by adjusting process parameters, such as: pressure, temperature and precursor partial pressure by synthesizing phase pure β-Ga_2O_3 from solid $Ga(acac)_3$ precursor. Pressures lower than 300 mbar reduce the residence times in the reaction zone significantly, which is related to a decrease in particle size due to insufficient time for particle growth. Below 50 mbar no powder could be collected via thermophoresis or no reaction occurs at all. Varying the temperature from 1000°C to 1500°C at a constant pressure of 300 mbar the crystallinity of the materials improves, while the surface area of the particle decreases with particle growth. By loading Rh/Cr_2O_3 cocatalysts all samples evolve H_2 and O_2 in the stoichiometric ratio of 2:1. The POWS activity is the highest for the optimum ratio of crystallinity and surface area observed for the β-Ga_2O_3 sample produced at 1200°C and 300 mbar via CVS.

Nanoscaled CVS β-Ga_2O_3 particles have almost spherical shape compared to the rod-like particles of microscaled commercial Ga_2O_3 powder (Chempur). Investigation of the local structure by (XANES/EXAFS) before and after the POWS experiments shows no significant structural changes indicating very good stability. The POWS activity of CVS Ga_2O_3 is increasing during the first 5 h compared to a decreasing activity for the commercial Ga_2O_3 sample (Chempur).

In this work β-Ga_2O_3 is doped with Mn, Rh and Fe. In CVS, it is possible to vary the microstructure and control the doping level even beyond the thermodynamic limit. The best progress is achieved by doping with 0.26 % of Mn^{2+} and it is the

second most active sample in this thesis after pure undoped Ga_2O_3. An increasing concentration of dopants increases the defect density and, therefore, lowers the photocatalytic activity.

Combining $Zn(TMHD)_2$ and $Ga(acac)_3$ it is challenging and hard to control the phase composition of the final powder and, therefore, liquid DEZ is used in combination with solid $Ga(acac)_3$ to overcome this problem. Mixtures of ZnO-Ga_2O_3 and $ZnGa_2O_4$ are generated in CVS and used as precursors to obtain the desired $(Ga_{1-x}Zn_x)(N_{1-x}O_x)$ by either thermal nitridation or in combination with microwave plasma reactor. The most active samples are nitrided for 5 h at 850°C. Oxynitrides from starting $ZnGa_2O_4$ show higher POWS activity than oxynitrides from ZnO-Ga_2O_3 due to better control of Zn volatilization during nitridation process. Applying microwave plasma reactor to pre-decompose NH_3 and N_2 reaction gases enables low temperature transformation from spinel $ZnGa_2O_4$ to wurtzite phase already at 550°C. However, pelleting the powder causes co-sintering of the particles, which leads to a decrease in specific surface area when the powder is regenerated by milling of pellets. Using N_2 as reaction gas this method has a great potential to prevent Zn loss during the nitridation and control the phase composition, which finally influences the band gap structure.

So far no POWS activity in the visible region has been observed due to increased defect density during the nitridation of the starting CVS powders, which leads to higher recombination of electrons and holes during POWS.

To generate GaN nanoparticles directly in CVS using NH_3 as reaction gas the liquid TEG is employed and delivered to the reactor using a specially constructed inert gas box. Very small nanoparticles with crystallite size below 3 nm and specific surface area of 160 m^2/g are generated at a temperature of 1200°C and pressure of 20 mbar. Therefore, the liquid precursor is advantageous compared to the solid precursor, and provides an opportunity to significantly change the process parameters and still obtain the desired material properties.

6 Research Recommendations

This thesis shows that CVS can be optimized and controlled to produce oxide, nitride and oxynitride nanoparticles of high quality for use in photocatalytic overall water splitting. Nevertheless, the knowledge obtained during this research can be utilized to further improve the CVS and nitridation processes. Some ideas and research recommendations are enlisted below.

By doping of β-Ga_2O_3 predominantly with Zn the crystallographic structure parameters and local structure around the dopant can be investigated by XAFS and solid-state NMR, as previously done by Djenadic et al. [2010] for ZnO doped with Co. This technique can be supported also by HRTEM/EDS/EELS spectroscopy for investigation of particle morphology, composition and distribution of elements. It can be also applied to Zn-Ga oxynitrides for a deeper understanding of influence of different nitridation techniques on the microstructure of the formed wurtzite phase. Maeda et al. [2006] investigated $(Ga_{1-x}Zn_x)(N_{1-x}O_x)$ by XAFS before and after photocatalytic reactions for different pH values of solutions to determine the degree of oxidation of Ga species on the surface as a result of the photooxidation by holes and/or by hydrolysis, but as well to determine the valence state of Cr and Rh co-catalysts. In this work only pure β-Ga_2O_3 without addition of co-catalyst is analyzed by XAFS to observe difference before and after POWS reaction by simple irradiation with UV light source in aqueous media.

Zn volatilization can also be suppressed by applying moisture-assisted nitridation process, as previously reported by Wang et al. [2016] and Jansen et al. [2018]. However, the degree of crystallinity is lower than for conventional nitridation technique at high temperatures. Therefore, the optimization of the microwave plasma assisted nitridation (presented in this work) and overcoming the technical limitations of using pressed pellets instead of powder could have a great potential. This can be achieved either by improving the stability of the plasma at atmospheric pressure or physically preventing charged particles to fly away. Nanoparticles can be trapped

on a membrane, which is permeable to gas molecules. Such a membrane is distinguished by high thermal, chemical and mechanical stability and could be implemented in the reaction tube for nitridation.

GaN nanoparticles are unstable in the ambient atmosphere and as reported by Ognjanovic [2019] for CVS AlN nanoparticles, when exposed to air they degrade very quickly to an amorphous oxide. Ali et al. [2012] in chemical vapor functionalization covered the surface of the nanoparticles with a capping agent to hinder the oxidation. Capping agents would be further decomposed during the nitridation process. In addition, a thermophoretic collector for continuous nanoparticle collection under inert conditions described by Ognjanovic [2019] should be used.

The newly constructed precursor delivery unit (inert gas box) offers plenty of opportunities for synthesis of the complex structures. Using more than two precursors, such as: TEAL, DEZ and TEG by varying the precursor delivery sequences core-shell ZnO-Al_2O_3 nanoparticles can be produced and mixed with Ga_2O_3. The Al_2O_3 shell thickness can be adjusted by precise control of the process parameters which hinders the volatilization of the Zn species during the nitridation.

Zn_3N_2 and GaN can be obtained as starting CVS materials for post-calcination treatment in oxidative atmosphere at lower temperatures to produce oxynitrides. Cubic Zn_3N_2 is stable only up to 600°C, which is not sufficient for decomposition of NH_3 and therefore microwave plasma must be used, as well different reaction zones for synthesis of Zn_3N_2 and GaN with their direct mixing in the gas phase before the particle collector.

7 References

Abe R, (2010) "Recent Progress on Photocatalytic and Photoelectrochemical Water Splitting under Visible Light Irradiation" *Journal of Photochemistry and Photobiology C: Photochemistry Reviews* 11, no. 4: 179-209. doi:10.1016/j.jphotochemrev.2011.02.003

Adeli B and Taghipour F, (2013) "A Review of Synthesis Techniques for Gallium-Zinc Oxynitride Solar-Activated Photocatalyst for Water Splitting" *ECS Journal of Solid State Science and Technology* 2, no. 7: 118-126. doi:10.1149/2.022307jss

Akatsuka M, Yoshida T, Yamamoto N, Yamamoto M, Ogawa S, and Yagi S, (2016) "XAFS Analysis for Quantification of the Gallium Coordinations in Al_2O_3-Supported Ga_2O_3 Photocatalysts" *J. Phys.: Conf. Ser.* 712: 012056. doi:10.1088/1742-6596/712/1/012056

Al-Khamis KM, Al-Othman Z and Mahfouz RM, (2010) "Kinetic Studies of the Non-Isothermal Decomposition of Unirradiated and γ-Irradiated Gallium Acetylacetonate" *Progress in Reaction Kinetics and Mechanism* 35, no. 2: 187-207. doi:10.3184/146867810X12686717520239

Aguirre MH, Shkabko A and Weidenkaff A, (2010) "Microwave Plasma Nitridation of $SrTiO_3$: A Quantitative EELS, TEM, and STEM-HAADF Analysis of the $SrTiO_{3-x}N_y$ Growth and the Structural Evolution" *Crystal Growth & Design* 10, no. 8: 3562-3567. doi:10.1021/cg100474x

Ali M and Winterer M, (2010) "ZnO Nanocrystals: Surprisingly 'Alive'" *Chemistry of Materials* 22, no. 1: 85-91. doi:10.1021/cm902240c

Ali M, Donakowski MD, Mayer C, Winterer M, (2012) "Chemical Vapor Functionalization: A Continuous Production Process for Functionalized ZnO Nanoparticles" *Journal of nanoparticle research* 14, no. 3: 689. doi:10.1007/s11051-011-0689-0

Alvi NH, Ul HK, Nur O and Willander M, (2011) "The Origin of the Red Emission in n-ZnO Nanotubes/p-GaN White Light Emitting Diodes" *Nanoscale research letters* 6, no. 1: 130. doi:10.1021/cg100474x

Ambrose D, Ewing MB, Ghiassee NB, and Sanchez-Ochoa JC (1990) "The Ebulliometric Method of Vapour-Pressure Measurement: Vapour Pressures of Benzene, Hexafluorobenzene, and Naphthalene" *The Journal of Chemical Thermodynamics* 22, no. 6: 589-605. doi:10.1016/0021-9614(90)90151-F

Aoki T, (2002) "Photoluminescence Spectroscopy" *Characterization of Materials* 1st ed., Vol. 2: 681–688. doi:10.1002/0471266965.com058.pub2

Arai T, Sato S and Morikawa T, (2015) "A Monolithic Device for CO_2 Photoreduction to Generate Liquid Organic Substances in a Single-Compartment Reactor" *Energy & Environmental Science* 8, no. 7: 1998-2002. doi:10.1039/C5EE01314C

Arakawa H, Aresta M, Armor JN, Barteau MA, Beckman EJ, Bell AT, Bercaw JE, Creutz C, Dinjus E and Dixon DA, (2001) "Catalysis Research of Relevance to Carbon Management: Progress, Challenges, and Opportunities" *Chemical reviews* 101, no. 4: 953-996. doi:10.1021/cr000018s

Baev AK and Sokolovskii AE, (1994), *Zh. Prikl. Khim. (S.-Petersburg)* 67: 1476-1481.

Baron PA, (2001), *Aerosol Fundamentals, Chap. 3 in Aerosol Measurement*, PA Baron and K. Willeke. Wiley, New York. ISBN: 978-0-470-38741-2

Boppana VBR, Doren DJ and Lobo RF, (2010) "Analysis of Ga Coordination Environment in Novel Spinel Zinc Gallium Oxy-Nitride Photocatalysts" *Journal of Materials Chemistry* 20, no. 43: 9787-9797. doi:10.1039/C0JM01928C

Bragg, WH and Bragg WL, (1913) "The Reflection of X-Rays by Crystals." *Proceedings of the Royal Society of London. Series A, Containing Papers of a Mathematical and Physical Character* 88, no. 605: 428-438. doi:10.1098/rspa.1913.0040

Branda MM, Collins SE, Castellani NJ, Baltanás MA and Bonivardi AL, (2006) "Methanol Adsorption on the β-Ga_2O_3 Surface with Oxygen Vacancies: Theoretical and Experimental Approach" *The Journal of Physical Chemistry B* 110, no. 24: 11847-11853. doi:10.1021/jp060118n

Breiland WO and Ho P, (1993) "Analysis of Chemical Vapor Deposition Processes" Vol. 91, *London Hitchman ML and Jensen KF (eds.), Academic Press*: 31-90.

Bunker G, (2010) "Introduction to XAFs: A Practical Guide to X-Ray Absorption Fine Structure Spectroscopy", Cambridge University Press. doi:10.1017/CBO9780511809194

Busser GW, Bastian M and Muhler M, (2012) "Optimizing the Deposition of Hydrogen Evolution Sites on Suspended Semiconductor Particles Using On-Line Photocatalytic Reforming of Aqueous Methanol Solutions" *ChemSusChem* 5, no. 11: 2200-2206. doi:10.1002/cssc.201200374

Busser GW, Bastian M, Pougin A, Strunk J, Gutkowski R, Schuhmann W, Willinger MG, Schlögl R and Muhler M, (2014) "Photodeposition of Copper and Chromia on Gallium Oxide: The Role of Co-Catalysts in Photocatalytic Water Splitting" *ChemSusChem* 7, no. 4 (2014): 1030-1034. doi:10.1002/cssc.201301065

Busser GW, Mei B, Weide P, Vesborg PCK, Stührenberg K, Bauer M, Huang X, Willinger MG, Chorkendorff I and Schlögl R, (2015) "Cocatalyst Designing: A Regenerable Molybdenum-Containing Ternary Cocatalyst System for Efficient Photocatalytic Water Splitting" *ACS Catalysis* 5, no. 9: 5530-5539. doi:10.1002/cssc.201301065

Chen H, Wen W, Wang Q, Hanson JC, Muckerman JT, Fujita E, Frenkel AI and Rodriguez JA, (2009) "Preparation of $(Ga_{1-x}Zn_x)(N_{1-x}O_x)$ Photocatalysts from the Reaction of NH_3 with Ga_2O_3/ZnO and $ZnGa_2O_4$: In Situ Time-Resolved XRD and XAFS Studies" *The Journal of Physical Chemistry C* 113, no. 9: 3650-59. doi:10.1021/jp804551p

Chen S, Takata T and Domen K, (2017) "Particulate Photocatalysts for Overall Water Splitting." *Nature Reviews Materials* 2, no. 10: 17050. doi:10.1038/natrevmats.2017.50

Cheng J, Chu W, Liu S, Dong P and Wu Z, (2014) "An Overview on the Research of Iron-Based High-T C Superconductors Probed by X-Ray Absorption Spectroscopy." *Journal of Superconductivity and Novel Magnetism* 27, no. 1: 9-15. doi: 10.1007/s10948-013-2405-z

Clogston JD and Patri AK, (2011) "Zeta Potential Measurement." *Characterization of Nanoparticles Intended for Drug Delivery*: *Springer*, 2011. doi:10.1007/978-1-60327-198-1_6

Cossi M, Scalmani G, Rega N and Barone V, (2002) "New Developments in the Polarizable Continuum Model for Quantum Mechanical and Classical Calculations on Molecules in Solution" *The Journal of Chemical Physics* 117, no. 1: 43-54. doi:10.1063/1.1480445

Davis EA and Mott NF, (1970) "Conduction in Non-Crystalline Systems V. Conductivity, Optical Absorption and Photoconductivity in Amorphous Semiconductors" *Philosophical Magazine* 22, no. 179: 0903-0922. doi:10.1080/14786437008221061

Dharmagunawardhane, Naveen HA, Woerner WR, Wu Q, Huang H, Chen X, Orlov A, Khalifah PG and Parise JB, (2014) "Photocatalytic Hydrogen Evolution Using Nanocrystalline Gallium Oxynitride Spinel" *Journal of Materials Chemistry A* 2, no. 45: 19247-19252. doi:10.1039/C4TA03676J

Dias A, Bundaleski N, Tatarova E, Dias FM, Abrashev M, Cvelbar U, Teodoro O and Henriques J, (2016) "Production of N-Graphene by Microwave N_2-Ar Plasma" *Journal*

of Physics D: Applied Physics 49, no. 5: 055307. doi:10.1088/0022-3727/49/5/055307

Diehm PM, Ágoston P and Albe K, (2012) "Size-Dependent Lattice Expansion in Nanoparticles: Reality or Anomaly?" *ChemPhysChem* 13, no. 10: 2443-2454. doi:10.1002/cphc.201200257

Djenadic R, Akgül G, Attenkofer K and Winterer M, (2010) "Chemical Vapor Synthesis and Structural Characterization of Nanocrystalline $Zn_{1-x}Co_xO$ (x= 0−0.50) Particles by X-Ray Diffraction and X-Ray Absorption Spectroscopy" *The Journal of Physical Chemistry C* 114, no. 20: 9207-9215. doi:10.1021/jp908148y

El Mel AA, Nakamura R and Bittencourt C, (2015) "The Kirkendall Effect and Nanoscience: Hollow Nanospheres and Nanotubes" *Beilstein journal of nanotechnology* 6, no. 1: 1348-1361. doi:10.3762/bjnano.6.139

Esswein AJ and Nocera DG, (2007) "Hydrogen Production by Molecular Photocatalysis" *Chemical reviews* 107, no. 10: 4022-4047. doi:10.1021/cr050193e

Fabian DM, Shu H, Singh N, Houle FA, Hisatomi T, Domen K, Osterloh FE and Ardo S, (2015) "Particle Suspension Reactors and Materials for Solar-Driven Water Splitting" *Energy & Environmental Science* 8, no. 10: 2825-2850. doi:10.1039/C5EE01434D

Fang S, and Yun HH, (2018) "Recent Progress in Photocatalysts for Overall Water Splitting" *International Journal of Energy Research* 43, no. 3: 1082-1098. doi:10.1002/er.4259

Fendler JH, (2008) "Nanoparticles and Nanostructured Films: Preparation, Characterization, and Applications" *John Wiley & Sons*. ISBN: 978-3-527-61206-2

Fisher John C, (1951) "Calculation of Diffusion Penetration Curves for Surface and Grain Boundary Diffusion" *Journal of Applied Physics* 22, no. 1: 74-77. doi:10.1063/1.1699825

Foo WJ, Zhang C and Ho GW, (2013) "Non-Noble Metal Cu-Loaded TiO_2 for Enhanced Photocatalytic H 2 Production" *Nanoscale* 5, no. 2: 759-764. doi:10.1039/C2NR33004K

Friedlander SK, (2000) "Smoke, Dust, and Haze" Vol. 198: *Oxford University Press* New York (USA).

Fuchs NA, Daisley RE, Fuchs M, Davies CN and Straumanis ME, (1965) "The Mechanics of Aerosols" *Physics Today* 18: 73. doi:10.1063/1.3047354

Fujishima A and Honda K, (1972) "Electrochemical Photolysis of Water at a Semiconductor Electrode" *Nature*, no. 238: 37-38. doi:10.1038/238037a0

Garcia-Martinez O, Rojas RM, Vila E and De Vidales JLM, (1993) "Microstructural Characterization of Nanocrystals of ZnO and CuO Obtained from Basic Salts" *Solid State Ionics* 63: 442-449. doi:10.1016/0167-2738(93)90142-P

Geller S, (1960) "Crystal Structure of β-Ga_2O_3" *The Journal of Chemical Physics* 33, no. 3: 676-684. doi:10.1063/1.1731237

Goldstein J, (2012) "Practical Scanning Electron Microscopy: Electron and Ion Microprobe Analysis" *Springer Science & Business Media*. ISBN: 978-3-319-92954-5

Graetzel M, Kalyanasundaram K, Borgarello E and Duonghong D, (1981) "Water Cleavage by Irradiation of Colloidal Cadmium Sulfide Solutions with Visible Light; Suppression of Photocorrosion by Ruthenium Dioxide" *Angewandte Chemie* 93: 1012-1013.

Grewe T and Tüysüz H, (2015) "Designing Photocatalysts for Hydrogen Evolution: Are Complex Preparation Strategies Necessary to Produce Active Catalysts?" *ChemSusChem* 8, no. 18: 3084-3091. doi:10.1002/cssc.201500774

Harwig T and Kellendonk F, (1978) "Some Observations on the Photoluminescence of Doped β-Galliumsesquioxide" *Journal of Solid State Chemistry* 24, no. 3-4: 255-263. doi:10.1016/0022-4596(78)90017-8

Hayashi H, Huang R, Oba F, Hirayama T and Tanaka I, (2012) "Site Preference of Cation Vacancies in Mn-Doped Ga_2O_3 with Defective Spinel Structure" *Applied Physics Letters* 101, no. 24: 241906. doi:10.1063/1.4770363

Hinds PJ, (1999) "The Curse of Expertise: The Effects of Expertise and Debiasing Methods on Prediction of Novice Performance" *Journal of experimental psychology: applied* 5, no. 2: 205. doi:10.1037/1076-898X.5.2.205

Hinds and William C, (1999) "Aerosol Technology: Properties, Behavior, and Measurement of Airborne Particles": *John Wiley & Sons*. ISBN: 978-0-471-19410-1

Hirai T, Maeda K, Yoshida M, Kubota J, Ikeda S, Matsumura M and Domen K, (2007) "Origin of Visible Light Absorption in GaN-Rich $(Ga_{1-x}Zn_x)(N_{1-x}O_x)$ Photocatalysts" *The Journal of Physical Chemistry C* 111, no. 51: 18853-18855. doi:10.1021/jp709811k

Hisatomi T, Maeda K, Lu D and Domen K, (2009) "The Effects of Starting Materials in the Synthesis of $(Ga_{1-x}Zn_x)(N_{1-x}O_x)$ Solid Solution on Its Photocatalytic Activity for Overall Water Splitting under Visible Light" *ChemSusChem: Chemistry & Sustainability Energy & Materials* 2, no. 4: 336-343. doi:10.1002/cssc.200800156C

Hisatomi T, Takanabe K, and Domen K, (2015) "Photocatalytic Water-Splitting Reaction from Catalytic and Kinetic Perspectives" *Catalysis Letters* 145, no. 1: 95-108. doi:10.1007/s10562-014-1397-z

Hisatomi T and Domen K, (2019) "Reaction Systems for Solar Hydrogen Production via Water Splitting with Particulate Semiconductor Photocatalysts" *Nature Catalysis* 2, no. 5: 387-399. doi:10.1038/s41929-019-0242-6

Ho CH, Tseng CY and Tien LC, (2010) "Thermoreflectance Characterization of β-Ga_2O_3 Thin-Film Nanostrips." *Optics express* 18, no. 16: 16360-16369. doi:10.1364/OE.18.016360

Hoffmann MR, Martin ST, Choi W, and Bahnemann DW, (1995) "Environmental Applications of Semiconductor Photocatalysis" *Chemical reviews* 95, no. 1: 69-96. doi:10.1021/cr00033a004

Houmes JD and Loye HC, (1996) "Plasma Nitridation of Metal Oxides" *Chemistry of Materials* 8, no. 11 (1996): 2551-2553. doi:10.1021/cm960384l

Hu CC and Teng H, (2010) "Gallium Oxynitride Photocatalysts Synthesized from $Ga(OH)_3$ for Water Splitting under Visible Light Irradiation" *The Journal of Physical Chemistry C* 114, no. 47: 20100-20106. doi:10.1021/jp1070083

Hu CC and Wang MS, (2017) "Photoluminescence and Photocatalysis of Gallium Oxynitride Synthesized from Nitridation of Ga_2O_3" *ECS Journal of Solid State Science and Technology* 6, no. 2: Q3001-Q06. doi:10.1149/2.0011702jss

Iguchi S, Kikkawa S, Teramura K, Hosokawa S and Tanaka T, (2016) "Investigation of the Electrochemical and Photoelectrochemical Properties of Ni–Al LDH Photocatalysts" *Physical Chemistry Chemical Physics* 18, no. 20: 13811-13819. doi:10.1039/C6CP01646D

Iguchi S, Hasegawa Y, Teramura K, Kidera S, Kikkawa S, Hosokawa S, Asakura H and Tanaka T, (2017) "Drastic Improvement in the Photocatalytic Activity of Ga_2O_3 Modified with Mg-Al Layered Double Hydroxide for Conversion of CO_2 in Water" *Sustainable Energy & Fuels* 1, no. 8: 1740-1747. doi:10.1039/C7SE00204A

Ikeda S, Hara M, Kondo JN, Domen K, Takahashi H, Okubo T and Kakihana M, (1998) "Preparation of $K_2La_2Ti_3O_{10}$ by Polymerized Complex Method and Photocatalytic Decomposition of Water" *Chemistry of Materials* 10, no. 1: 72-77. doi:10.1021/cm970221c

Ishihara T, Nishiguchi H, Fukamachi K and Takita Y, (1999) "Effects of Acceptor Doping to $KTaO_3$ on Photocatalytic Decomposition of Pure H_2O" *The Journal of Physical Chemistry B* 103, no. 1: 1-3. doi:10.1021/jp983590k

Iwasawa Y, Asakura K, and Tada M, (2017), "XAFS Techniques for Catalysts, Nanomaterials, and Surfaces": *Springer*. ISBN: 978-3-319-43866-5

Jansen H, Menze J and Muhler M, (2018) "Optimizing the Synthesis of Zinc-Rich Gallium Zinc Oxynitrides by Combining Co-Precipitation and Moisture-Assisted Nitridation" *Zeitschrift für anorganische und allgemeine Chemie* 644, no. 24: 1686-1690. doi:10.1002/zaac.201800406

Jensen LL, Muckerman JT and Newton MD, (2008) "First-Principles Studies of the Structural and Electronic Properties of the ($Ga_{1-x}Zn_x$)($N_{1-x}O_x$) Solid Solution Photocatalyst" *The Journal of Physical Chemistry C* 112, no. 9: 3439-3446. doi:10.1021/jp073554y

Karakitsou KE and Verykios XE, (1993) "Effects of Altervalent Cation Doping of Titania on Its Performance as a Photocatalyst for Water Cleavage" *The Journal of Physical Chemistry* 97, no. 6: 1184-1189. doi:10.1021/j100108a014

Kato H, Asakura K and Kudo A, (2003) "Highly Efficient Water Splitting into H_2 and O_2 over Lanthanum-Doped $NaTaO_3$ Photocatalysts with High Crystallinity and Surface Nanostructure" *Journal of the American Chemical Society* 125, no. 10: 3082-3089. doi:10.1021/ja027751g

Kay A, Cesar I and Grätzel M, (2006) "New Benchmark for Water Photooxidation by Nanostructured A-Fe_2O_3 Films" *Journal of the American Chemical Society* 128, no. 49: 15714-15721. doi:10.1021/ja064380l

Kikkawa S, Teramura K, Asakura H, Hosokawa S and Tanaka T, (2018) "Development of Rh-Doped Ga_2O_3 Photocatalysts for Reduction of CO_2 by H_2O as an Electron Donor at a More Than 300 Nm Wavelength" *The Journal of Physical Chemistry C* 122, no. 37: 21132-21139. doi:10.1021/acs.jpcc.8b04956

Kim Y-Il, Li J, Zhang JP, Seshadri R, (2011) "GaN Powders from Ammonolysis: Preparation, Structure, Morphology, and Optical Properties" *Solid state sciences* 13, no. 1: 216-223. doi:10.1016/j.solidstatesciences.2010.11.017

Klingshirn CF, Waag A, Hoffmann A and Geurts J, (2010) "Zinc Oxide: From Fundamental Properties Towards Novel Applications" Vol. 120: *Springer Science & Business Media*. ISBN: 978-3-642-10577-7

Kodas TTT, and Hampden-Smith MJ, (1999) "Aerosol Processing of Materials", *Wiley-Vch*.

Kohn, JA, Gerald K and Broder JD, (1957) "Characterization of β-Ga_2O_3 and Its Alumina Isomorph, θ-Al_2O_3" *American Mineralogist: Journal of Earth and Planetary Materials* 42, no. 5-6: 398-407.

Koningsberger DC, Mojet BL, van Dorssen GE and Ramaker D, (2000) "XAFS Spectroscopy; Fundamental Principles and Data Analysis" *Topics in catalysis* 10, no. 3-4: 143-155. doi:10.1023/A:1019105310221

Koningsberger DC and Prins R, (1988) "X-Ray Absorption: Principles, Applications, Techniques of EXAFS, SEXAFS, and XANES" *John Wiley and Sons*, New York (USA), From review Joseph E. Lester, GTE Laboratories, in Analytical Chemistry, Vol. 60.

Koponen SE, Gordon PG and Barry ST, (2016) "Principles of Precursor Design for Vapour Deposition Methods" *Polyhedron* 108: 59-66. doi:10.1016/j.poly.2015.08.024

Kosmulski M, (2009) "Compilation of PZC and IEP of Sparingly Soluble Metal Oxides and Hydroxides from Literature" *Advances in colloid and interface science* 152, no. 1-2: 14-25. doi:10.1016/j.cis.2009.08.003

Kubelka P and Munk F, (1931), *Z Techn. Phys.* 12: 593.

Kubelka P, (1948), *J. Opt. Soc. Am*.38 (1931): 448.

Kudo A, Sayama K, Tanaka A, Asakura K, Domen K, Maruya K, and Onishi T, (1989) "Nickel-Loaded $K_4Nb_6O_{17}$ Photocatalyst in the Decomposition of H_2O into H_2 and O_2: Structure and Reaction Mechanism" *Journal of catalysis* 120, no. 2: 337-352. doi:10.1016/0021-9517(89)90274-1

Kudo A and Miseki Y, (2009) "Heterogeneous Photocatalyst Materials for Water Splitting" *Chemical Society Reviews* 38, no. 1 (2009): 253-78. doi:10.1039/B800489G

Kumar M, Pasha S, Krishna TCS, Avanish P, Kumar P, Gupta BK and Gupta G, (2014) "Facile Synthesis and Photoluminescence Spectroscopy of 3d-Triangular GaN Nano Prism Islands" *Dalton Transactions* 43, no. 31: 11855-11861. doi:10.1039/C4DT01191K

Lee Y, Terashima H, Shimodaira Y, Teramura K, Hara M, Kobayashi H, Domen K and Yashima M, (2007) "Zinc Germanium Oxynitride as a Photocatalyst for Overall Water Splitting under Visible Light" *The Journal of Physical Chemistry C* 111, no. 2: 1042-48. doi:10.1021/jp0656532

Lee K, Tienes BM, Wilker MB, Schnitzenbaumer KJ and Dukovic G, (2012) $(Ga_{1-x}Zn_x)(N_{1-x}O_x)$ Nanocrystals: Visible Absorbers with Tunable Composition and Absorption Spectra." *Nano letters* 12, no. 6: 3268-3272. doi:10.1021/nl301338z

Lee K, Lu YG, Chuang CH, Ciston J and Dukovic G, (2016) "Synthesis and Characterization of $(Ga_{1-x}Zn_x)(N_{1-x}O_x)$ Nanocrystals with a Wide Range of Compositions" *Journal of Materials Chemistry A* 4, no. 8: 2927-2935. doi:10.1039/C5TA04314J

Leineweber A, (2011) "Understanding Anisotropic Microstrain Broadening in Rietveld Refinement" *Zeitschrift für Kristallographie Crystalline Materials* 226, no. 12: 905-923. doi:10.1524/zkri.2011.1413

Leijtens T, Eperon GE, Bush KA, Prasanna R, Green T, Wang JTW, McMeekin DP, Volonakis G, Milot RL and May R, (2016) "Perovskite-Perovskite Tandem Photovoltaics with Optimized Band Gaps" *Science* 354, no. 6314: 861-865. doi:10.1126/science.aaf9717

Levinshtein ME, Rumyantsev SL and Shur MS, (2001) "Properties of Advanced Semiconductor Materials: GaN, AlN, InN, BN, SiC, SiGe" *John Wiley & Sons*. ISBN: 0-471-35827-4

Lewis NS, Crabtree G, Nozik AJ, Wasielewski MR, Alivisatos P, Kung H, Tsao J, Chandler E, Walukiewicz W and Spitler M, (2005) "*Basic Research Needs for Solar Energy Utilization. Report of the Basic Energy Sciences Workshop on Solar Energy Utilization*", *3-4*. doi:10.2172/899136

Li L, Wie W and Behrens M, (2012) "Synthesis and Characterization of α-, β-, and γ-Ga_2O_3 Prepared from Aqueous Solutions by Controlled Precipitation" *Solid state sciences* 14, no. 7: 971-981. doi:10.1016/j.solidstatesciences.2012.04.037

Lide David R, (2003), "CrC Handbook of Chemistry and Physics: A Ready-Reference Book of Chemical and Physical Data": *CRC press*. ISBN13: 978-0849304842

Linde DR, (1993) "Crc Handbook of Chemistry and Physics." *Boca Raton: CRC Press* 1994: 148-55.

Liu B, Bando Y, Dierre B, Sekiguchi T, Tang C, Mitome Ma, Wu A, Jiang X and Golberg D, (2009) "The Synthesis, Structure and Cathodoluminescence of Ellipsoid-Shaped $ZnGa_2O_4$ Nanorods." *Nanotechnology* 20, no. 36: 365705. doi:10.1088/0957-4484/20/36/365705

Lorenz K, Nogales E, Miranda SMC, Franco NMB, Alves E, Tourbot G and Daudin B, (2013) "Enhanced Red Emission from Praseodymium-Doped GaN Nanowires by Defect Engineering" *Acta Materialia* 61, no. 9: 3278-3284. doi:10.1016/j.actamat.2013.02.016

Lowell S, Shields JE, Thomas MA and Thommes M, (2012), "Characterization of Porous Solids and Powders: Surface Area, Pore Size and Density" Vol. 16: *Springer Science & Business Media*. ISBN: 978-1-4020-2303-3

Lutterotti L. (2010) "Total Pattern Fitting for the Combined Size-Strain-Stress-Texture Determination in Thin Film Diffraction" *Nuclear Instruments and Methods in Physics Research B*. 268: 334-340.

Maeda K, Takata T, Hara M, Saito N, Inoue Y, Kobayashi H and Domen K, (2005) "GaN:ZnO Solid Solution as a Photocatalyst for Visible-Light-Driven Overall Water Splitting" *Journal of the American Chemical Society* 127, no. 23 (2005): 8286-8287. doi:10.1021/ja0518777

Maeda K, Teramura K, Lu D, Takata T, Saito N, Inoue Y and Domen K, (2006) "Photocatalyst Releasing Hydrogen from Water" *Nature* 440, no. 7082: 295-295. doi:10.1038/440295a

Maeda K, Teramura K, Masuda H, Takata T, Saito N, Inoue Y and Domen K, (2006) "Efficient Overall Water Splitting under Visible-Light Irradiation on $(Ga_{1-x}Zn_x)(N_{1-x}O_x)$ Dispersed with Rh−Cr Mixed-Oxide Nanoparticles: Effect of Reaction Conditions on Photocatalytic Activity." *The Journal of Physical Chemistry B* 110, no. 26: 13107-13112. doi:10.1021/jp0616563

Maeda K, Teramura K, Lu D, Saito N, Inoue Y and Domen K, (2007) "Roles of Rh/Cr_2O_3 (Core/Shell) Nanoparticles Photodeposited on Visible-Light-Responsive $(Ga_{1-x}Zn_x)(N_{1-x}O_x)$ Solid Solutions in Photocatalytic Overall Water Splitting" *The Journal of Physical Chemistry C* 111, no. 20: 7554-7560. doi:10.1021/jp071056j

Maeda K and Domen K, (2007) "New Non-Oxide Photocatalysts Designed for Overall Water Splitting under Visible Light" *The Journal of Physical Chemistry C* 111, no. 22: 7851-7861. doi:10.1021/jp070911w

Maeda K, Teramura K and Domen K, (2008) "Effect of Post-Calcination on Photocatalytic Activity of $(Ga_{1-x}Zn_x)(N_{1-x}O_x)$ Solid Solution for Overall Water Splitting under Visible Light" *Journal of catalysis* 254, no. 2: 198-204. doi:10.1016/j.jcat.2007.12.009

Maeda K, Hashiguchi H, Masuda H, Abe R and Domen K, (2008) "Photocatalytic Activity of $(Ga_{1-x}Zn_x)(N_{1-x}O_x)$ for Visible-Light-Driven H_2 and O_2 Evolution in the Presence of Sacrificial Reagents" *The Journal of Physical Chemistry C* 112, no. 9: 3447-52. doi:10.1021/jp710758q

Maeda K and Domen K, (2010) "Solid Solution of GaN and ZnO as a Stable Photocatalyst for Overall Water Splitting under Visible Light" *Chemistry of Materials* 22, no. 3: 612-623. doi:10.1021/cm901917a

Maeda K, Sakamoto N, Ikeda T, Ohtsuka H, Xiong A, Lu D, Kanehara M, Teranishi T and Domen K, (2010) "Preparation of Core–Shell-Structured Nanoparticles (with a Noble-Metal or Metal Oxide Core and a Chromia Shell) and Their Application in Water Splitting by Means of Visible Light" *Chemistry–A European Journal* 16, no. 26: 7750-7759. doi:10.1002/chem.201000616

Maeda K, Xiong A, Yoshinaga T, Ikeda T, Sakamoto N, Hisatomi T, Takashima M, Lu D, Kanehara M and Setoyama T, (2010) "Photocatalytic Overall Water Splitting Promoted by Two Different Cocatalysts for Hydrogen and Oxygen Evolution under Visible Light" *Angewandte Chemie International Edition* 49, no. 24: 4096-4099. doi:10.1002/anie.201001259

Maeda K, (2011) "Photocatalytic Water Splitting Using Semiconductor Particles: History and Recent Developments" *Journal of Photochemistry and Photobiology C: Photochemistry Reviews* 12, no. 4: 237-268. doi:10.1016/j.jphotochemrev.2011.07.001

Maeda K, Ohno T and Domen K, (2011) "A Copper and Chromium Based Nanoparticulate Oxide as a Noble-Metal-Free Cocatalyst for Photocatalytic Water Splitting" *Chemical Science* 2, no. 7: 1362-1368. doi:10.1039/C1SC00177A

Maeda K and Domen K, (2016) "Development of Novel Photocatalyst and Cocatalyst Materials for Water Splitting under Visible Light" *Bulletin of the Chemical Society of Japan* 89, no. 6: 627-648. doi:10.1246/bcsj.20150441

Martin M, Dronskowski R, Janek J, Becker KD, Roehrens D, Brendt J, Lumey MW, Nagarajan L, Valov I and Börger A, (2009) "Thermodynamics, Structure and Kinetics

in the System Ga–O–N" *Progress in Solid State Chemistry* 37, no. 2-3: 132-152. doi:10.1016/j.progsolidstchem.2009.11.005

McDonald JE, (1963) "Homogeneous Nucleation of Vapor Condensation. Ii. Kinetic Aspects" *American Journal of Physics* 31, no. 1: 31-41. doi:10.1119/1.1969234

Momma K and Izumi F, (2011) "Vesta 3 for Three-Dimensional Visualization of Crystal, Volumetric and Morphology Data" *Journal of applied crystallography* 44, no. 6: 1272-1276. doi:10.1107/S0021889811038970

Navarro-Yerga RM, Galván MCA, Del Valle F, De La Mano V and Fierro, JLF, (2009) "Water Splitting on Semiconductor Catalysts under Visible-Light Irradiation" *ChemSusChem* 2: 471-485. doi:10.1002/cssc.200900018

Neugebauer J and Van de Walle CG, (1996) "Gallium Vacancies and the Yellow Luminescence in GaN" *Applied Physics Letters* 69, no. 4: 503-505. doi:10.1063/1.117767

Ni M, Leung MKH, Leung DYC and Sumathy K, (2007) "A Review and Recent Developments in Photocatalytic Water-Splitting Using TiO_2 for Hydrogen Production" *Renewable and Sustainable Energy Reviews* 11, no. 3: 401-425. doi:10.1016/j.rser.2005.01.009

Nishi K, Shimizu K, Takamatsu M, Yoshida H, Satsuma A, Tanaka T, Yoshida S and Hattori T, (1998) "Deconvolution Analysis of Ga K-Edge XANES for Quantification of Gallium Coordinations in Oxide Environments" *The Journal of Physical Chemistry B* 102, no. 50: 10190-10195. doi:10.1021/jp982704p

Ognjanovic S, (2019) "Chemical Vapor Synthesis and Characterization of Aluminum Nitride Nanoparticles as Precursors for Phosphors" *Dissertation,* University Duisburg-Essen. doi:10.17185/duepublico/70744

Ohno T, Bai L, Hisatomi T, Maeda K and Domen K, (2012) "Photocatalytic Water Splitting Using Modified GaN:ZnO Solid Solution under Visible Light: Long-Time Operation and Regeneration of Activity" *Journal of the American Chemical Society* 134, no. 19: 8254-8259. doi:10.1021/ja302479f

Okuyama K, Ushio R, Kousaka Y, Flagan RC and Seinfeld JH, (1990) "Particle Generation in a Chemical Vapor Deposition Process with Seed Particles." *AIChE journal* 36, no. 3: 409-419. doi:10.1002/aic.690360310

Onuma T, Fujioka S, Yamaguchi T, Higashiwaki M, Sasaki K, Masui T, and Honda T, (2013) "Correlation between Blue Luminescence Intensity and Resistivity in β-Ga_2O_3 Single Crystals" *Applied Physics Letters* 103, no. 4: 041910. doi:10.1063/1.4816759

Ouhbi H and Aschauer U, (2019) "Nitrogen Loss and Oxygen Evolution Reaction Activity of Perovskite Oxynitrides" *ACS Materials Letters* 1: 52-57. doi:10.1021/acsmaterialslett.9b00088

Osterloh FE, (2013) "Inorganic Nanostructures for Photoelectrochemical and Photocatalytic Water Splitting" *Chemical Society Reviews* 42, no. 6: 2294-2320. doi:10.1039/C2CS35266D

Pecora R, (2000) "Dynamic Light Scattering Measurement of Nanometer Particles in Liquids" *Journal of nanoparticle research* 2, no. 2: 123-131. doi:10.1023/A:1010067107182

Phivilay SP, Roberts CA, Puretzky AA, Domen K and Wachs IE, (2013) "Fundamental Bulk/Surface Structure–Photoactivity Relationships of Supported (Rh_{2-y}/Cr_yO_3)/GaN Photocatalysts" *The Journal of Physical Chemistry Letters* 4, no. 21: 3719-3724. doi:10.1021/jz401884c

Pinaud BA, Benck JD, Seitz LC, Forman AJ, Chen Z, Deutsch TG, James BD, Baum KN, Baum GN and Ardo S, (2013), *Energy Environ Sci 6: 1983*. doi:10.1039/C3EE40831K

Popa A, Toloman D, Stan M, Silipas TD and Biris AR, (2015) "Optical and Electron Paramagnetic Resonance Studies of Cr Doped Ga_2O_3 Nanoparticles", Vol. 1700. *AIP Conference Proceedings: AIP Publishing*.

Popa NC, (1998) "The (hkl) Dependence of Diffraction-Line Broadening Caused by Strain and Size for All Laue Groups in Rietveld Refinement" *Journal of applied crystallography* 31, no. 2: 176-180. doi:10.1107/S0021889897009795

Prabhakar RR, Mathews N, Jinesh KB, Karthik KRG, Pramana SS, Varghese B, Sow CH and Mhaisalkar, (2012) "Efficient Multispectral Photodetection Using Mn Doped ZnO Nanowires" *Journal of Materials Chemistry* 22, no. 19: 9678-9683. doi:0.1039/C2JM16698D

Pratsinis SE, (1988) "Simultaneous Nucleation, Condensation, and Coagulation in Aerosol Reactors" *Journal of Colloid and Interface Science* 124, no. 2: 416-427. doi:10.1016/0021-9797(88)90180-4

Qian HS, Gunawan P, Zhang YX, Lin GF, Zheng JW and Xu R, (2008) "Template-Free Synthesis of Highly Uniform α-GaOOH Spindles and Conversion to α-Ga_2O_3 and β-Ga_2O_3" *Crystal Growth and Design* 8, no. 4: 1282-1287. doi:10.1021/cg701004w

Quaschning V, (2016), "Understanding Renewable Energy Systems" *Routledge*, New York (USA). ISBN: 978-1-138-78194-8

Quaschning V, (2016) "Renewable Energy and Climate Change" *John Wiley & Sons*. ISBN: 978-0-470-74707-0

Rai G and Kumar A, (2014) "Elucidation of Ionic Interactions in the Protic Ionic Liquid Solutions by Isothermal Titration Calorimetry" *The Journal of Physical Chemistry B* 118, no. 15: 4160-4168. doi:10.1021/jp5019179

Raidongia K and Rao CNR, (2008) "Study of the Transformations of Elemental Nanowires to Nanotubes of Metal Oxides and Chalcogenides through the Kirkendall Effect" *The Journal of Physical Chemistry C* 112, no. 35: 13366-13371. doi:10.1021/jp8043658

Rehr JJ, Kas JJ, Vila FD, Prange MP and Jorissen K, (2010) "Parameter-Free Calculations of X-Ray Spectra with Feff9" *Physical Chemistry Chemical Physics* 12, no. 21: 5503-5513. doi:10.1039/B926434E

Reimer L, (2013) "Transmission Electron Microscopy: Physics of Image Formation and Microanalysis", Vol. 36: *Springer*. ISBN: 13:978-0387400938

Rietveld HaM, (1969) "A Profile Refinement Method for Nuclear and Magnetic Structures" *Journal of applied crystallography* 2, no. 2: 65-71. doi:10.1107/S0021889869006558

Roehrens D, Brendt J, Samuelis D and Martin M, (2010) "On the Ammonolysis of Ga_2O_3: An XRD, Neutron Diffraction and XAS Investigation of the Oxygen-Rich Part of the System Ga_2O_3–GaN" *Journal of Solid State Chemistry* 183, no. 3: 532-541. doi:10.1016/j.jssc.2009.12.024

Sabio-Erwin M, Chamousis RL, Browning N, and Osterloh FE, (2012) "Photocatalytic Water Splitting with Suspended Calcium Niobium Oxides: Why Nanoscale Is Better Than Bulk – a Kinetic Analysis" *The Journal of Physical Chemistry C* 116, no. 4: 3161-3170. doi:10.1021/jp209006n

Sakakura T, Murakami N, Takatsuji Y, Morimoto M and Haruyama T, (2019) "Contribution of Discharge Excited Atomic N, N_2^*, and N_2^+ to a Plasma/Liquid Interfacial Reaction as Suggested by Quantitative Analysis" *ChemPhysChem* 20, no. 11: 1467-74. 10.1002/cphc.201900212

Sakamoto N, Ohtsuka H, Ikeda T, Maeda K, Lu D, Kanehara M, Teramura K, Teranishi T and Domen K, (2009) "Highly Dispersed Noble-Metal/Chromia (Core/Shell) Nanoparticles as Efficient Hydrogen Evolution Promoters for Photocatalytic Overall Water Splitting under Visible Light" *Nanoscale* 1, no. 1: 106-109. doi:10.1039/B9NR00186G

Sakata Y, Matsuda Y, Yanagida T, Hirata K, Imamura H and Teramura K, (2008) "Effect of Metal Ion Addition in a Ni Supported Ga_2O_3 Photocatalyst on the Photocatalytic

Overall Splitting of H_2O" *Catalysis Letters* 125, no. 1-2: 22-26. doi:10.1007/s10562-008-9557-7

Sakata Y, Matsuda Y, Nakagawa T, Yasunaga R, Imamura H and Teramura K, (2011) "Remarkable Improvement of the Photocatalytic Activity of Ga_2O_3 Towards the Overall Splitting of H_2O" *ChemSusChem* 4, no. 2: 181-184. doi:10.1002/cssc.201000258

Sakata Y, Nakagawa T, Nagamatsu Y, Matsuda Y, Yasunaga R, Nakao E and Imamura H, (2014) "Photocatalytic Properties of Gallium Oxides Prepared by Precipitation Methods toward the Overall Splitting of H_2O" *Journal of catalysis* 310: 45-50. doi:10.1016/j.jcat.2013.06.025

Scaife DE, (1980) "Oxide Semiconductors in Photoelectrochemical Conversion of Solar Energy" *Solar Energy* 25, no. 1: 41-54. doi:10.1016/0038-092X(80)90405-3

Schilling C and Winterer M, (2014) "Preserving Particle Characteristics at Increasing Production Rate of ZnO Nanoparticles by Chemical Vapor Synthesis." *Chemical Vapor Deposition* 20, no. 4-5-6: 138-145. doi:10.1002/cvde.201307094

Schulz H and Thiemann KH, (1977) "Crystal Structure Refinement of AlN and GaN" *Solid State Communications* 23, no. 11: 815-819. doi:10.1016/0038-1098(77)90959-0

Seinfeld JH, and Pandis SN, (1998) "Atmospheric Chemistry and Physics: From Air Pollution to Climate Change" *John Willey and Sons,* (USA). ISBN: 978-1-118-94740-1

Shannon RD, (1976) "Revised Effective Ionic Radii and Systematic Studies of Interatomic Distances in Halides and Chalcogenides" *Acta crystallographica section A: crystal physics, diffraction, theoretical and general crystallography* 32, no. 5: 751-767. doi:10.1107/S0567739476001551

Shimura K, Yoshida T and Yoshida H, (2010) "Photocatalytic Activation of Water and Methane over Modified Gallium Oxide for Hydrogen Production" *The Journal of Physical Chemistry C* 114, no. 26: 11466-11474. doi:10.1021/jp1012126

Shimura K and Yoshida H, (2012) "Effect of Doped Zinc Species on the Photocatalytic Activity of Gallium Oxide for Hydrogen Production" *Physical Chemistry Chemical Physics* 14, no. 8: 2678-2684. doi:10.1039/C2CP23220K

Soldat J, Busser GW, Muhler M and Wark M, (2016) "Cr_2O_3 Nanoparticles on $Ba_5Ta_4O_{15}$ as a Noble-Metal-Free Oxygen Evolution Co-Catalyst for Photocatalytic Overall Water Splitting" *ChemCatChem* 8, no. 1: 153-156. doi:10.1002/cctc.201500977

Stenzel Olaf, (2015) "The Physics of Thin Film Optical Spectra": *Springer*. ISBN: 978-3-319-21602-7

Sun X, Maeda K, Le Faucheur M, Teramura K and Domen K, (2007) "Preparation of $(Ga_{1-x}Zn_x)(N_{1-x}O_x)$ Solid-Solution from $ZnGa_2O_4$ and ZnO as a Photo-Catalyst for Overall Water Splitting under Visible Light" *Applied Catalysis A: General* 327, no. 1: 114-121. doi:10.1016/j.apcata.2007.05.005

Sung MC, Kuo YM, Hsieh LT and Tsai CH, (2017) "Two-Stage Plasma Nitridation Approach for Rapidly Synthesizing Aluminum Nitride Powders" *Journal of Materials Research* 32, no. 7: 1279-1286. doi:10.1557/jmr.2016.505

Takata T, Pan C and Domen K, (2015) "Recent Progress in Oxynitride Photocatalysts for Visible-Light-Driven Water Splitting" *Science and technology of advanced materials* 16, no. 3: 033506. doi:10.1088/1468-6996/16/3/033506

Takata T, Pan C and Domen K, (2016) "Design and Development of Oxynitride Photocatalysts for Overall Water Splitting under Visible Light Irradiation" *ChemElectroChem* 3, no. 1: 31-37. doi:10.1002/celc.201500324

Tang C, Sun J, Lin N, Jia Z, Mu W, Tao, and Zhao X, (2016) "Electronic Structure and Optical Property of Metal-Doped Ga_2O_3: A First Principles Study" *RSC Advances* 6, no. 82: 78322-78334. doi:10.1039/C6RA14010F

Tauc J, (1968) "Optical Properties and Electronic Structure of Amorphous Ge and Si" *Materials Research Bulletin* 3, no. 1: 37-46. doi:10.1016/0025-5408(68)90023-8

Toloman D, Popa A, Stan M, Silipas TD and Biris AR, (2015) "Identification of Different Iron Sites in β-Ga_2O_3 Nanoparticles by Spectroscopic" *Methods*. Vol. 1700. AIP Conference Proceedings: AIP Publishing. doi:10.1063/1.4938455

Tongying P, Lu YG, Hall LMG, Lee K, Sulima M, Ciston J and Dukovic G, (2017) "Control of Elemental Distribution in the Nanoscale Solid-State Reaction That Produces ($Ga_{1-x}Zn_x$)($N_{1-x}O_x$) Nanocrystals" *ACS nano* 11, no. 8: 8401-8412. doi:10.1021/acsnano.7b03891

Townsend TK, Sabio ES, Browning ND and Osterloh FE, (2011) "Photocatalytic Water Oxidation with Suspended Alpha-Fe_2O_3 Particles-Effects of Nanoscaling" *Energy & Environmental Science* 4, no. 10: 4270-4275. doi:10.1039/C1EE02110A

Tripathi AD, Mishra R, Maurya KK, Singh RB and Wilson DW, (2019) "Estimates for World Population and Global Food Availability for Global Health" *The Role of Functional Food Security in Global Health*: Elsevier. doi:10.1016/B978-0-12-813148-0.00001-3

Valavanis A, (2009) "n-type Silicon-Germanium Based Terahertz Quantum Cascade Lasers" *Dissertation,* University of Leeds, 9. uk.bl.ethos.505065

Vanheusden K, Warren WL, Seager CH, Tallant DR, Voigt JA, and Gnade BE, (1996) "Mechanisms Behind Green Photoluminescence in ZnO Phosphor Powders" *Journal of Applied Physics* 79, no. 10 : 7983-7990. doi:10.1063/1.362349

Vasyltsiv V, Luchechko A, Kostyk L, and Pavlyk B, (2019) "Effect of Deep Trap Levels on Green Luminescence in β-Ga_2O_3" *XI International Scientific and Practical Conference on Electronics and Information Technologies (ELIT): IEEE*. doi:10.1109/ELIT.2019.8892283

Wang HF and Liu ZP, (2009) "Formic Acid Oxidation at Pt/H_2O Interface from Periodic DFT Calculations Integrated with a Continuum Solvation Model" *The Journal of Physical Chemistry C* 113, no. 40: 17502-17508. doi:10.1021/jp9059888

Wang T and Radovanovic PV, (2011) "In Situ Enhancement of the Blue Photoluminescence of Colloidal Ga_2O_3 Nanocrystals by Promotion of Defect Formation in Reducing Conditions" *Chemical Communications* 47, no. 25: 7161-7163. doi:10.1039/C1CC11957E

Wang X, Xu Q, Li M, Shen S, Wang X, Wang Y, Feng Z, Shi J, Han H and Li C, (2012), "Photocatalytic Overall Water Splitting Promoted by an α–β Phase Junction on Ga_2O_3" *Angewandte Chemie International Edition* 51, no. 52: 13089-13092. doi:10.1002/anie.201207554

Wang X, Shen S, Jin S, Yang J, Li M, Wang X, Han H and Li C, (2013) "Effects of Zn^{2+} and Pb^{2+} Dopants on the Activity of Ga_2O_3-Based Photocatalysts for Water Splitting" *Physical Chemistry Chemical Physics* 15, no. 44: 19380-19386. doi:10.1039/C3CP53333F

Wang Z, Han J, Li Z, Li M, Wang H, Zong X and Li C, (2016) "Moisture-Assisted Preparation of Compact GaN: ZnO Photoanode toward Efficient Photoelectrochemical Water Oxidation" *Advanced Energy Materials* 6, no. 20: 1600864. doi:10.1002/aenm.201600864

Wang D, Zhang M, Zhuang H, Chen X, Wang X, Zheng X and Yang J, (2017) "The Photocatalytic Properties of Hollow $(GaN)_{1-x}(Zno)_x$ Composite Nanofibers Synthesized by Electrospinning" *Applied Surface Science* 396: 888-896. doi:10.1016/j.apsusc.2016.11.053

Wang WK, Xu YJ, Huang SY, Liu KF and Tsai PC, (2019) "Structural Characteristics and Photoluminescence Properties of Sputter-Deposition $ZnGa_2O_4$ Thin Films on Sapphire and Si (100) Substrates" *Coatings* 9, no. 8: 469. doi:10.3390/coatings9080469

Wang Z, Li C and Domen K, (2019) "Recent Developments in Heterogeneous Photocatalysts for Solar-Driven Overall Water Splitting" *Chemical Society Reviews* 48, no. 7: 2109-2125. doi:10.1039/C8CS00542G

Wani S, Sofi HS, Sheikh FA, Shivashankar SA and Majeed S, (2017) "$ZnGa_2O_4$ Nanophosphors: Rapid Synthesis, Characterization and Luminescence Properties" *Material Science Research India* 14, no. 2: 116-122. doi:10.13005/msri/140205

Warren BE, (1990) "X-Ray Diffraction" *Courier Corporation*. ISBN: 0486663175

Wei SH and Zunger A, (1988) "Role of Metal d States in II-VI Semiconductors" *Physical Review B* 37, no. 15: 8958. doi:10.1103/PhysRevB.37.8958

Winterer M, (1997) "XAFS Data Analysis Program for Materials Science" *Le Journal de Physique* IV 7, no. C2: 243-244.

Winterer M, (2000) "Reverse Monte Carlo Analysis of Extended X-Ray Absorption Fine Structure Spectra of Monoclinic and Amorphous Zirconia" *Journal of Applied Physics* 88, no. 10: 5635-5644. doi:10.1063/1.1319167

Winterer M, (2002) "Nanocrystalline Ceramics: Synthesis and Structure" *Physics and Astronomy Online Library, Springer*, Berlin, Germany, ISBN: 354043433X

Winterer M, (2018) "Discovering Paths to Optimized Nanoparticle Characteristics" *Chemical Engineering Science* 186: 135-141. doi:10.1016/j.ces.2018.04.005

Yanagida T, Sakata Y and Imamura H, (2004) "Photocatalytic Decomposition of H_2O into H_2 and O_2 over Ga_2O_3 Loaded with NiO" *Chemistry letters* 33, no. 6: 726-727. doi:10.1246/cl.2004.726

Yang J, Wang D, Han H and Li C, (2013) "Roles of Cocatalysts in Photocatalysis and Photoelectrocatalysis" *Accounts of chemical research* 46, no. 8: 1900-1909.

Yang P, Yan H, Mao S, Russo R, Johnson J, Saykally R, Morris N, Pham J, He R and Choi HJ, (2002) "Controlled Growth of ZnO Nanowires and Their Optical Properties" *Advanced functional materials* 12, no. 5: 323-31. doi:10.1002/1616-3028(20020517)12:5<323::AID-ADFM323>3.0.CO;2-G

Yao J, Liu T and Wang B, (2019) "Optical Properties for the Oxygen Vacancies in β-Ga_2O_3 Based on First-Principles Calculations" *Materials Research Express* 6, no. 7: 075913. doi:10.1088/2053-1591/ab17be

Yashima M, Maeda K, Teramura K, Takata T and Domen K, (2005) "Crystal Structure and Optical Properties of $(Ga_{1-x}Zn_x)(N_{1-x}O_x)$ Oxynitride Photocatalyst (x = 0.13)." *Chemical physics letters* 416, no. 4-6: 225-228. doi:10.1016/j.cplett.2005.09.092

Yuliati L, Hattori T, Itoh H and Yoshida H, (2008) "Photocatalytic Nonoxidative Coupling of Methane on Gallium Oxide and Silica-Supported Gallium Oxide" *Journal of catalysis* 257, no. 2: 396-402. doi:10.1016/j.jcat.2008.05.022

Zeng S, Aliev GN, Wolverson D, Davies JJ, Bingham SJ, Abdulmalik DA, Coleman PG, Wang T and Parbrook PJ, (2006) "Origin of the Red Luminescence in Mg-Doped GaN" *Applied Physics Letters* 89, no. 2: 022107. doi:10.1063/1.2220552

Zeng X, Han B, Wang X, Shi J, Xu Y, Zhang J, Wang J, Zhang J and Xu K, (2013) "Comparison of Morphology, Structure and Optical Properties of GaN Powders Prepared by Ga_2O_3 Nitridation and Gallium Nitridation" *Journal of crystal growth* 367: 48-52. doi:10.1016/j.jcrysgro.2013.01.004

Zhang L, Yan J, Zhang Y, Li T and Ding X, (2012) "A Comparison of Electronic Structure and Optical Properties between N-Doped β-Ga_2O_3 and N–Zn Co-Doped β-Ga_2O_3" *Physica B: Condensed Matter* 407, no. 8: 1227-1231. doi:10.1016/j.physb.2012.01.107

Zhang Yi, Ligthart M, Liu P, Gao L, Verhoeven T and Hensen E, (2014) "Size Dependence of Photocatalytic Oxidation Reactions of Rh Nanoparticles Dispersed on $(Ga_{1-x}Zn_x)(N_{1-x}O_x)$ Support" *Chinese Journal of Catalysis* 35, no. 12: 1944-1954. doi:10.1016/S1872-2067(14)60181-9

Zhang J, Tian B, Wang L, Xing M and Lei J, (2018) "Mechanism of Photocatalysis" *Photocatalysis*: *Springer*. ISBN: 978-981-13-2112-2

Zhou X, Liu R, Sun K, Chen Y, Verlage E, Francis SA, Lewis NS, and Xiang C, (2016) "Solar-Driven Reduction of 1 Atm of CO_2 to Formate at 10% Energy-Conversion Efficiency by Use of a TiO_2-Protected III–V Tandem Photoanode in Conjunction with a Bipolar Membrane and a Pd/C Cathode" *ACS Energy Letters* 1, no. 4: 764-770. doi:10.1021/acsenergylett.6b00317

8 Appendix

Table A8.1. Properties of bulk materials

Property	Ga_2O_3	GaN	ZnO
Molar mass (g/mol)	187.4	83.73	81.4
Density (g/cm^3)	5.88	6.1	5.6
Melting point (°C)	1900	>1600	1975
Band gap (eV)	4.8-4.9	3.4	3.3

Lide David R, (2003), "CrC Handbook of Chemistry and Physics: A Ready-Reference Book of Chemical and Physical Data": *CRC press*. ISBN: 0-8493-0485-7

Table A8.2. Properties of precursors

Property	Value	
Molecular formula	$GaC_{15}H_{21}O_6$	
Molar mass (g/mol)	367.05	
Density (g/cm^3) at 20°C	1.42	$Ga(acac)_3$
Melting point (°C)	196-198	
Boiling point (°C)	140 (10 mm Hg)	
Molecular formula	$C_{22}H_{40}O_4Zn$	
Molar mass (g/mol)	431.92	
Density (g/cm^3) at 20°C	N/A	$Zn(TMHD)_2$
Melting point (°C)	132-134	
Boiling point (°C)	250	
Molecular formula	$C_{15}H_{21}MnO_6$	
Molar mass (g/mol)	352.3	
Density (g/cm^3) at 20°C	N/A	$Mn(acac)_3$
Melting point (°C)	159-161	
Boiling point (°C)	decomposes	
Molecular formula	$C_{15}H_{21}O_6Rh$	
Molar mass (g/mol)	400.23	
Density (g/cm^3) at 20°C	N/A	$Rh(acac)_3$
Melting point (°C)	263-264	
Boiling point (°C)	decomposes	
Molecular formula	$C_{15}H_{21}FeO_6$	
Molar mass (g/mol)	353.17	
Density (g/cm^3) at 20°C	N/A	$Fe(acac)_3$
Melting point (°C)	180-182	
Boiling point (°C)	decomposes	
Molecular formula	$(C_2H_5)_3Ga$	
Molar mass (g/mol)	156.9	
Density (g/cm^3) at 20°C	1.067	Triethylgallium (TEG)
Melting point (°C)	-82.3	
Boiling point (°C)	143	

Molecular formula	$(C_2H_5)_2Zn$	
Molar mass (g/mol)	123.5	
Density (g/cm^3) at 20°C	1.2	Diethylzinc (DEZ)
Melting point (°C)	-28	
Boiling point (°C)	117	

Lide David R, (2003), "CrC Handbook of Chemistry and Physics: A Ready-Reference Book of Chemical and Physical Data": *CRC press*. ISBN: 0-8493-0485-7

Table A8.3. Overview of the CVS synthesis parameters for the most important samples directly synthesized via CVS and used in this work. Nitridation conditions are not included.

#	Material	*T*	*p*	O_2	NH_3	*He*	*R#*
‡		°C	mbar	sccm	sccm	sccm	
1	Ga_2O_3	1200	20	1700	/	600	1
2	Ga_2O_3	1200	40	1700	/	600	1
3	Ga_2O_3	1200	100	1700	/	600	1
4	Ga_2O_3	1200	150	1700	/	600	1
5	Ga_2O_3	1200	300	1700	/	600	1
6	Ga_2O_3	1000	300	1700	/	600	1
7	Ga_2O_3	1100	300	1700	/	600	1
8	Ga_2O_3	1300	300	1700	/	600	1
9	Ga_2O_3	1400	300	1700	/	600	1
10	Ga_2O_3	1500	300	1700	/	600	1
11	Ga_2O_3	1200	300	1700	/	600	1
12	0.26 % Mn-doped Ga_2O_3	1200	300	1700	/	600	1
13	1.38 % Mn-doped Ga_2O_3	1200	300	1700	/	600	1
14	1.60 % Mn-doped Ga_2O_3	1200	300	1700	/	600	1
15	7.30 % Mn-doped Ga_2O_3	1200	300	1700	/	600	1
16	1.00 % Rh-doped Ga_2O_3	1200	300	1700	/	600	1
17	5.00 % Rh-doped Ga_2O_3	1200	300	1700	/	600	1
18	5.00 % Fe-doped Ga_2O_3	1200	300	1700	/	600	1
19	ZnO-Ga_2O_3	300 + 1200	300	1700	/	600	2
20	ZnO-Ga_2O_3	400 + 1200	300	1700	/	600	2
21	ZnO-Ga_2O_3	500 + 1200	300	1700	/	600	2
22	ZnO-Ga_2O_3	1000 + 1200	300	1700	/	600	2
23	$ZnGa_2O_4$	1200	300	1700	/	600	1
24	GaN	1200	20		1200	50	1

#	sample number	O_2	flow of oxygen
‡	units	NH_3	flow of ammonia
T	reaction temperature	*He*	flow of helium
p	total system pressure	*R#*	number of reaction zones

Table A8.4. Overview of the photocatalytic activities of the pure Ga_2O_3, doped Ga_2O_3, mixture of ZnO/Ga_2O_3 and their parent nitrides and as well $ZnGa_2O_4$ and its parent nitrides. All oxides given in this table are synthesized at 1200 °C and 300 mbar. All the nitrided samples compared in this table are nitrided for 5 h at 850 °C. All the activities are not in the initial state, but after the evolution rate production is stabilized. IMPORTANT: The results are calculated per gram of the catalyst to be able to compare them, because different amounts of the powder are used for POWS experiments.

†	Sample name	H_2 (mmol h^{-1} g_{cat}^{-1})	O_2 (mmol h^{-1} g_{cat}^{-1})
5	Ga_2O_3	13.7	5.7
11	Reproduced Ga_2O_3	6.94	3.1
22	Ga_2O_3-ZnO	1.53	0.74
22 →	Nitrided Ga_2O_3-ZnO	1.10	0.51
12	0.26 % Mn-doped Ga_2O_3	8.16	4.1
13	1.38 % Mn-doped Ga_2O_3	1.24	0.60
14	1.60 % Mn-doped Ga_2O_3	0	0
15	7.30 % Mn-doped Ga_2O_3	0	0
16	1.00 % Rh-doped Ga_2O_3	0.62	0.25
17	5.00 % Rh-doped Ga_2O_3	0	0
18	5.00 % Fe-doped Ga_2O_3	0	0
23	$ZnGa_2O_4$	2.32	0.95
23 →	Nitrided $ZnGa_2O_4$ (TN)	4.36	2.34
23 →	Nitrided $ZnGa_2O_4$ (TN + MWP – NH_3)	1.25	0.67
23 →	Nitrided $ZnGa_2O_4$ (TN + MWP – N_2)	0.55	0.24

† - Number of sample linked to the Table 8.3

Table A8.5. Sample labels in the lab book related to sample numbers used in this thesis (information important for reproducibility of the samples via CVS)

†	§	†	§
1	SL31	13	SL153
2	SL50	14	SL152
3	SL52	15	SL154
4	SL54	16	SL156
5	SL58	17	SL155
6	SL73	18	SL134
7	SL72	19	SL122
8	SL70	20	SL121
9	SL71	21	SL119
10	SL74	22	SL120
11	SL75	23	SL157
12	SL151	24	SL161

† - Sample number used in this thesis
§ - Sample labels associated to the lab book

List of Publications

Lukic S, Stijepovic I, Ognjanovic S and Srdic VV, (2015) "Chemical Vapour Synthesis and Characterisation of Al_2O_3 Nanopowders" *Ceramics International* 41, no. 3 (2015): 3653-3658. doi:10.1016/j.ceramint.2014.11.034

Lukic S, Menze J, Weide P, Busser GW, Winterer M and Muhler M, (2017) "Decoupling the Effects of High Crystallinity and Surface Area on the Photocatalytic Overall Water Splitting over β-Ga_2O_3 Nanoparticles by Chemical Vapor Synthesis" *ChemSusChem* 10, no. 21: 4190-4197. doi:10.1002/cssc.201701309

Lukic S, Busser GW, Zhang S, Menze J, Muhler M, Scheu C and Winterer M, (2019) "Nanocrystalline Ga–Zn Oxynitride Materials: Minimized Defect Density for Improved Photocatalytic Activity?" *Zeitschrift für Physikalische Chemie* 1, no. ahead-of-print. doi:10.1515/zpch-2019-1432

The curriculum vitae is not included in the online version for data protection reasons.

DOI: 10.17185/duepublico/74820
URN: urn:nbn:de:hbz:464-20210921-070455-5